



Universiteit
Leiden
The Netherlands

Magnetic Resonance Force Microscopy and the spin bath : towards single-spin massive-resonator entanglement and the spoiling influence of the spin bath

Voogd, J.M. de

Citation

Voogd, J. M. de. (2018, February 20). *Magnetic Resonance Force Microscopy and the spin bath : towards single-spin massive-resonator entanglement and the spoiling influence of the spin bath*. *Casimir PhD Series*. Retrieved from <https://hdl.handle.net/1887/61001>

Version: Not Applicable (or Unknown)

License: [Licence agreement concerning inclusion of doctoral thesis in the Institutional Repository of the University of Leiden](#)

Downloaded from: <https://hdl.handle.net/1887/61001>

Note: To cite this publication please use the final published version (if applicable).

Cover Page



Universiteit Leiden



The handle <http://hdl.handle.net/1887/61001> holds various files of this Leiden University dissertation.

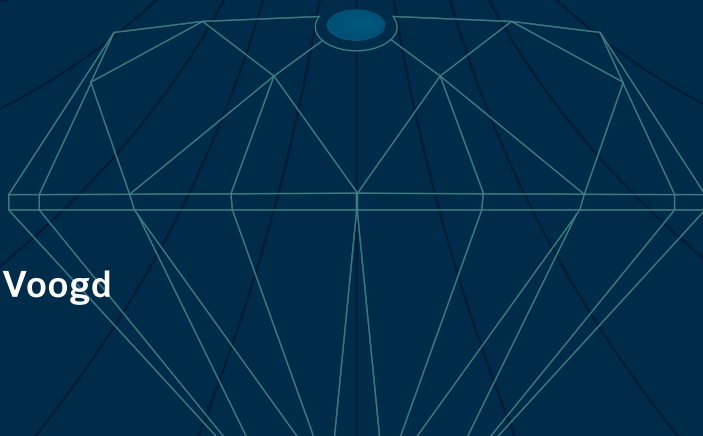
Author: Voogd, J.M. de

Title: Magnetic Resonance Force Microscopy and the spin bath : towards single-spin massive-resonator entanglement and the spoiling influence of the spin bath

Issue Date: 2018-02-20

MRFM and the Spin Bath

towards single-spin massive-resonator entanglement
and the spoiling influence of the spin bath



Marc de Voogd

Magnetic Resonance Force Microscopy and the Spin Bath

TOWARDS SINGLE-SPIN MASSIVE-RESONATOR ENTANGLEMENT
AND
THE SPOILING INFLUENCE OF THE SPIN BATH

PROEFSCHRIFT

TER VERKRIJGING VAN
DE GRAAD VAN DOCTOR AAN DE UNIVERSITEIT LEIDEN,
OP GEZAG VAN RECTOR MAGNIFICUS PROF. MR. C. J. J. M. STOLKER,
VOLGENS BESLUIT VAN HET COLLEGE VOOR PROMOTIES
TE VERDEDIGEN OP DINSDAG 20 FEBRUARI 2018
KLOKKE 13.45 UUR

DOOR

Jacobus Marinus de Voogd

GEBOREN TE VLISSINGEN
IN 1989

Promotor: Prof. dr. ir. T. H. Oosterkamp

Promotiecommissie: Dr. A. C. Bleszynski Jayich (University of California,
Santa Barbara, USA)

Prof. dr. R. Hanson (Technische Universiteit Delft)

Dr. J. van Wezel (Universiteit van Amsterdam)

Prof. dr. J. Aarts

Prof. dr. E. R. Eliel

Casimir PhD series, Delft-Leiden 2018-01

ISBN 978-90-8593-333-5

An electronic version of this thesis can be found at openaccess.leidenuniv.nl

The work described in this thesis was performed at the Huygens - Kamerlingh Onnes Laboratory, Universiteit Leiden, Niels Bohrweg 2, 2333 CA, Leiden.

This work is part of the research programme of the Foundation for Fundamental Research on Matter (FOM), which is part of the Netherlands Organisation for Scientific Research (NWO).

Cover design by Studio Zint - The cover shows a symbolic impression of the ultimate experiment as proposed in this thesis.

Copyright © 2018 Marc de Voogd

Printed by: Gildeprint - Enschede

PUBLISHED BY CASIMIR RESEARCH SCHOOL

Dedicated to

Yintel

&

Alix

Contents

1	Introduction	9
1.1	Spin mechanics	10
1.2	Mechanical resonators	12
1.3	Thermal noise	15
1.4	Heating	16
1.5	Contents	18
2	Spin - resonator equilibrium dynamics	21
2.1	Basic principles	23
2.2	Susceptibility	26
2.3	Spin bath - resonator coupling	28
2.4	Spin - electromagnetic resonator	31
2.5	Resonator coupling to other systems	33
2.6	Discussion and conclusions	35
2.7	Resonator - semiclassical spin Lagrangian	37
2.8	Equilibrium magnetic moment	37
2.9	Zeroth order solution	38
2.10	First order solution	39
2.11	Spin bath integral	41

3	Spin-mediated dissipation and frequency shifts of a cantilever at milliKelvin temperatures	43
3.1	Theory	45
3.2	Experimental details	46
3.3	Results and discussion	50
3.4	Conclusions	53
4	MRFM on diamond	55
4.1	Defects in diamond	56
4.2	Methods	61
4.3	Equilibrium dynamics	64
4.4	Spin resonance I: saturation	67
4.5	Spin resonance II: spin coherence	69
4.6	Conclusions and outlook	76
5	Gravitational decoherence of NV-resonator systems	79
5.1	Gravitational collapse	80
5.2	Probing the instability of a quantum superposition of time dilations	84
5.3	Mode heating due to spontaneous wave function collapse	88
5.4	Quantum description of spin - resonator system	90
5.5	The experiment blueprint	95
5.6	Roadmap and outlook	99
6	Techniques and instrumentation	103
6.1	Sample	104
6.2	Cantilever	107
6.3	SQUID	108
6.4	Anneal-o-tron	110
6.5	Nanopositioning	111

6.6	Cryostat wiring	117
6.7	From cryostat to electronics	118
6.8	Electronic infrastructure	119
7	Fast and reliable pre-approach for scanning probe microscopes based on tip-sample capacitance	123
7.1	Introduction	124
7.2	Subfemtofarad capacitance measurement principles	127
7.3	Results	131
7.4	Finite element analysis	136
7.5	Analytical models	141
7.6	Conclusion	144
	Bibliography	147
	List of publications	159
	Summary in dutch	163
	Experiment	164
	Techniek	166
	Wetenschappelijke bevindingen	167
	Acknowledgements	169
	Curriculum Vitae	171

1 Introduction

BUILDING EFFECTIVE RELATIONSHIPS requires speaking the same language. It is remarkable that although we formulate physics in the language of mathematics, nature itself speaks it better. After enormous investments into this relationship, physicists started seeing two different natures of nature. One of them is elegantly described by Einstein's geometric theory of gravitation,¹ better known as general relativity. The other, the nature of small things, is best described by a theory of complex valued probability amplitudes: quantum theory.

The unfeasible unification of the two theories describing both natures is one of the biggest conundrums humanity ever faced. The solution is of utmost importance as it might reveal where the universe's existence originates from, but also whether the world is deterministic or not.² Despite incredible efforts in the last century, physicist and mathematicians did not succeed creating a consistent theory of everything, yet.

A large problem of quantum theory is the understanding of why the squared norm of the normalized quantum states gives a probability distribution that describes the possible measurement outcomes, also known as Born's rule. There are several interpretations to overcome this measurement problem. In my opinion, the many worlds interpretation³ has a great resemblance with the worldview of the prisoners in Plato's cave. To free ourselves from the cave we need to ask nature itself for more information. However, performing measurements beyond quantum mechanics is a difficult

¹ Einstein 1915

² A subject closely related to free will, see Atmanspacher 2015.

³ This interpretation takes quantum theory for granted, and avoids the measurement problem.

thing to do. Luckily we are on the edge of a new era of technical possibilities where we can push systems over the supposed safe boundaries of quantum theory. We then have to compare the outcomes of these measurements with the conventional quantum theory and the different interpretations, and other beyond quantum mechanics theories.⁴

⁴Bassi et al. 2013

1.1 *Spin mechanics*

MANY RESEARCH GROUPS that are exploring the boundaries of quantum mechanics are trying to find a non-classical state of a mechanical object⁵ due to the interaction with an easily controllable quantum state (qubit). A popular version is a resonating mirror that is part of a cavity for photons. The branch of physics studying this system is called cavity optomechanics. The cavity can be replaced with other qubit-holding systems which, together with the mechanical object, can be called a hybrid quantum system.

⁵Here ‘mechanical object’ means a mass with something attached, such as a mirror, a magnet, or just being conductive, such that it can interact with some physical field (usually the electromagnetic field).

IN THIS THESIS we describe and work towards an experiment that should eventually be useful in verifying/falsifying gravitational induced spontaneous collapse models³ such as the Diósi-Penrose model⁶ and closely related models.^{7,8} The basic idea, that widespread⁹ wave functions are energetically unfavorable for the gravitational field¹⁰ compared to collapsed wave functions, can be tested by creating larger and larger position-separated superpositions of macroscopic objects. These superpositions can be created by coupling a well controlled quantum object to the macroscopic one. The force (or interaction strength) a single qubit can exert onto the mechanical object is limited and therefore a low spring constant is necessary to create a large position displacement of the mass.¹¹ The setup we choose to develop is a Magnetic Resonance Force Microscope (MRFM) coupled to a Nitrogen-Vacancy center¹² (NV⁻-center, or just NV) for several reasons: First because MRFM is a technique where the basics

⁶Penrose 2014

⁷Oosterkamp and Zaanen 2013

⁸Rademaker et al. 2014

⁹Widespread as function of position.

¹⁰Or better said: spacetime.

¹¹More on this in Ch. 5

¹²Doherty et al. 2013

have been developed in the last two decades, and nowadays there are ultrasoft cantilevers available with spring constants less than $50 \mu\text{N/m}$. Moreover, there is a whole range of spin manipulation protocols created that can directly be used.¹³ The qubit connected to our mechanical object in MRFM is a spin which is a big advantage as spin-qubits can decay and decohere very slowly. Although a nuclear spin is much more stable than an electron spin, the latter has a larger magnetic moment by three orders of magnitude and therefore a larger interaction strength by the same amount. NV-centers show the longest longitudinal (T_1) and transversal (T_2) decay times of individual electron-spin like spins¹⁴ and we argue in Ch. 5 that this is enough for our experiment. The biggest advantage of NV-centers is that they can be very precisely controlled using light and radio-frequent (RF) fields.¹² Finally it should be noted that creating a hybrid quantum system in this way, also contributes to the development of the MRFM technique, thereby making it a win-win situation. Even when in a follow-up research it turns out that the developed experiment becomes too difficult or does not give the results one could have hoped for, it most definitely has been useful for developing and commercializing the MRFM, and has provided new important single atom analysis methods to condensed matter scientists,¹⁵ biophysicists,¹⁶ and probably various industries.

¹³ Poggio and Degen 2010

¹⁴ Bar-Gill et al. 2013

¹⁵ Wagenaar et al. 2016

¹⁶ Degen et al. 2009a

BESIDE VERIFYING THEORIES, experimental results can also point towards a yet unknown theory, such as happened after the famous Michelson-Morley experiment, and the Stern-Gerlach experiment. On a smaller scale we have also seen this in this thesis: the temperature dependent dissipation experiment described in Ch. 3 helped finding the general theoretical results of Ch. 2 where we explain how a paramagnetic spin can significantly influence the resonance frequency and dissipation of a macroscopic resonator. We verified this theory and used it for the new experiment (Ch. 4-5).

A PRECISE UNDERSTANDING OF RESONATORS is necessary for all chapters in this thesis. Therefore, we continue this chapter by summarizing the basics regarding classical mechanical resonators without any specific interaction with other systems. The same principles apply to electromagnetic resonators, but as we only need this in Sec. 2.4 it is left aside for the moment. In Sec. 1.2 we provide a Lagrangian description of a bare mechanical resonator, in Sec. 1.3 we give a treatment of the thermal motion, while in Sec. 1.4 we calculate under which conditions driving the resonator may heat the system it is coupled to. In Sec. 1.5 we describe the contents of the chapters in this thesis and how these are related to each other.

1.2 Mechanical resonators

THE CLASSICAL MOTION OF THE CANTILEVER can be determined by minimizing the action. For small displacements q the cantilever can be thought of as a harmonic oscillator, whose Lagrangian, L , is

$$L = T - V = \frac{1}{2}m\dot{q}^2 - \frac{1}{2}k_0q^2. \quad (1.1)$$

Here, T and V are the kinetic and potential energy, respectively. q and \dot{q} are the generalized coordinates of the position and velocity respectively. Furthermore, m is the effective mass of the cantilever, k_0 the spring constant which the cantilever would have in case there is no interaction with parts outside the system.

As for small displacements q can be taken to point in a single Cartesian direction, we can work with the scalar q .¹⁷ Let us continue finding a classical solution for q . Minimizing the action gives us the equations of motion (EOM)

$$\frac{d}{dt} \frac{\partial L}{\partial \dot{q}} - \frac{\partial L}{\partial q} = F_{\text{ext}}(t) \Rightarrow m\ddot{q} + k_0q = F_{\text{ext}}(t). \quad (1.2)$$

The external force term is added manually based on the second law of Newton. Note that with F_{ext} the energy in the

¹⁷ Note that q can also be negative, so not q , but $|q|$ is the norm of q .

system is not conserved. In fact we should also take the dissipative mechanisms into account since this makes the cantilever move differently. The dissipative force for a harmonic resonator can be thought of as a viscous drag $-\gamma\dot{q}$ because of the movement and friction in the spring and surroundings. Since the dissipated energy depends on the path the cantilever takes, the force cannot be derived from a potential description. Therefore we manually add this dissipation term as a special kind of an external force. Rewriting the EOM gives

$$F_{\text{ext}}(t) + F_{\text{fric}}(\dot{q}) - \frac{\partial V}{\partial q} = \frac{d}{dt} \frac{\partial T}{\partial \dot{q}} - \frac{\partial T}{\partial q}, \quad (1.3)$$

where the right-hand side would be a conserved quantity (the generalized force) in case the cantilever system would be dissipationless and not influenced from the outside. From the last equation it is easy to see that we can effectively recreate a conserved system by choosing $F_{\text{ext}}(t) = -F_{\text{fric}}(\dot{q})$. We want this so we are able to do continuous measurements, but therefore we should know the path \dot{q} first.

IF WE FILL IN the terms of the last equations we find

$$m\ddot{q} + \gamma\dot{q} + k_0q = F_{\text{ext}}(t). \quad (1.4)$$

The solution of this inhomogeneous ordinary differential equation can be found in several ways. We use the Laplace transform, $\mathcal{L}\{q\}(s) = \int_0^\infty q(t)e^{-st}dt$, as we need to use that as well in Ch. 2. If we shift the time-axis such that an arbitrarily chosen initial time $t_0 \rightarrow 0$, we find

$$\begin{aligned} \mathcal{L}\{q\}(s) = & \frac{\left(s - \frac{\omega_0}{2Q}\right)q(0) + \omega_r \left(\frac{q(0)}{\sqrt{4Q^2-1}} + \frac{\dot{q}(0)}{\omega_r}\right)}{\left(s + \frac{\omega_0}{2Q}\right)^2 + \omega_r^2} \\ & + \frac{1}{\omega_0^2 + s^2 + \frac{\omega_0}{Q}s} \frac{\mathcal{L}\{F_{\text{ext}}\}(s)}{m}, \end{aligned} \quad (1.5)$$

where ω_0 is the natural frequency $\sqrt{\frac{k_0}{m}}$, Q the quality factor $\frac{\sqrt{k_0m}}{\gamma}$, and $\omega_r \equiv \pm\omega_0\sqrt{1 - \frac{1}{4Q^2}}$, which is the frequency

where the resonance is the strongest. $\mathcal{L}\{q\}(s)$ has two parts: the transients and the steady state. The transient solution is found by setting $F_{ext} = 0$, so it only depends on the initial conditions $q(0)$ and $\dot{q}(0)$. Returning to the time-domain¹⁸ we find

$$q(t) = e^{-\frac{\omega_0}{2Q}t} \left[q(0) \cos(\omega_r t) + \left(\frac{q(0)}{\sqrt{4Q^2 - 1}} + \frac{\dot{q}(0)}{\omega_r} \right) \sin(\omega_r t) \right]. \quad (1.6)$$

This solution will always decrease exponentially to the solution $q = 0$ and therefore it will be of no interest for continuous experiments. However, a so called ring down experiment, where one measures the response after giving the resonator a certain $q(0)$ or $\dot{q}(0)$, is an efficient way to measure ω_r and Q for resonators with large Q -factors.

THE STEADY STATE SOLUTION does not depend on the initial conditions and is of much more interest for us as we would like to use the resonator as a continuous detector. The steady state solution is basically the last part of Eq. 1.5. When we drive the system¹⁹ we can represent the system in the frequency domain²⁰ and find

$$\bar{q}(\omega) = \frac{e^{i\phi(\omega)}}{\sqrt{(\omega_0^2 - \omega^2)^2 + \left(\frac{\omega_0\omega}{Q}\right)^2}} \frac{\tilde{F}(\omega)}{m}, \quad (1.7)$$

where the phase ϕ can be calculated using the four-quadrant inverse tangent²¹ $\phi(\omega) = \text{atan2}\left(\frac{-\omega_0\omega}{Q}, \omega_0^2 - \omega^2\right)$.

For a sinusoidal force $F_{ext} = F_0 \sin(\omega_d t)$ the response of the system is

$$q(t) = A(\omega_d) \sin(\omega_d t + \phi(\omega_d)), \quad \text{with amplitude} \\ A(\omega) \equiv \frac{\frac{F_0}{m}}{\sqrt{(\omega_0^2 - \omega^2)^2 + \left(\frac{\omega_0\omega}{Q}\right)^2}}. \quad (1.8)$$

¹⁸ Technically we should assume $\text{Re}\{s\} > -\frac{\omega_0}{2Q}$. This is automatically satisfied as for the transients we are only interested in $\text{Re}\{s\} = 0$ (the frequency domain).

¹⁹ Just driving the resonator without feedback turned on.

²⁰ As there are no poles on the imaginary axis of s we can take $s \rightarrow i\omega$, $\mathcal{L}\{q\}(s) \rightarrow \bar{q}(\omega)$, and $\mathcal{L}\{F_{ext}\}(s) \rightarrow \tilde{F}(\omega)$.

²¹ The range of $\text{atan2}(y, x)$ is $(-\pi, \pi]$, rather than $(-\frac{\pi}{2}, \frac{\pi}{2})$ for $\text{atan}(\frac{y}{x})$.

1.3 Thermal noise

FROM THE FLUCTUATION DISSIPATION THEOREM it follows that the thermal force noise is related to the imaginary part of the Fourier transform of the linear response function of the force, i.e. the force $\tilde{F}(\omega)$ that the cantilever feels when it is moved by $q(\omega)$. It follows that the one-sided spectral density function of the force noise is given by

$$S_F(\omega) = \frac{4k_B T}{\omega} \text{Im} \left(\frac{\tilde{F}(\omega)}{q(\omega)} \right) = 4k_B T \gamma. \quad (1.9)$$

The (also one-sided) spectral density function of the position of the cantilever is then found by substituting $S_F(\omega)$ into the expression for $q(\omega)q(\omega)^*$ which gives

$$S_q(\omega) = \frac{4k_B T}{m} \frac{\frac{\omega_0}{Q}}{(\omega_0^2 - \omega^2)^2 + \left(\frac{\omega_0 \omega}{Q}\right)^2} \quad (1.10)$$

$$\approx \frac{k_B T}{k_0} \frac{\frac{\omega_0}{Q}}{(\omega_0 - \omega)^2 + \left(\frac{\omega_0}{2Q}\right)^2}. \quad (1.11)$$

In the last step we approximated the result by a Lorentzian distribution. This can be done by expanding the denominator until second order in $\omega_0 - \omega$, and neglecting higher order terms and the term $\omega_0^2 \frac{\omega_0^2 - \omega^2}{Q^2}$. This approximation is thus only valid for high Q and near resonance $\omega \approx \omega_0$. However, for our experiments the error is neglectable.²² For Lorentzian distributions it can be shown that the full width at half maximum (FWHM) is $\frac{\omega_0}{Q}$.

²² For example consider a resonator with its resonance frequency at 3 kHz and a Q of 10^4 ; then at the frequency where the spectral density is 100 times below its maximum, that is 15 Hz from resonance, the error is still less than 0.3%.

IT IS EASY TO CHECK that $S_q(\omega)$ satisfies the equipartition theorem

$$\left\langle \frac{1}{2} k_0 q^2 \right\rangle = \frac{1}{2} k_0 \int_{-\infty}^{\infty} q(t)^2 dt = \frac{1}{2} \frac{k_0}{2\pi} \int_0^{\infty} S_q(\omega) d\omega = \frac{1}{2} k_B T, \quad (1.12)$$

where we used Plancherel's theorem, and the identity

$$\int_0^{\infty} \frac{a}{(1-x^2)^2 + (ax)^2} dx = \frac{\pi}{2a} \text{ for Eq. 1.10, or } \int_{-\infty}^{\infty} \frac{a}{(x_0-x)^2 + a^2} dx = \pi \text{ for Eq. 1.11.}$$

1.4 Heating

AS THE RESONATOR has a dissipation factor, it releases heat into the environment where the dissipation occurs. Our very cold materials and samples in the experiment can have very low heat capacities. Especially the spin or spin bath in the sample that couples to the resonator is very sensitive to heating. Therefore we should calculate if the heat production of the cantilever can raise the temperature significantly, or even dramatically. Let us consider two cases: a system that is driven with a sinusoidal force, and one that is excited with white noise around the resonance peak.

BY DEFINITION of the Q-factor,²³ the average power that is lost is given by

$$P_{\text{avg}} = \frac{1}{2} k_0 \langle q^2 \rangle \frac{\omega}{Q}, \quad (1.13)$$

For the sinusoidal force with frequency $\omega = \omega_d$ we have $\langle q^2 \rangle = (A(\omega_d))^2$, where A is defined in Eq. 1.8.

IF THE FORCE is coming from a thermal force,²⁴ the total energy in the resonator is $\frac{1}{2} k_B T_m$, where T_m stands for the mode temperature which characterizes the height of the thermal spectrum. The power induced into the sample where the dissipation occurs is

$$P_{\text{avg}} \approx \frac{1}{2} k_B T_m \frac{\omega_0}{Q}. \quad (1.14)$$

The sample also has a temperature, let's say T_s , and the fluctuations in the sample will induce movement in the cantilever until the system is in equilibrium ($T_m = T_s$). The rate at which this equilibrium process goes is $\frac{\omega_0}{2Q}$, and hence the net power going from the mode to the sample is $P_{m \rightarrow s} = k_B \frac{\omega_0}{2Q} (T_m - T_s)$.

However, it might be that the sample is cooled by the environment. Let us assume that this environment has a constant temperature T_h , the heat capacity of the sample is $C(T)$, and the rate at which the temperature energy transfers from sam-

²³ The Q-factor is generally defined as $2\pi \frac{\text{Total energy stored}}{\text{Energy lost per cycle}}$.

²⁴ Or we inject white noise, which looks like thermal noise.

ple to heat bath, and vice versa, is τ . When there is a steady flow of heat, i.e. T_m and T_h are fixed, then the temperature of the sample can be derived from the stationary condition $P_{m \rightarrow s} = P_{s \rightarrow h}$, which gives

$$\frac{\omega_0}{2Q} k_B (T_m - T_s) = \frac{1}{\tau} \int_{T_h}^{T_s} C(T') dT'. \quad (1.15)$$

To solve this equation we need to know $C(T')$. For $T_s \sim T_h$ we can use the fundamental theorem of calculus and find

$$T_s = \frac{\frac{\omega_0 \tau}{2Q} k_B T_m + C(T_h) T_h}{\frac{\omega_0 \tau}{2Q} k_B + C(T_h)}. \quad (1.16)$$

Usually the resonator will loose its energy in more than one area. For calculating the temperature of each different part of the sample, one should only use the contribution of that specific part to the dissipation, and thus replace $\frac{1}{Q} \rightarrow \Delta \frac{1}{Q_s}$, see Fig. 1.1.

FINALLY, we calculate the sample temperature for a specific situation. In this thesis, the sample is usually a semiclassical spin interacting with a magnetic tip on the resonator. The precise coupling and dissipation mechanism are further explained in Ch. 2. For a two-state spin, the heat capacity is $C(T) = k_B \left(\frac{\mu_s B_0}{k_B T} \right)^2 \cosh^{-2} \left(\frac{\mu_s B_0}{k_B T} \right)$, with μ_s the magnetic moment of the spin and B_0 the average (constant) magnetic field. If we in advance already use Eq. 2.11 for the dissipation factor $\Delta \frac{1}{Q}$, and assume $k_0 \langle q^2 \rangle \gg T_s \sim T_h$, we find

$$T_s \approx \left(1 + \frac{1}{2} \frac{|\mathbf{B}'_{\parallel \hat{\mathbf{B}}_0}|^2}{B_0^2} \langle q^2 \rangle \right) T_h, \quad (1.17)$$

where $\mathbf{B}'_{\parallel \hat{\mathbf{B}}_0}$ is the gradient of the magnetic field in the direction of the constant B_0 field. We assumed that the spin is connected to the heat bath with a relaxation time ($\tau = T_1$) longer than the resonator's period. The imposed assumptions show that the approximation is only valid when $\sqrt{\langle q^2 \rangle} \ll 2B_0 / |\mathbf{B}'_{\parallel \hat{\mathbf{B}}_0}|$, which for typical values in this thesis leads to a maximal rms amplitude of 100 nm. Comparing this to the 0.05 – 0.5 nm which we would have when the can-

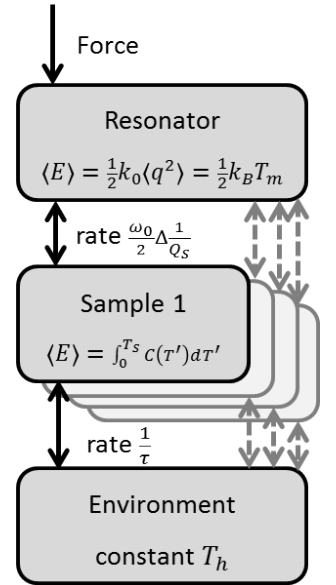


Figure 1.1: A thermodynamic schematic of the MRFM. The force working on the resonator causes a certain mode temperature. Sample 1, which is connected due to it's contribution to the Q-factor, is affected by the mode temperature. However, the sample is also (badly) connected to a heat bath. T_h is known, T_m can be measured, but what is T_s ?

tilever was thermalized to a heat bath of $0.01 - 1$ K, we see that it is not likely that the temperature of the spin bath is significantly changed due to the cantilever thermal motion. However, note that the mode temperature T_m is the sum over the squared movement of the resonator and can be significantly higher than T_h if the resonator is driven. In certain situations, such as during one of the OSCAR spin resonance protocols, the amplitude might be several 10s of nm,^{25,26} and the spin bath might heat up. When T_s becomes very different from T_h , we should recalculate T_s by solving Eq. 1.15. More on this subject is given in Ch. 2, where we take spin's resonance properties into account.

²⁵ Rugar et al. 2004

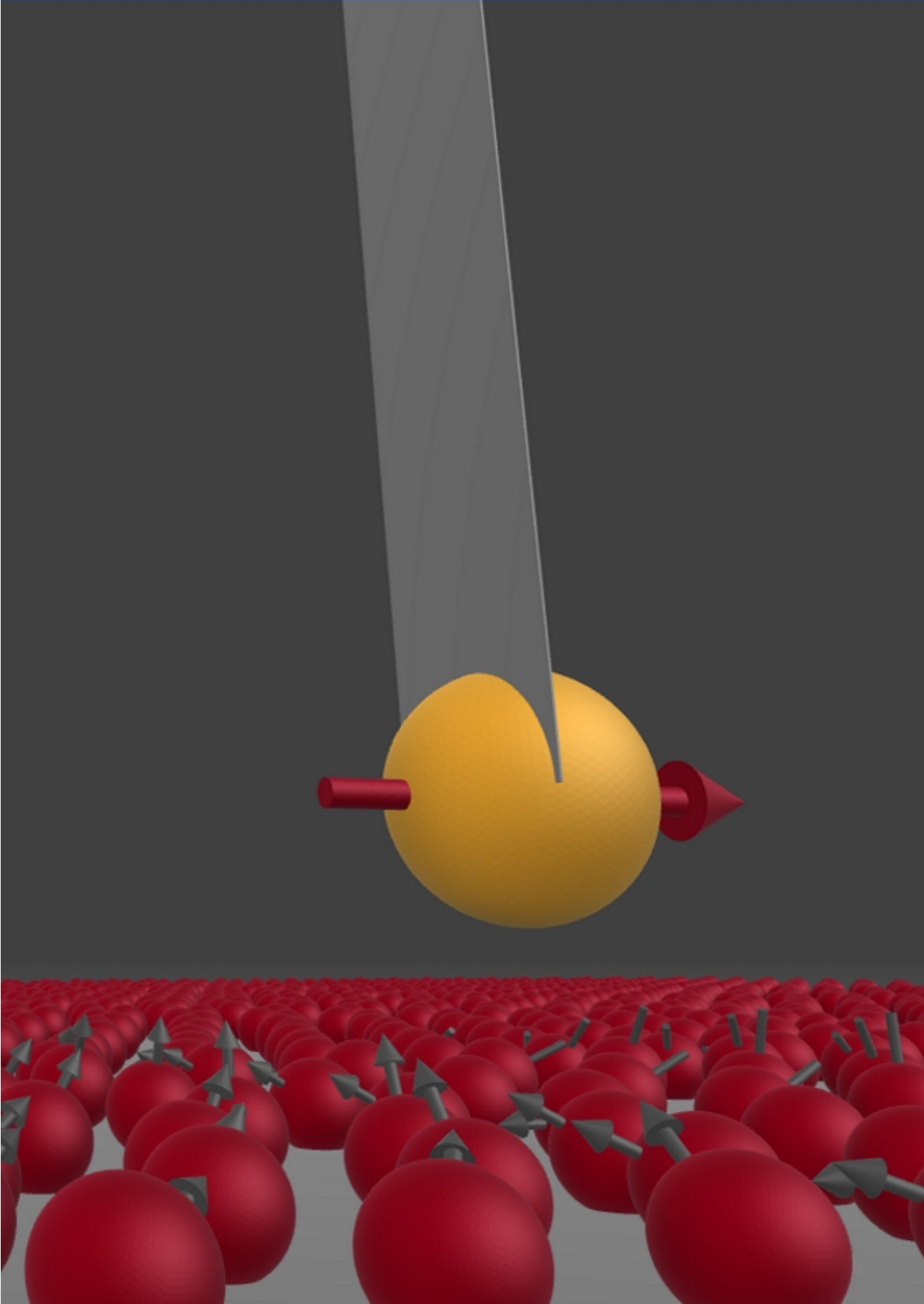
²⁶ Cardellino et al. 2014

1.5 Contents

APART FROM FORMULATING THE BASICS in this introduction chapter, we already touched on the main challenges that we need to overcome for creating an experiment that is able to measure gravitational collapse of the wave function. In our proposed experiment, where a macroscopic resonator is manipulated with the qubit, all we care about is a very good coupling between the resonator and the qubit, plus a very low dissipation of the mechanical resonator. We will show that the coupling can be very good. However, a central question, that needs to be answered in Ch. 2-4, can we also understand, control, or even avoid the dissipation? Only after we know that, it makes sense to find the optimal experiment as is explained in Ch. 5. On the other hand, numerous technical challenges that we have encountered and solved are summarized in Ch. 6. One of the most difficult parts of the MRFM experiments was, and still is, the three dimensional coarse approach at cryogenic temperatures. We tested the stability of the microscope that is used in Ch. 4 by measuring the stability of a tunneling current between a temporarily mounted Scanning Tunneling Microscope (STM) tip and a conductive sample.²⁷ As the approach of the tip to the sample had to be

²⁷ The STM-tip was mounted on the moving end of the coarse approach motor, while the Highly Oriented Pyrolytic Graphite (HOPG) sample was mounted on the base.

done without optical access, we monitored the approach by measuring the capacitance between tip and sample continuously. An analysis of this method turned into a relatively new technique which is useful for various Scanning Probe Microscopes. The article following from this spin-off side project is included as Ch. 7.



2 Spin - resonator equilibrium dynamics

We calculate the change of the properties of a resonator, when coupled to a semiclassical spin by means of the magnetic field. Starting with the Lagrangian of the complete system, we provide an analytical expression for the linear response function for the motion in the case of a mechanical resonator and the current for the case of an electromagnetic resonator, thereby considering the influence of the resonator on the spin and vice versa. This analysis shows that the resonance frequency and effective dissipation factor can change significantly due to the relaxation times of the spin. We first derive this for a system consisting of a spin and mechanical resonator and thereafter apply the same calculations to an electromagnetic resonator. Moreover, the applicability of the method is generalized to a resonator coupled to two-level systems and more, providing a key to understand some of the problems of two-level systems in quantum devices.

RESONATORS AND SPINS are ubiquitous in physics, especially in quantum technology, where they can be considered as the basic building blocks, as they can collect, store and process energy and information.^{1,2} The validity of this information is, however, of limited duration as these building blocks leak practically always to the environment, which on its own can be seen as a bath of resonators and spins.^{3,4} If in particular we focus on the situation where a resonator is coupled to a certain spin, then the spin's interaction with the environment naturally causes, besides a shift of resonance

This work is published as: De Voogd *et al.* Dissipation and resonance frequency shift of a resonator magnetically coupled to a semiclassical spin. *Sci. Rep.* 7, 42239; doi: 10.1038/s-rep42239 (2017).

¹ Nazarov and Blanter 2009

² You and Nori 2005

³ Caldeira and Leggett 1981

⁴ Prokof'ev and Stamp 2000

frequency, an extra dissipation channel for the resonator. Despite this simple qualitative explanation and many experimental^{5,6,7} and theoretical efforts,^{8,9,10,11} an applicable full picture that quantitatively describes the response of a resonator coupled to a spin and their environments is still lacking. Here we derive classically the linear response function of the non-conservative system consisting of a resonator and a semiclassical spin. We show that the quality factor and resonance frequency of the resonator can be significantly influenced due to the relaxation times of the spin.

We start with a Lagrangian description, that includes the degrees of freedom of the resonator *and* the spin, to find the coupled equations of motion (EOMs) that describe the resonator displacement and the spin magnetic moment, finding that this magnetic moment depends on the path the resonator takes. This is fundamentally different from conventional magnetic force microscopy (MFM),¹² where one assumes a fixed polarization of the spins, like in magnetized samples. Even in magnetic resonance force microscopy (MRFM), which is usually focused on paramagnetic spins, it is generally assumed that the spin is not, or at least not significantly, influenced by the resonator.^{13,14,15} We will show that this influence actually opens the dissipation channel and that the resonance frequency shift is more subtle than generally assumed.

Furthermore, we find in our analytical results that the interaction amplitude as function of temperature is a curve that for certain conditions shows an optimum, see Sec. 2.3, similar to the curves found in experiments where the tails have heuristically been fitted with power laws.^{5,6} Parts of the analysis we present here have been used by den Haan *et al.*¹⁶ to explain the experimental results obtained by approaching a native oxide layer on silicon with an ultra-sensitive MRFM probe. The equations derived in this paper were found to closely resemble the measured shift in resonance frequency

⁵ Imboden and Mohanty 2009⁶ Venkatesan et al. 2010⁷ Bruno et al. 2015⁸ Caldeira and Leggett 1983⁹ Sleator et al. 1987¹⁰ Schlosshauer et al. 2008¹¹ Pappas et al. 2011¹² Rugar et al. 1990¹³ Rugar et al. 1992¹⁴ Degen et al. 2009b¹⁵ Vinante et al. 2011a¹⁶ Haan et al. 2015

and reduced quality factor as function of temperature and resonator - spin surface distance.

Although we start calculating the susceptibility of the more intuitive mechanical resonator, we will as well derive explicitly the (additional) impedance for electromagnetic resonators (see Fig. 2.1b versus 2.1a, and Sec. 2.4), thereby making the results suitable for direct use by other fields in physics. Moreover, we will show the applicability of the theory to the case of the resonator coupled to two-level systems (2LSs) and higher level quantum systems.

Finding an accurate description of the interaction of the building blocks of quantum devices with the environment can be seen as a widespread and major research area since not being able to understand, control and minimize the interaction is a major bottleneck in: the field of quantum computing,^{11,7} detector fabrication in astronomy,^{17,18} MRFM and high resolution MRI^{19,20} and the development of optomechanical-like hybrid quantum devices.^{21,22}

2.1 Basic principles

THE CONFIGURATION of our theoretical analysis is given in Fig. 2.1a. A semiclassical spin, with magnetic moment μ , is located at laboratory position r_s and feels a magnetic field $B(r_s, t)$ that is produced by a magnet. The magnet is attached to a mechanical resonator that has spring constant k and (effective) mass m . The origin of the laboratory frame is chosen to be the equilibrium position of the magnet's center. The displacement of the magnet from this equilibrium position is denoted by $q(t)$. See Fig. 2.1. The Lagrangian for this system is given by

$$L = \frac{1}{2}m\dot{q}^2 - \frac{1}{2}kq^2 + \boldsymbol{\mu} \cdot \mathbf{B}(q) + I_S. \quad (2.1)$$

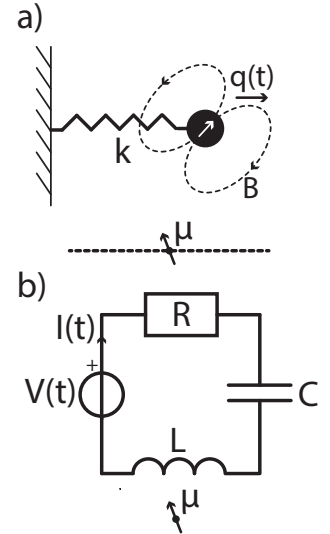


Figure 2.1: Schematic representation of spin μ interacting with two types of resonators. a) The mechanical resonator with spring constant k and displacement $q(t)$ of the magnet. The dashed line shows the position axis that is used in Fig. 2.2. b) The electromagnetic resonator as a lumped element device. The current $I(t)$ through the inductor L changes the magnetic field at the position of spin μ .

¹⁷ Day et al. 2003

¹⁸ Endo et al. 2013

¹⁹ Poggio and Degen 2010

²⁰ Kovacs et al. 2005

²¹ Aspelmeyer et al. 2014

²² Lee et al. 2017

I_S stands for an expression with the internal spin degrees of freedom that needs to be included to derive the spin EOM. A more detailed account is left in App. 2.7. The resonator-spin system does not live in an isolated world. Therefore we include dissipation and decay to the environment into the EOMs. The first differential equation, derived with respect to the resonator displacement, includes the Raleigh dissipation $-\gamma\dot{q}$ of the resonator. This results in

$$m\ddot{q} + \gamma\dot{q} + kq - \boldsymbol{\mu} \cdot \frac{\partial}{\partial \mathbf{q}} \mathbf{B} = F_{ext}(t), \quad (2.2)$$

where the last term, $F_{ext}(t)$, is an external force that is exerted on the resonator.

Starting with the Lagrangian, which contains the degrees of freedom for the resonator *and* the spin, leads to the force interaction term $-\boldsymbol{\mu} \cdot \frac{\partial}{\partial \mathbf{q}} \mathbf{B}$. This is the same as $-\boldsymbol{\mu} \cdot \nabla B_{\parallel q}$, because of the vanishing curl of the magnetic field in free space. Here $\nabla B_{\parallel q}$ is the gradient of the magnetic field component in the direction of the movement of the resonator. In MRFM $-\boldsymbol{\mu} \cdot \nabla B_{\parallel q}$ is often derived from calculating the force-field from the gradient of the potential energy $\nabla (\boldsymbol{\mu} \cdot \mathbf{B})$, assuming that $\boldsymbol{\mu}$ does not depend on the position of the resonator.²³ However, as $\boldsymbol{\mu}$ follows the classical path, we will show by solving the spin EOM that $\boldsymbol{\mu}$ is influenced by the resonator and it is therefore a priori not at all obvious that $\frac{\partial}{\partial \mathbf{q}} \boldsymbol{\mu} = 0$ as long as the spin degrees of freedom are not defined.

²³ Berman et al. 2006

THE OTHER SET of differential equations can be found by deriving the EOM with respect to the spin degrees of freedom. Since the spin interacts with the environment, we can expect an effectively decaying amplitude that is often described by T_1 and T_2 ; the time constants associated with the decay of the semiclassical magnetic moment longitudinal and perpendicular to the magnetic field, respectively.²⁴ If one assumes that the system consists of an ensemble of paramagnetic spins, instead of one, the average magnetic moment per spin decays

²⁴ Bloch 1946

to a certain equilibrium vector $\boldsymbol{\mu}_\infty$, according to the master equation.²⁵ However, if a single spin over time has on average the same behavior as the average of an ensemble at a certain moment, i.e. the spin satisfies ergodicity, then we can combine the ensemble's master equation and the single spin EOM to find a differential equation that describes the average behavior of the single semiclassical spin. This is the Bloch equation:

$$\dot{\boldsymbol{\mu}} = \gamma_s \boldsymbol{\mu} \times \mathbf{B} + T^{-1} (\boldsymbol{\mu}_\infty - \boldsymbol{\mu}). \quad (2.3)$$

Here γ_s is the gyromagnetic ratio and $T^{-1} \equiv \frac{1}{2} (\mathbb{1} - \hat{\mathbf{B}}\hat{\mathbf{B}}^T) + \frac{1}{T_1} \hat{\mathbf{B}}\hat{\mathbf{B}}^T$, where the hat denotes the unit-vector in the direction of the specified vector.

The spin equilibrium magnetic moment $\boldsymbol{\mu}_\infty(t)$ is the vector to which the spin magnetic moment would decay to if given the time. As the resonator moves, the magnetic field changes, and so does $\boldsymbol{\mu}_\infty$. We will assume that the environment of the spin is a heat bath, connected to the spin by means of the relaxation times.²⁵ However, does the spin's equivalent spin ensemble have a well defined temperature? As derived in the original paper of Bloembergen *et al.*,²⁶ the differential equation describing the population difference n for particles in a two-level system is

$$\frac{dn}{dt} = -2Wn + \frac{n_0 - n}{T_1}, \quad (2.4)$$

where W is the probability rate that the particle changes energy level due to an applied field and n_0 is the population difference between the energy levels when the ensemble has the temperature of the heat bath. In other words $-2Wn$ is proportional to the incoming energy and $\frac{n_0 - n}{T_1}$ is the connection to the heat bath. This results in

$$n_\infty = \frac{n_0}{1 + 2WT_1}, \quad (2.5)$$

where n_∞ is the steady state solution. Thus when $2WT_1 \ll 1$ the spin ensemble, and hence our semiclassical spin, is con-

²⁵ Slichter 1990

²⁶ Bloembergen et al. 1948

nected well enough to the heat bath to assume that our spin has a well defined temperature. For spin- $\frac{1}{2}$ this condition yields²⁶

$$\pi\gamma_s^2 |\mathbf{B}'|^2 q^2 T_1 g(\omega) \ll 1, \quad (2.6)$$

where $\mathbf{B}' = \frac{\partial}{\partial q} \mathbf{B} \Big|_{r=r_s}$ and $g(\omega)$ the spin's normalized absorption line that is usually described by a Lorentzian or Gaussian that peaks around the Larmor frequency. This makes this condition hard to satisfy when the resonator has a resonance frequency around the Larmor frequency, and one should minimize the resonator's movement q . When this condition is not met, the spin saturates and the temperature increases or might be undefined.²⁵ However, for example in MRFM, mechanical resonators tend to have resonance frequencies much lower than the Larmor frequency for spins close to the resonator²⁷ and very small gradients at a distant, thereby making it much easier to satisfy the condition.

²⁷ Kuehn et al. 2008

Assuming the condition is satisfied we can now derive μ_∞ from the canonical ensemble and find for spin- $\frac{1}{2}$

$$\mu_\infty = \mu_s \tanh(\beta\mu_s |\mathbf{B}|) \hat{\mathbf{B}}, \quad (2.7)$$

where $\beta \equiv \frac{1}{k_B T}$ is the inverse temperature and $\mu_s \equiv S\hbar\gamma_s$ is the magnitude of the non-averaged spin magnetic moment with spin number $S = \frac{1}{2}$. This result can easily be generalized for other spin numbers as is done in App. 2.8. For simplicity we will stick to the formula for spin- $\frac{1}{2}$ particles here.

2.2 Susceptibility

To FIND the resonance frequency and quality factor of the resonator, we will need to calculate the interaction term up to linear order in q . Higher order terms will give rise to nonlinear effects. Interaction terms with even powers in q are usually experimentally uninteresting since they will pro-

duce even multiples of the fundamental resonance frequency. These multiples are not measured or can easily be filtered. Uneven powers of q can, however, lead to disturbing nonlinear effects like Duffing.²⁸ One can lower the amplitude of q to suppress higher order terms and therefore the nonlinear effects, but in experiments this is usually limited by the signal-to-noise ratio.

The zeroth order term does not contribute to the dynamics of the system, however it does give rise to a constant deflection of the resonator. This can be solved by shifting the origin of the laboratory frame by the amount of the deflection; this causes, however, a (usually small) change of the coordinates of the spin. We will provide an estimate of the deflection in App. 2.9 and leave it further out of account.

To FIND the interaction term $-\boldsymbol{\mu} \cdot \frac{\partial \mathbf{B}}{\partial \mathbf{q}}$ up to first order in q , we need to solve Eq. 2.3 and find the constant and q -dependent parts. By substituting $q \rightarrow \lambda q$ we use perturbation theory to find

$$-\boldsymbol{\mu} \cdot \frac{\partial \mathbf{B}}{\partial \mathbf{q}} = \boldsymbol{\mu}_0 \cdot \mathbf{B}' + \lambda (\boldsymbol{\mu}_1 \cdot \mathbf{B}' - q \boldsymbol{\mu}_0 \cdot \mathbf{B}'') + \mathcal{O}(\lambda^2), \quad (2.8)$$

where $\mathbf{B}' = \frac{\partial \mathbf{B}}{\partial \mathbf{q}} \Big|_{r=r_s}$ was defined previously, and $\mathbf{B}'' = \frac{\partial^2 \mathbf{B}}{\partial q^2} \Big|_{r=r_s}$. Here $\boldsymbol{\mu}$ is perturbed into a q -independent part $\boldsymbol{\mu}_0$ and a linear term $\boldsymbol{\mu}_1$. The higher order terms $\mathcal{O}(\lambda^2)$ can be omitted, as well as the first term on the right hand side that only gives rise to the constant deflection.

At first we are mostly interested in solutions that do not decay over time and do not depend on initial conditions because then the linear response function can conveniently be given in the Fourier domain which makes it easy to compare with experiments. The Fourier Transform $\mathcal{F}\{ \}$ of the linear response function, or simply susceptibility $\chi(\omega) \equiv \frac{\tilde{q}(\omega)}{\mathcal{F}\{F_{ext}\}}$, can be calculated from Eq. 2.2

$$\chi(\omega) = \frac{1}{k - m\omega^2 + i\gamma\omega + \kappa'} \quad (2.9)$$

²⁸ Kaajakari et al. 2004

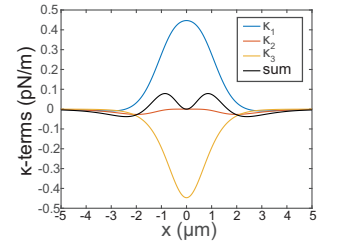


Figure 2.2: This graph shows the single spin contribution to the spring constant as function of a position axis parallel to the direction of resonator movement, as visualized by the dashed line in figure 2.1a. In the simulation we attached a magnetic dipole (with magnetic moment of 19 pAm² in the direction of q) on a mechanical resonator. The resonator is connected, by means of the magnetic field, to an electron spin at a temperature of 300 mK. The distance between the center of the dipole and $x = 0$ is 2.5 μm . To demonstrate the spatial behavior of the κ -terms we avoided imaginary terms by setting $T_1 = 0$ in κ_2 and $T_2 = 0$ in κ_3 . The solid line shows the sum of these κ -terms.

where $\kappa = \kappa_1 + \kappa_2 + \kappa_3$, with $\kappa_1 \equiv -\boldsymbol{\mu}_0 \cdot \mathbf{B}''$ and $\kappa_2 + \kappa_3 \equiv \frac{\mathcal{F}\{\boldsymbol{\mu}_1 \cdot \mathbf{B}'\}}{\bar{q}(\omega)}$. Appendices 2.9 and 2.10 present the calculation of the κ -terms, which turn out to be:

$$\kappa_1 = -\mu_s \tanh(\beta\mu_s B_0) \left| \mathbf{B}''_{\parallel \hat{\mathbf{B}}_0} \right|, \quad (2.10)$$

$$\kappa_2(\omega) = -\frac{\mu_s}{B_0} \frac{\beta\mu_s B_0}{\cosh^2(\beta\mu_s B_0)} \left| \mathbf{B}'_{\parallel \hat{\mathbf{B}}_0} \right|^2 \frac{1}{1 + i\omega T_1}, \quad (2.11)$$

$$\kappa_3(\omega) = -\frac{\mu_s}{B_0} \tanh(\beta\mu_s B_0) \left| \mathbf{B}'_{\perp \hat{\mathbf{B}}_0} \right|^2 \cdot \left(1 - \frac{2\frac{T_2}{T_1} - (\omega T_2)^2 + i\omega T_2 \left(1 + 2\frac{T_2}{T_1}\right)}{(1 + i\omega T_2)^2 + (\omega_s T_2)^2} \right), \quad (2.12)$$

where $\mathbf{B}_0 \equiv \mathbf{B}(q=0)$ and the notation $\mathbf{v}_{\parallel \hat{\mathbf{B}}_0}$ and $\mathbf{v}_{\perp \hat{\mathbf{B}}_0}$ is used to indicate the part of \mathbf{v} parallel and perpendicular to $\hat{\mathbf{B}}_0$ respectively for any vector \mathbf{v} . κ_2 and κ_3 are derived from $\boldsymbol{\mu}_{1\parallel \hat{\mathbf{B}}_0}$ and $\boldsymbol{\mu}_{1\perp \hat{\mathbf{B}}_0}$ respectively.

If we compare this result with the conventional approach that neglects the effect of the resonator on the spin, we see that in that approach we have only the term κ_1 .²⁹ However, κ_1 is real and therefore it cannot describe the extra dissipation channel that has been seen in experiments.³⁰ The derivation which has been done here does include the linear effect of the resonator on the spin and vice versa. This produces two extra terms in the linear response function that are partly imaginary. Each of the κ -terms is shown separately in Fig. 2.2 as a function of the spin position. This position axis is indicated in Fig. 2.1 by the dashed line. Which effect these terms have in practice, where usually more than one spin is present, will be shown in the next section.

²⁹ Garner et al. 2004

³⁰ Vinante et al. 2011b

2.3 Spin bath - resonator coupling

WE ASSUME that all spins in the system act individually and do not influence each other, except through the relaxation times. We can then sum over the κ -terms for each spin to find

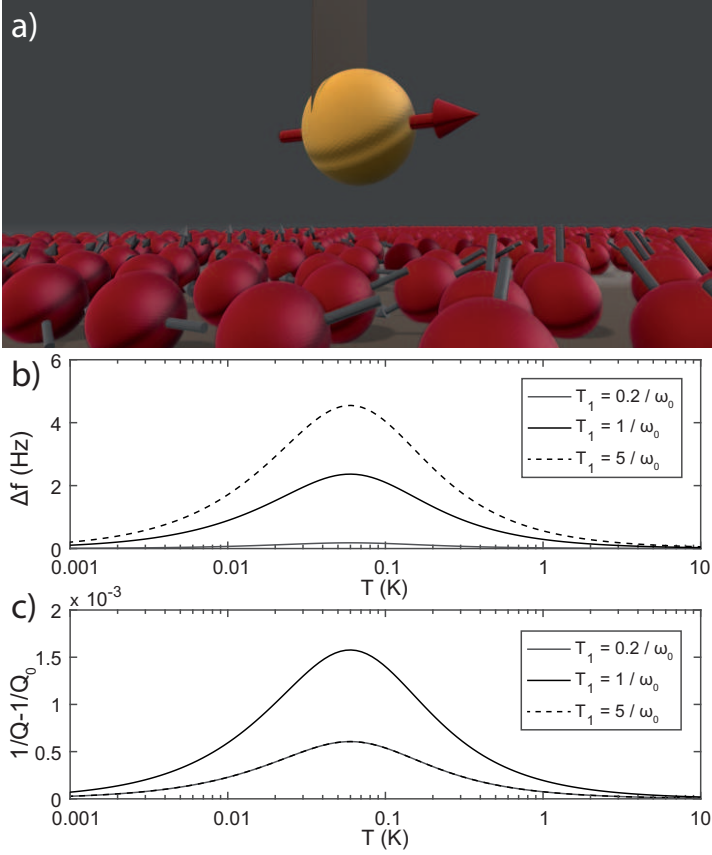


Figure 2.3: Calculated frequency shift and added dissipation of a mechanical resonator due to dangling bonds on a silicon surface, equivalent to the setup of den Haan *et al.*¹⁶. a) Impression of a Nd-FeB magnet (with magnetic moment 19 pAm^2 in the direction of q) attached to an ultrasoft silicon cantilever with spring constant $k = 70 \text{ }\mu\text{N/m}$, together leading to a natural frequency of $\frac{\omega_0}{2\pi} = 3 \text{ kHz}$. The center of the magnet is positioned at a distance of $2.2 \text{ }\mu\text{m}$ to the silicon sample. The surface of the sample has a native oxide containing $0.14 \text{ electron spins/nm}^2$ that are visualized by the red balls (not to scale). The graphs b) and c) show the resonance frequency shift and the damping of the cantilever. The results are shown for various T_1 , showing a maximal opening of the additional dissipation channel for $T_1 = 1/\omega_0$.

the susceptibility of the resonator connected to a whole ensemble of spins, i.e. $\kappa = \sum_s \kappa_1(\mathbf{r}_s) + \kappa_2(\mathbf{r}_s) + \kappa_3(\mathbf{r}_s)$. Moreover, if the spins in the sample have an average nearest neighbor distance smaller than the typical spatial scale of the applied magnetic field, we can see the sample as a spin continuum and hence, instead of summing, integrate over the sample with spin density $\rho(\mathbf{r})$.

If we calculate the result for a volume with constant spin density, it is found in App. 2.11 by partial integration of the

volume in the direction of the movement of the resonator that

$$\kappa(\omega) = \rho\beta\mu_s^2 C \frac{(\omega T_1)^2 + i\omega T_1}{1 + (\omega T_1)^2} + \text{boundary term} + \mathcal{O}\left(\frac{1}{(\omega_s^2 - \omega^2) T_2^2}\right), \quad (2.13)$$

with

$$C = \int_V d^3\mathbf{r} \frac{|\mathbf{B}'_{\parallel \hat{\mathbf{B}}_0}|^2}{\cosh^2(\beta\mu_s B_0)}. \quad (2.14)$$

The boundary term vanishes when the volume boundaries in the q -direction are large. The $\mathcal{O}\left(\frac{1}{(\omega_s^2 - \omega^2) T_2^2}\right)$ can be neglected for resonance frequencies away from the Larmor frequency and for $T_2 \gg \frac{1}{\omega_s}$.

From κ we can calculate the frequency and Q-factor shifts as seen in experiments by den Haan *et al.*¹⁶. For $Q_0 \equiv \frac{\sqrt{km}}{\gamma} \gg \frac{1}{\sqrt{2}}$ the susceptibility has a maximum around the natural frequency $\omega_0 \equiv \sqrt{\frac{k}{m}}$. Then, as long as the influence of the spin leads only to a small correction of the susceptibility, i.e. $\kappa \ll k$, the relative frequency shift is given by

$$\frac{\Delta\omega}{\omega_0} \approx \frac{1}{2} \frac{\text{Re}(\kappa(\omega_0))}{k}. \quad (2.15)$$

The imaginary part of κ causes the change in Q-factor. The new Q-factor is given by

$$\frac{1}{Q} \approx \frac{1}{Q_0} + \frac{\text{Im}(\kappa(\omega_0))}{k}. \quad (2.16)$$

In Fig. 2.3 we show an example of an experiment with a magnet attached to an ultrasoft cantilever, which is positioned above a silicon sample. The native oxide contains electron spins that interact with the resonating magnet. The frequency shift and quality factor depend differently on T_1 . In this simulation we have set T_2 to zero only after we checked that the \mathcal{O} term in Eq. 2.13 can indeed be neglected: setting $T_2 = T_1$ gives an additional frequency shift of about 1 nHz and a five orders of magnitude lower shift in Q-factor compared to the results shown in Fig. 2.3c.

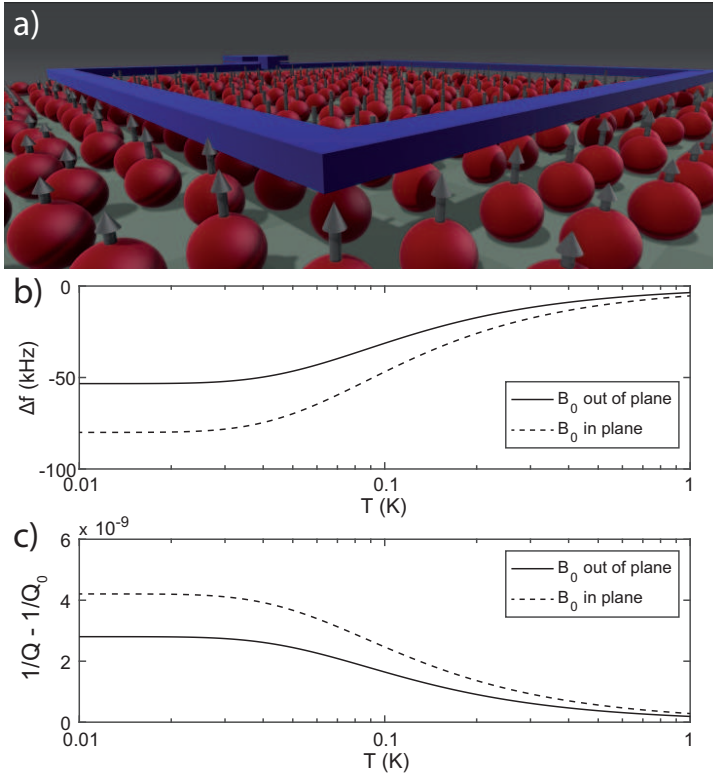


Figure 2.4: Simulation of frequency shift and added dissipation of an electromagnetic resonator due to dangling bonds at the sample's surface. a) Impression of an RLC-circuit with 10 GHz natural frequency and 0.25 nH inductance that consists of a $50 \mu\text{m} \times 50 \mu\text{m}$ square which is positioned 50 nm above a surface with 0.14 electron spins/ nm^2 b,c) Calculated results for a static external magnetic field of 0.1 T that is oriented out of plane (solid curve) and in plane (dashed curve). For this simulation we assumed $T_2 = 0.01 \mu\text{s}$.

2.4 Spin - electromagnetic resonator

IN THIS SECTION we calculate the complex impedance coming from a spin interacting with an electromagnetic resonator. The derivation is very similar to the mechanical resonator and hence we will largely copy the results. We will assume that the system can be described by a lumped element model, which is a valid approximation when the typical size of the system is much smaller than the wavelength. The results might be generalized to work for other resonators by using the distributed element model.^{31,1} However, this can become rather complicated depending on if it is necessary to calculate the interaction between resonator and spin using the retarded time (Jefimenko's equations). Moreover, it could be that the

³¹ Pozar 2011

interaction depends on the current density rather than the current, all of which is outside the scope of this paper. We conveniently describe a series RLC circuit, see Fig. 2.1b.

As there is a direct analogy with the mechanical resonator, it is straightforward to write down the complete Lagrangian and derive the EOM. From this we calculate something similar to the susceptibility, but more commonly used in electromagnetism, the impedance $Z(\omega) \equiv \frac{V(\omega)}{\bar{I}(\omega)}$.

The electromagnetic analog of the displacement q is the charge Q_e . However, instead of writing down Q_e and ‘momentum variable’ \dot{Q}_e , we prefer to work with the current $I \equiv \dot{Q}_e$. The ‘position variable’ Q_e then becomes $\int dt I$. This results in the RLC-resonator’s EOM as

$$L\dot{I} + RI + \frac{1}{C} \int dt I + \frac{d}{dt} \left(\boldsymbol{\mu} \cdot \frac{\partial}{\partial I} \mathbf{B} \right) = V(t). \quad (2.17)$$

The resulting interaction term is slightly different compared to that of the mechanical resonator. The zeroth order term vanishes conveniently due to the time derivative, leading to the impedance interaction term $z(\omega) = -i\omega \frac{\mathcal{F}\{-\boldsymbol{\mu} \cdot \frac{\partial}{\partial I} \mathbf{B}\}}{\bar{I}(\omega)}$. The spin’s EOM does not change, apart from change of variable $q \rightarrow I$. This results in an extra impedance $z = z_1 + z_2 + z_3$, equivalent to the κ -terms, where

$$z_1 = i\omega \mu_s \tanh(\beta \mu_s B_0) \left| \mathbf{B}'_{\parallel \hat{\mathbf{B}}_0} \right|, \quad (2.18)$$

$$z_2 = i\omega \frac{\mu_s}{B_0} \frac{\beta \mu_s B_0}{\cosh^2(\beta \mu_s B_0)} \left| \mathbf{B}'_{\parallel \hat{\mathbf{B}}_0} \right|^2 \frac{1}{1 + i\omega T_1}, \quad (2.19)$$

$$z_3 = i\omega \frac{\mu_s}{B_0} \tanh(\beta \mu_s B_0) \left| \mathbf{B}'_{\perp \hat{\mathbf{B}}_0} \right|^2 \cdot \left(1 - \frac{2\frac{T_2}{T_1} - (\omega T_2)^2 + i\omega T_2 \left(1 + 2\frac{T_2}{T_1} \right)}{(1 + i\omega T_2)^2 + (\omega_s T_2)^2} \right). \quad (2.20)$$

The resonators complex impedance then becomes

$$Z(\omega) = i\omega L + R + \frac{1}{i\omega C} + z. \quad (2.21)$$

It is much harder to simplify the z -terms as done in Sec. 2.3 when partially integrating over a whole sample because I

is, unlike q , not a Cartesian direction. However, one thing simplifies the z term reasonably: the law of Biot-Savart shows a linear dependence on I implying that z_1 vanishes. Note that it is very well possible that the frequencies of interest are comparable to $\frac{1}{T_2}$ or ω_s . In this case one should calculate the whole term. Moreover one should be careful with the implied condition of Eq. 2.6, i.e. $\pi\gamma_s^2 |\mathbf{B}'|^2 I^2 T_1 g(\omega) \ll 1$ when probing the resonator.

In Fig. 2.4 we provide an example of an electromagnetic RLC-circuit fabricated on top of a silicon sample with a native oxide. The electron spins inside the native oxide couple to the inductor changing the resonators resonance frequency and Q-factor.

2.5 Resonator coupling to other systems

SO FAR we have done nothing more than rigorous math to calculate the susceptibility of a system were the physical process is precisely known. However, the physical nature of the interaction between a resonator and a general two-level systems (2LSs) can be different from the simple magnetic field interaction and will often even be unknown. This subject has been studied in glassy systems long before it found its application in quantum technology.³² Mohanty *et al.*³³ connected dissipation coming from 2LSs to intrinsic frequency and quality factor changes in mechanical resonators. The calculated relaxation rate of phonons coupled to 2LSs based on Fermi's golden rule is, however, assuming Markovian dynamics. Incorporating the time dependent dynamics of the spin, as we did, lead to different results in which the dissipation depends on the history of the spin as can be seen from the T_1 and T_2 dependency.

Meanwhile the field of glassy dynamics revived when it was found in experiments that the electric permittivity and loss

³² Phillips 1972

³³ Mohanty *et al.* 2002

factor of a nonmagnetic glass do actually depend on the magnetic field.³⁴ It was only until recently, around the same time as this paper appeared on a preprint server, that Jug *et al.*³⁵ provided an intuitive and elegant explanation based on a \mathbf{B} -field dependent density of states and heat capacity. Indeed, expanding the average energy term, as we did in App. 2.8, leads to the heat capacity which resulted in $\kappa_2 \propto z_2 \propto \frac{x}{\cosh^2(x)}$ with x the Zeeman energy – temperature ratio. These similar results in combination with the results obtained in this paper imply two things: First the \mathbf{B} does not have to be the physical magnetic field. It is always possible to rewrite the two state Hamiltonian to

$$H = E_0 + \frac{\epsilon}{2B_0} \sigma \cdot \left(\mathbf{B}_0 - q\mathbf{B}' + q^2\mathbf{B}'' + \dots \right), \quad (2.22)$$

where \mathbf{B} can be any field that splits the energy levels, leading to an energy difference ϵ when $q = 0$. Here E_0 is an uninteresting energy-offset and σ is a vector containing the Pauli matrices. The interaction strength is determined by $\frac{\partial}{\partial q} \mathbf{B}$, hence it is important that \mathbf{B} depend on q , which is the generalized coordinate of the mechanical resonator, or generalized velocity of the electromagnetic resonator. Because the expectation values of the Pauli matrices σ are described by the Bloch equations, the derivations in this paper apply to any resonator-2LS system. Just substitute $\mu_s \rightarrow \frac{\epsilon}{2B_0}$ into the κ and z terms.

Secondly, this result can be easily generalized to a system with $2S + 1$ energy levels (with S an integer or half integer) by expanding the Brillouin function from App. 2.8 and substituting

$$\tanh(\beta\mu_s B_0) \rightarrow (2S + 1) \coth\left(\left(S + \frac{1}{2}\right)\beta\epsilon\right) - \coth\left(\frac{1}{2}\beta\epsilon\right) \quad (2.23)$$

$$\frac{\beta\mu_s B_0}{\cosh^2(\beta\mu_s B_0)} \rightarrow \frac{-\frac{1}{2}(2S + 1)^2\beta\epsilon}{\sinh^2\left(\left(S + \frac{1}{2}\right)\beta\epsilon\right)} + \frac{\frac{1}{2}\beta\epsilon}{\sinh^2\left(\frac{1}{2}\beta\epsilon\right)} \quad (2.24)$$

³⁴ Strehlow et al. 2000

³⁵ Jug et al. 2016

into the κ and z -terms. This $2S + 1$ -state quantum system must be isomorphic to a spin- S particle and hence meet two conditions: 1) the energy levels are equally spaced and 2) transitions are only possible to adjacent energy levels.

The general formalism presented in this section can thus be made very practical again by substituting the actual physical field responsible for the dynamics into B and finding the energy gap ϵ . This way, we hope the formalism can be of use in many systems.

2.6 Discussion and conclusions

WE HAVE calculated the linear response function of a mechanical and electromagnetic resonator coupled to a spin. The linear response function of the resonator shows extra terms that result in a shift of the resonance frequency and a drop of the Q-factor of the resonator, compared to the bare resonator characteristics. Moreover, we have generalized these results to the coupling with an energy level system with an arbitrary amount of equally spaced energy levels. In practice this means that despite having nonmagnetic samples and frequencies that are not even close to the Larmor frequency, one encounters dissipation of the resonator due to the inhomogeneous field it creates. Eventually this might not be a surprise since the resonator alters the heat capacity of the spin's equivalent spin ensemble. Although this is closely related to the magnetic loss enhancement in nonmagnetic glassy systems,³⁵ we did not find any description in literature that provides a quantitative and detailed account of how this influences the linear response of the resonator, despite the many reported and unexplained results.^{5,6,7} The results presented here have been experimentally verified¹⁶ and have been used to calculate the frequency shift in a simple, yet powerful, saturation measurement protocol.³⁶ The region

³⁶ Wagenaar et al. 2016

between infinitesimal excitation of the spins as we did and full saturation is, however, still unexplored and we anticipate that the calculation in this paper is a good starting point in a follow-up research where an additional radio-frequent field and the incoming energy, see Eq. 2.4, are incorporated. In contrast to this paper where we used the steady state solution of μ_1 , it might also be important to consider the transient solutions.

We have chosen to do the calculations completely in the (semi)classical regime as we are especially interested in the expectation value of spin and resonator. Moreover this leads to an intuitive description and fairly simple calculations. The classical treatment has its limitations though: Berman *et al.*²³ have raised the point that, if the cantilever position is constantly measured, there is an influence on the spin because of the projections that are constantly occurring in the act of measuring. This might introduce random quantum jumps which, when they are not time averaged over timescales longer than T_1 , are not taken into account in our description. Furthermore, when pulses are applied, for example in spin resonance techniques, a precise time evolution of the system is needed. Moreover, sending hard pulses might violate the condition for the temperature and linear response of the spin that we have encountered in Sec. 2.1. In this case one might move to a calculation involving the spin-operators. The theory presented here would still give a fair indication about the enhancement of dissipation, which is of importance in the field of hybrid quantum systems that are pushing the limit of macroscopic superpositions.^{22,37}

³⁷ Wezel and Oosterkamp 2012

Appendices following: Dissipation and resonance frequency shift of a resonator magnetically coupled to a semiclassical spin

2.7 Resonator - semiclassical spin Lagrangian

THE SEMICLASSICAL MAGNETIC MOMENT $\boldsymbol{\mu}$ can be seen as a vector with an azimuth ϕ and a polar angle θ , where the poles of the spherical coordinate system ($\theta = 0^\circ$ and 180°) lie on the axis parallel to the magnetic field. θ and $\dot{\phi}$ can be seen as the two degrees of freedom that a spin has. Then the Lagrangian $L = \boldsymbol{\mu} \cdot \mathbf{B}(q) + S\hbar\dot{\phi} \cos \theta$ reveals the Bloch equations for a spin- S particle, but then without decay and for magnetic moment instead of magnetization. The last term of the Lagrangian describes the internal dynamics of the spin. Substituting this into the full Lagrangian in Eq. 2.1, we find

$$L = \frac{1}{2}m\dot{q}^2 - \frac{1}{2}kq^2 + \boldsymbol{\mu} \cdot \mathbf{B}(q) + S\hbar\dot{\phi} \cos \theta. \quad (2.25)$$

2.8 Equilibrium magnetic moment

BY DEFINITION of the equilibrium vector we can state that $-\boldsymbol{\mu}_\infty \cdot \mathbf{B} = \langle E \rangle$, where $\langle E \rangle$ is the equivalent ensemble average for the energy, or for a single spin the averaged energy over all the points in time with equal q . The limited energy levels make it easy to calculate the average energy: For spin- S there are $2S + 1$ energy levels with energies $E_k = -kg_s\mu_s|\mathbf{B}|$ with $k = -S, -S + 1, \dots, S$. Using the relation between internal energy and the canonical partition function, this results in

$$\boldsymbol{\mu}_\infty = \mu_s \left((2S + 1) \coth \left((2S + 1) \beta \mu_s |\mathbf{B}| \right) - \coth \left(\beta \mu_s |\mathbf{B}| \right) \right) \hat{\mathbf{B}} \quad (2.26)$$

$$\stackrel{S=\frac{1}{2}}{=} \mu_s \tanh \left(\beta \mu_s |\mathbf{B}| \right) \hat{\mathbf{B}}. \quad (2.27)$$

This result is also known as the Brillouin function for the Zeeman energy. The imposed direction $\hat{\mathbf{B}}$ follows from Curie's law. The result might be different when the spin

has (strong) interaction with its neighbors and when this leads to anisotropic effects, although some of these effects might be included in the q independent part of \mathbf{B} .

2.9 Zeroth order solution

IF THE MAGNETIC FIELD generated by the oscillating magnet is given by $\mathbf{B}(\mathbf{r})$ in the magnet's rest frame, then in the laboratory frame the magnetic field is $\mathbf{B}(\mathbf{r} - \lambda \mathbf{q})$. Around the spin position \mathbf{r}_s the magnetic field is

$$\mathbf{B} = \mathbf{B}_0 - q\mathbf{B}' + \frac{1}{2}q^2\mathbf{B}'' + \dots \quad (2.28)$$

Here $\mathbf{B}_0 \equiv \mathbf{B}(\mathbf{r}_s)$, $\mathbf{B}' \equiv \left. \frac{\partial \mathbf{B}}{\partial q} \right|_{\mathbf{r}=\mathbf{r}_s}$ and $\mathbf{B}'' \equiv \left. \frac{\partial^2 \mathbf{B}}{\partial^2 q} \right|_{\mathbf{r}=\mathbf{r}_s}$.

Next we substitute $q \rightarrow \lambda q$ and expand $\boldsymbol{\mu}_\infty$ for spin- $\frac{1}{2}$ up to first order in λ and omit higher order terms

$$\boldsymbol{\mu}_\infty = \mu_s \tanh(\beta\mu_s B_0) \hat{\mathbf{B}}_0 - q \left(\tanh(\beta\mu_s B_0) P_\perp + \frac{\beta\mu_s B_0}{\cosh^2(\beta\mu_s B_0)} P_\parallel \right) \frac{\mathbf{B}'}{B_0}, \quad (2.29)$$

where P_\parallel and P_\perp are projections parallel and perpendicular to the \mathbf{B}_0 field respectively, i.e. $P_\parallel \equiv \hat{\mathbf{B}}_0 \hat{\mathbf{B}}_0^T$ and $P_\perp \equiv \mathbb{1} - \hat{\mathbf{B}}_0 \hat{\mathbf{B}}_0^T$. We also set $q \rightarrow \lambda q$ into Eqs. 2.3 and 2.28 and set $\lambda \rightarrow 0$ to get the differential equation to solve for $\boldsymbol{\mu}_0$:

$$\dot{\boldsymbol{\mu}}_0 = \left(\gamma_s B_{0\times} - \frac{1}{T_2} P_\perp - \frac{1}{T_2} P_\parallel \right) \boldsymbol{\mu}_0 + \frac{\mu_s}{T_1} \tanh(\beta\mu_s B_0) \hat{\mathbf{B}}_0, \quad (2.30)$$

where the \times subscript denotes an antisymmetric matrix such that $A_\times \mathbf{v} \equiv \mathbf{v} \times \mathbf{A}$ for any vector \mathbf{v} and \mathbf{A} .

Let $\mathbf{M}(s) \equiv \int_0^\infty e^{-st} \boldsymbol{\mu}(t) dt$ be the Laplace transform of the magnetic moment and apply the necessary linear algebra to get

$$\mathbf{M}_0(s) = \left(\frac{\left(s + \frac{1}{T_2} \right) P_\perp + \omega_s \hat{\mathbf{B}}_{0\times} + \frac{P_\parallel}{s + \frac{1}{T_1}}}{\left(s + \frac{1}{T_2} \right)^2 + \omega_s^2} \right) \left(\frac{1}{s} \frac{\mu_s}{T_1} \tanh(\beta\mu_s B_0) \hat{\mathbf{B}}_0 + \boldsymbol{\mu}(0) \right), \quad (2.31)$$

with $\omega_s \equiv \gamma_s B_0$. The inverse Laplace transform yields the general solution for $\boldsymbol{\mu}_0$ in

the time-domain:

$$\boldsymbol{\mu}_0(t) = \mu_s \left(1 - e^{-t/T_1}\right) \tanh(\beta\mu_s B_0) \hat{\mathbf{B}}_0 + \begin{pmatrix} e^{-t/T_2} \cos(\omega_s t) & -e^{-t/T_2} \sin(\omega_s t) & 0 \\ e^{-t/T_2} \sin(\omega_s t) & e^{-t/T_2} \cos(\omega_s t) & 0 \\ 0 & 0 & e^{-t/T_1} \end{pmatrix} \boldsymbol{\mu}(0). \quad (2.32)$$

To retrieve some intuition for the results we choose to present the last term as a matrix which is given in a non-rotating Cartesian basis with $\hat{\mathbf{z}} = \hat{\mathbf{B}}_0$.

To estimate the static displacement we use $\boldsymbol{\mu}_0(\infty)$, which is of course the same as $\boldsymbol{\mu}_\infty(q=0)$, to find the change of equilibrium position

$$q \rightarrow q - \frac{\boldsymbol{\mu}_0 \cdot \mathbf{B}'}{k + \delta k} \approx q - \frac{\mu_s}{k} \tanh(\beta\mu_s B_0) \hat{\mathbf{B}}_0 \cdot \mathbf{B}', \quad (2.33)$$

where in the last step we neglected δk , the effective extra stiffness coming from the terms linear in q .

2.10 First order solution

AS ARGUED in the main text, we can ignore the terms that decay or depend on initial conditions. As a consequence we can take $\boldsymbol{\mu}_0 = \mu_s \tanh(\beta\mu_s B_0) \hat{\mathbf{B}}_0$. This leads immediately to one of the interaction terms. Taking $\mathcal{F}\{-q\boldsymbol{\mu}_0 \cdot \mathbf{B}''\} = \kappa_1 \tilde{q}(\omega)$ with $\tilde{q}(\omega) = \mathcal{F}\{q(t)\}$ we arrive at

$$\kappa_1 = -\mu_s \left| \mathbf{B}''_{\parallel \hat{\mathbf{B}}_0} \right| \tanh(\beta\mu_s B_0), \quad (2.34)$$

where $\left| \mathbf{B}''_{\parallel \hat{\mathbf{B}}_0} \right| = \mathbf{B}'' \cdot \hat{\mathbf{B}}_0$.

Next, we need to find μ_1 . Again this is done by substituting $q \rightarrow \lambda q$ and extracting the terms that are linear in λ only. We find

$$\begin{aligned}
\dot{\boldsymbol{\mu}}_1 = & \left(\gamma_s B_{0\times} - \frac{1}{T_2} P_\perp - \frac{1}{T_2} P_\parallel \right) \boldsymbol{\mu}_1 \\
& + q(t) \left(\left(\frac{1}{T_2} - \frac{1}{T_1} \right) C - \gamma_s B'_{\times} \right) \boldsymbol{\mu}_0 \\
& - q(t) \frac{\mu_s}{B_0 T_1} \left(\tanh(\beta \mu_s B_0) P_\perp + \frac{\beta \mu_s B_0}{\cosh^2(\beta \mu_s B_0)} \right) \hat{\mathbf{B}}', \quad (2.35)
\end{aligned}$$

where $C \equiv \frac{1}{B_0} (\hat{\mathbf{B}}_0 \mathbf{B}'^T P_\perp + P_\perp \mathbf{B}' \hat{\mathbf{B}}_0^T)$.

The first line is the same as in Eq. 2.30 and therefore leads to the same matrix as in Eq. 2.31 using the same non-rotating Cartesian basis with $\mathbf{z} = \hat{\mathbf{B}}_0$. This leads to

$$\begin{aligned}
\mathbf{M}_1(s) = & \left(\frac{\left(s + \frac{1}{T_2} \right) P_\perp + \omega_s \hat{\mathbf{B}}_{0\times}}{\left(s + \frac{1}{T_2} \right)^2 + \omega_s^2} + \frac{P_\parallel}{s + \frac{1}{T_1}} \right) \cdot \\
& \left(\tanh(\beta \mu_s B_0) \left(\left(\frac{1}{T_2} - \frac{2}{T_1} \right) P_\perp \mathbf{B}' - \omega_s \hat{\mathbf{B}}_0 \times \mathbf{B}' \right) - \frac{\beta \mu_s B_0}{\cosh^2(\beta \mu_s B_0)} P_\parallel \mathbf{B}' \right) \frac{\mu_s}{B_0 T_1} Q(s), \quad (2.36)
\end{aligned}$$

with $\mathbf{M}_1(s)$ and $Q(s)$ being the Laplace transform of $\boldsymbol{\mu}_1(t)$ and $q(t)$ respectively.

\mathbf{M}_1 , and thus $\boldsymbol{\mu}_1$, can be easily split in a part that is parallel and perpendicular to $\hat{\mathbf{B}}_0$. It follows from Eq. 2.8 that we need specifically the product $\boldsymbol{\mu}_1 \cdot \mathbf{B}'$ for the interaction term. So let us write $\mathcal{F}\{\boldsymbol{\mu}_1 \cdot \mathbf{B}'\} = \tilde{q}(\omega) (\kappa_2 + \kappa_3)$ where κ_2 and κ_3 come from the parallel and perpendicular parts of $\boldsymbol{\mu}_1$ respectively. Finally we move to the Fourier domain, which is possible since all poles lie in the $\text{Re}(s) < 0$ regime. This leads to

$$\kappa_2 = -\frac{\mu_s}{B_0} \left| \mathbf{B}'_{\parallel \hat{\mathbf{B}}_0} \right|^2 \frac{\beta \mu_s B_0}{\cosh^2(\beta \mu_s B_0)} \frac{1}{1 + i\omega T_1}, \quad (2.37)$$

where $\left| \mathbf{B}'_{\parallel \hat{\mathbf{B}}_0} \right|^2 = \mathbf{B}'^T P_\parallel \mathbf{B}'$.

For κ_3 we find

$$\kappa_3 = -\frac{\mu_s}{B_0} \left| \mathbf{B}'_{\perp \hat{\mathbf{B}}_0} \right|^2 \tanh(\beta \mu_s B_0) \left(1 - \frac{2\frac{T_2}{T_1} - (\omega T_2)^2 + i\omega T_2 \left(1 + 2\frac{T_2}{T_1} \right)}{(1 + i\omega T_2)^2 + (\omega_s T_2)^2} \right), \quad (2.38)$$

where $\left| \mathbf{B}'_{\perp \hat{\mathbf{B}}_0} \right|^2 = \mathbf{B}'^T P_{\perp} \mathbf{B}'$.

2.11 Spin bath integral

WE WANT to integrate the κ -terms over a volume of spins that has a constant spin density ρ . Before we start, we split the volume in a component perpendicular ($\mathcal{V}_{q_{\perp}}$) and along ($\mathcal{V}_{q_{\parallel}}$) the resonator movement, such that we can write the integration as

$$\kappa = \rho \int_{\mathcal{V}_{q_{\perp}}} d\mathbf{q}_{\perp} \int_{\mathcal{V}_{q_{\parallel}}} dq (\kappa_1 + \kappa_2 + \kappa_3). \quad (2.39)$$

Using the identities

$$\frac{\partial}{\partial q} \tanh(\beta\mu_s B) \Big|_{r=r_s} = \frac{\beta\mu_s}{\cosh^2(\beta\mu_s B_0)} \left| \mathbf{B}'_{\parallel \hat{\mathbf{B}}_0} \right|, \quad \text{and} \quad (2.40)$$

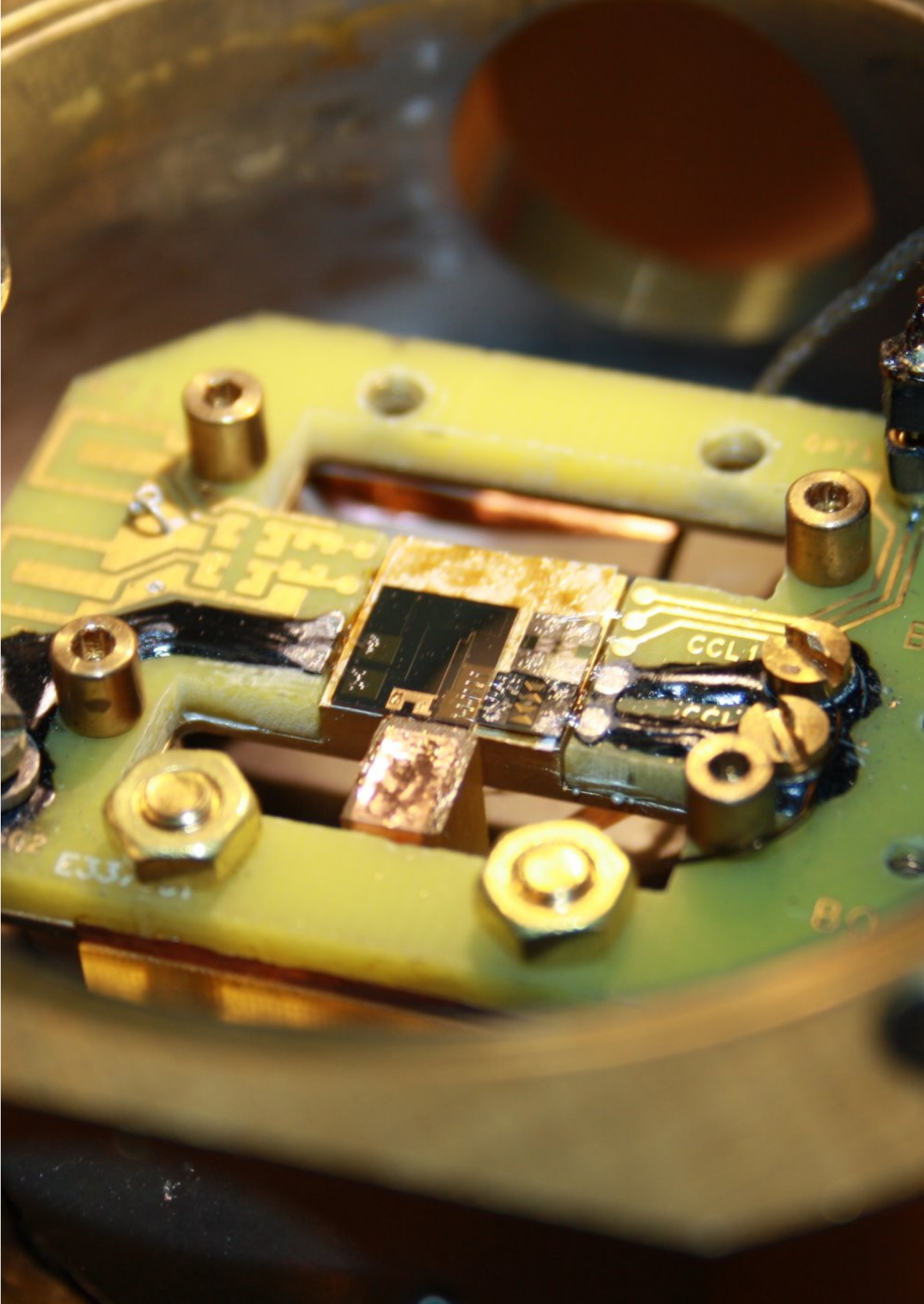
$$\frac{\partial}{\partial q} \left(\hat{\mathbf{B}} \cdot \frac{\partial}{\partial q} \mathbf{B} \right) \Big|_{r=r_s} = \left| \mathbf{B}''_{\parallel \hat{\mathbf{B}}_0} \right| + \frac{1}{B_0} \left| \mathbf{B}'_{\perp \hat{\mathbf{B}}_0} \right|^2, \quad (2.41)$$

we find by partial integration

$$\int_{\mathcal{V}_{q_{\parallel}}} dq \kappa_2(T_1 = 0) = -\mu_s \tanh(\beta\mu_s B) \left| \mathbf{B}'_{\parallel \hat{\mathbf{B}}_0} \right| \Big|_{\partial \mathcal{V}_{q_{\parallel}}} - \int_{\mathcal{V}_{q_{\parallel}}} dq (\kappa_1 + \kappa_3(T_2 = 0)). \quad (2.42)$$

Using this result and the expressions for κ_2 and κ_3 (Eq. 2.37 and 2.38), we can write the total integral

$$\begin{aligned} \kappa = & \rho \beta \mu_s^2 \frac{(\omega T_1)^2 + i\omega T_1}{1 + (\omega T_1)^2} \int_{\mathcal{V}_{q_{\perp}}} d\mathbf{q}_{\perp} \int_{\mathcal{V}_{q_{\parallel}}} dq \frac{\left| \mathbf{B}'_{\parallel \hat{\mathbf{B}}_0} \right|^2}{\cosh^2(\beta\mu_s B_0)} \\ & + \rho \mu_s \frac{2\frac{T_2}{T_1} - (\omega T_2)^2 + i\omega T_2 \left(1 + 2\frac{T_2}{T_1}\right)}{(1 + i\omega T_2)^2 + (\omega_s T_2)^2} \int_{\mathcal{V}_{q_{\perp}}} d\mathbf{q}_{\perp} \int_{\mathcal{V}_{q_{\parallel}}} dq \tanh(\beta\mu_s B_0) \frac{1}{B_0} \left| \mathbf{B}'_{\perp \hat{\mathbf{B}}_0} \right|^2 \\ & - \rho \int_{\mathcal{V}_{q_{\perp}}} d\mathbf{q}_{\perp} \int_{\mathcal{V}_{q_{\parallel}}} dq \mu_s \tanh(\beta\mu_s B) \left| \mathbf{B}'_{\parallel \hat{\mathbf{B}}_0} \right| \Big|_{\partial \mathcal{V}_{q_{\parallel}}}. \end{aligned} \quad (2.43)$$



3 Spin-mediated dissipation and frequency shifts of a cantilever at milliKelvin temperatures

We measure the dissipation and frequency shift of a magnetically coupled cantilever in the vicinity of a silicon chip, down to 25 mK. The dissipation and frequency shift originates from the interaction with the unpaired electrons, associated with the dangling bonds in the native oxide layer of the silicon, which form a two dimensional system of electron spins. We approach the sample with a 3.43 μm -diameter magnetic particle attached to an ultrasoft cantilever, and measure the frequency shift and quality factor as a function of temperature and the distance. Using a recent theoretical analysis of the dynamics of a system consisting of a spin and a magnetic resonator, we are able to fit the data and extract the relaxation time $T_1 = 0.39 \pm 0.08 \text{ ms}$ and spin density $\sigma = 0.14 \pm 0.01 \text{ spins per nm}^2$. Our analysis shows that at temperatures $\leq 500 \text{ mK}$ magnetic dissipation is an important source of non-contact friction.*

This work is published as: den Haan *et al.* Spin-mediated dissipation and frequency shifts of a cantilever at milliKelvin temperatures. Phys. Rev. B 92, 235441; doi: 10.1103/PhysRevB.92.235441 (2015).

* Presented in Ch. 2.

UNDERSTANDING the dissipation and frequency shifts in magnetic force experiments is crucial for the development of magnetic imaging techniques, e.g. Magnetic Resonance Force Microscopy (MRFM). The sensitivity of such techniques depends on the friction of the cantilevers, which therefore has increased the interest in high-quality cantilevers with quality factors exceeding a million.¹ However, the quality factor reduces due to non-contact friction with the scanned sample which is explained by dielectric fluctuations.² Far from the surface, magnetic dissipation from paramagnetic spins or nanomagnets on the cantilever have been observed to have a

¹ Tao et al. 2014

² Kuehn et al. 2006

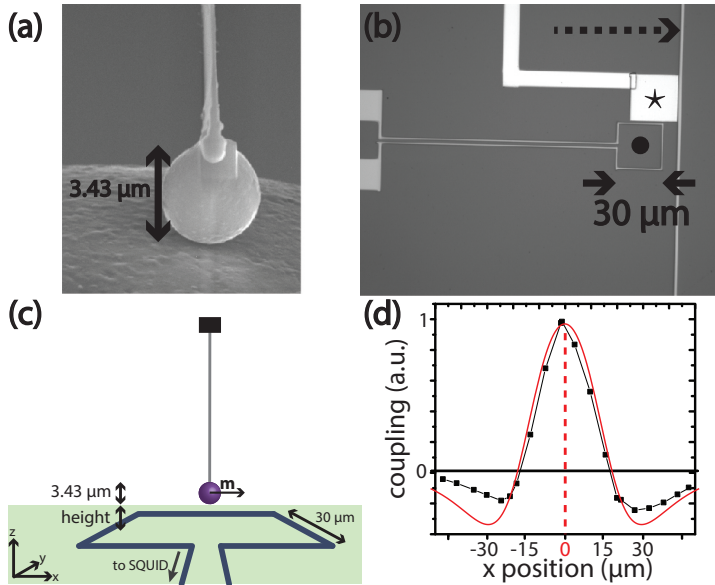


Figure 3.1: (a) Scanning Electron Microscope image of the magnetic particle after it is glued to the cantilever. (b) Optical microscope image of the detection chip. The cantilever is positioned above the center of the pickup coil (\bullet). The pickup coil is used for SQUID based detection of the cantilever's motion. The vertical wire (dotted arrow) and the copper sample (\star) are used in other experiments. (c) Sketch of the setup. The height is measured from the bottom of the magnetic particle, which has a diameter of $3.43 \mu\text{m}$. (d) The coupling with the pickup coil as function of the x -position of the cantilever. The red solid line is the calculated flux change in a square loop due to a magnetic dipole μ on a moving resonator. The maximum (scaled to 1) of the curve is at the center of the pick-up coil, which can be determined with μm precision.

³ Stipe et al. 2001a

⁴ Harris et al. 2003

large effect on the friction.^{3,4} Our report quantitatively analyzes the magnetic dissipation of a cantilever in the vicinity of a silicon chip, showing that this is the most significant non-contact friction at low temperatures for a magnet on cantilever geometry.

Magnetic Force Microscopy (MFM) measures the forces resulting from stray fields of a sample that is being scanned. The coupling of the tip with the magnetic field manifests itself as a shift in the resonance frequency of the cantilever and as additional dissipation which reduces its quality factor Q . For magnetic moments that do not change due to the magnetic tip itself, the frequency shifts are well understood. However, a more complicated model is required when the spins in the sample are paramagnetic, because the motion of the tip changes the direction of their magnetic moments.⁵ In this paper, we show frequency shifts and dissipation resulting from the dangling electron bonds at the surface of a silicon substrate. We are able to extract the relaxation time T_1 of the electron spins, without using electron spin resonance techniques. Furthermore, we use our analysis to calculate the

⁵ Rugar et al. 1990

maximum possible dissipation for a state-of-the-art MRFM setup and diamond cantilever. We show that magnetic dissipation can cause a drop in quality factor, thereby decreasing the sensitivity of an MRFM experiment. We calculate that this dissipation is suppressed when using large external magnetic fields at low temperatures.

3.1 Theory

IN OUR EXPERIMENT, a magnet attached to a cantilever (Fig. 3.1a) couples via its magnetic field $\mathbf{B}(\mathbf{r})$ to magnetic moments $\boldsymbol{\mu}$ originating from localized electron spins with near-negligible interactions. The coupling with a single spin can be associated with a stiffness k_s , which results in a shift Δf of the natural resonance frequency f_0 of the cantilever, according to $\Delta f = \frac{1}{2} \frac{k_s}{k_0} f_0$, with k_0 the natural stiffness of the cantilever.

⁶ Rugar et al. 2004

Commonly, the analysis of magnetic interaction⁶ begins with the interaction energy $E = -\boldsymbol{\mu} \cdot \mathbf{B}(\mathbf{r})$. And one calculates the force and stiffness acting on the cantilever by taking the first and second derivative with respect to x , the direction of the fundamental mode of the cantilever. Assuming that $\boldsymbol{\mu}$ is fixed by a large external field, one obtains in this approach a stiffness in the form of $k_s = \boldsymbol{\mu} \cdot \frac{\partial^2 \mathbf{B}(\mathbf{r})}{\partial x^2}$. A recent detailed analysis by De Voogd *et al.*,^{7*} which starts with the Lagrangian of the full system, taking into account the spin's dynamics as well as the influence of the mechanical resonator on the spin, suggests that the commonly employed model is not the correct approach for paramagnetic spins. For paramagnetic spins, the relaxation and the exact dynamics of the spin in the cantilever's magnetic field determine the frequency shifts and dissipation. In the case of a two-dimensional system of paramagnetic spins, uniformly distributed over an infinite surface, the frequency shift Δf and shift in the inverse quality

⁷ Voogd et al. 2017b

* Presented in Ch. 2.

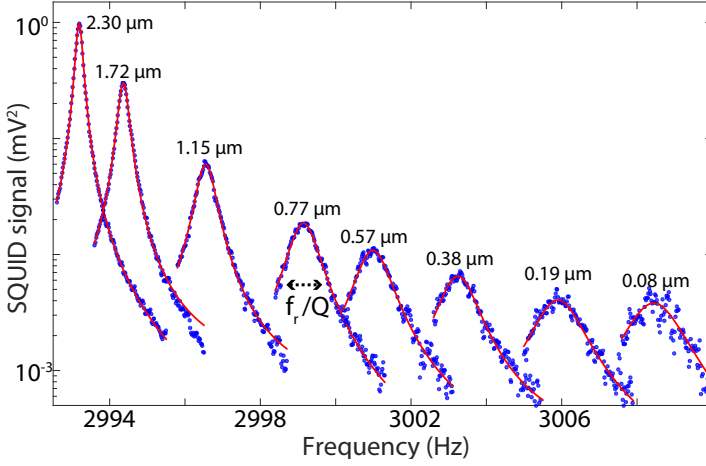


Figure 3.2: Frequency sweeps of the cantilever at a temperature of 70 mK. When moving towards the sample, the resonance frequency f_r increases, while Q decreases due to an increasing coupling with the surface electron spins. We extract f_r and Q by fitting the data to a Lorentzian (red solid line).

factor $\Delta \frac{1}{Q}$ can be written as:

$$\frac{\Delta f}{f_0} = \frac{1}{2} C \cdot \frac{(2\pi f_0 T_1)^2}{1 + (2\pi f_0 T_1)^2}, \quad (3.1)$$

$$\Delta \frac{1}{Q} = C \cdot \frac{2\pi f_0 T_1}{1 + (2\pi f_0 T_1)^2}, \quad (3.2)$$

$$C = \frac{\sigma \mu^2}{k_0 k_B T} \iint_S \frac{(\hat{\mathbf{B}}(\mathbf{r}) \cdot \frac{\partial \mathbf{B}(\mathbf{r})}{\partial x})^2}{\cosh^2(\frac{\mu \mathbf{B}(\mathbf{r})}{k_B T})} d\mathbf{r}. \quad (3.3)$$

Where T is the temperature, k_B is the Boltzmann constant and T_1 is the spin's longitudinal relaxation time. The integral is performed over the infinite surface assuming a constant spin density σ . We have assumed $\Delta f \ll f_0$, $Q \gg 1$, and that the inverse of the transverse relaxation time T_2^{-1} is much smaller than the Larmor frequency, which is already the case when T_2 is larger than 1 μ s.

3.2 Experimental details

IN THIS EXPERIMENT, we detect the dangling bonds that are present on the surface of a silicon substrate of the detection chip using MFM down to 25 mK. We use a commercial

cryogen-free dilution refrigerator, in which we implemented several vibration isolation measures.⁸ We are able to coarse approach towards the sample in three dimensions, with a range of 1 mm in x, y and z. For this we employ three ‘Piezo-Knobs’⁹ while reading out the position using three capacitive sensors.

The cantilever is a silicon micro-machined IBM-type with length, width and thickness of 145 μm , 5 μm and 100 nm, respectively.^{10,11} The magnetic particle is a spherical particle from a commercial neodymium-alloy powder.¹² We used platinum electron beam induced deposition using an in-house developed nanomanipulator¹³ in a Scanning Electron Microscope (SEM) to attach the small magnetic particle on the free end of the cantilever and measured the diameter to be 3.43 μm (Fig. 3.1a). Subsequently, we magnetized the magnet in the x-direction at room temperature in a field of 5 T.

The readout of the cantilever’s motion is based on a Superconducting Quantum Interference Device (SQUID) which enables low temperature experiments.¹⁴ Where in conventional MFM setups a laser is used to readout the motion, our method is based on the motion of the magnetic particle in the vicinity of a small superconducting ‘pickup’ coil, giving a flux change whenever the cantilever moves (Fig. 3.1c). This signal is transformed by an on-chip transformer, which matches the pickup coil inductance to the high SQUID input inductance. The measured flux noise in the complete setup is less than $4 \mu\Phi_0/\sqrt{\text{Hz}}$, where Φ_0 is the flux quantum.

The substrate is high resistivity ($> 1 \text{ k}\Omega\text{cm}$) (100)-oriented n-type (phosphorus doped) silicon. The substrate is cleaned with acetone and DI water, which leaves an interface of silicon with its native oxide. To create the superconducting structures on the chip, NbTiN is grown on the silicon substrate with a thickness of roughly 300 nm. Patterning is done using standard nano-lithographic techniques and reactive ion etching in a SF_6/O_2 plasma. For future MRFM experiments, we added a wire for radio-frequency currents and a 300 nm thick copper layer capped with gold. The copper is connected

⁸ Haan et al. 2014

⁹ PiezoKnobs from Janssen Precision Engineering B.V.

¹⁰ Chui et al. 2003

¹¹ Mamin et al. 2003

¹² The neodymium-alloy powder is of type MQP-S-11-9-20001-070 by Magnequench, Singapore

¹³ Heeres et al. 2010

¹⁴ Usenko et al. 2011

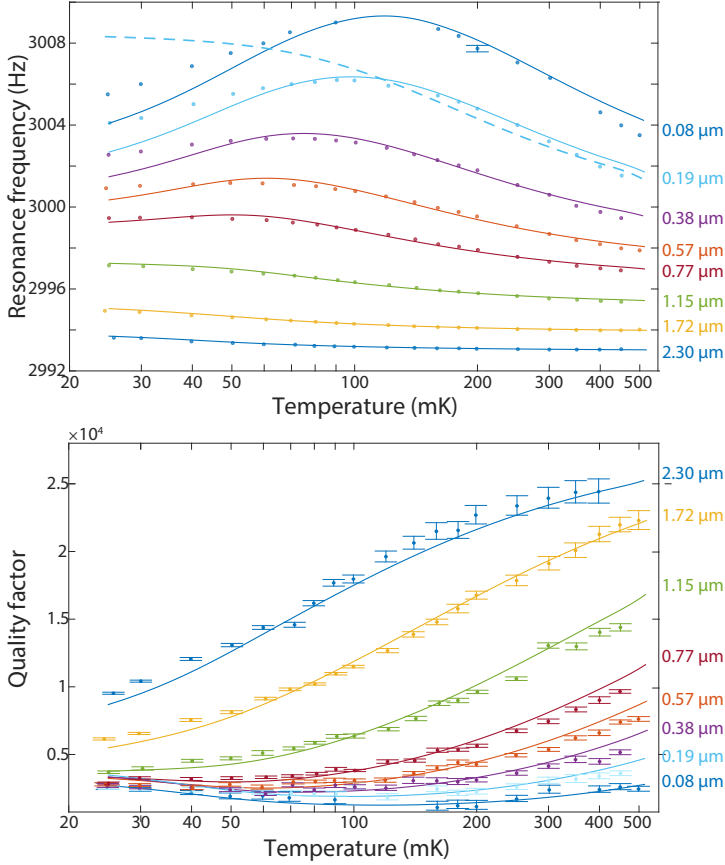


Figure 3.3: Resonance frequency f_r and quality factor Q versus temperature for different heights of the cantilever with respect to the sample. For the quality factor, the error bars indicate the 95% confidence intervals of the Lorentzian fit. For the frequencies the average error was 0.01 Hz, which is smaller than the point size, except for one data point. The solid lines are fits to the data with the spin density σ , spin relaxation time T_1 and frequency offset f_0 as fitting parameters. f_r and Q are simultaneously fitted for each height. The results of the fit can be found in table 3.1. The dashed line is the frequency shift calculated with the commonly used expression $k_s = p\mu \cdot \frac{d^2B}{dx^2}$, with $p = \tanh\left(\frac{\mu B(r)}{k_B T}\right)$ and with σ ten times smaller than we find in our analysis.

via golden wire bonds to the sample holder, which itself is connected via a silver welded wire to the mixing chamber, ensuring good thermalization of the sample. Figure 3.1b shows an optical microscope image of the obtained structure. We drive the cantilever using a small piezo element glued to the cantilever holder. We sweep the drive frequency using a function generator around the resonance frequency f_r while measuring the SQUID's response using a Lock-In amplifier. We fitted the square of the SQUID's signal with a Lorentzian curve in order to extract f_r and Q . The amplitude of the Lorentzian is determined by the coupling between the magnet and the pickup coil, which is proportional to the energy coupling, and can be used to determine the position of

the cantilever by scanning the cantilever in the xy -plane, see Fig. 3.1d.

FOR THE EXPERIMENT PRESENTED IN THIS PAPER, we positioned the cantilever above the center of the pickup coil, to minimize possible repulsive forces from the superconducting wires. By gently decreasing the height of the cantilever until the signal is completely lost, we determine the relative height of the magnetic particle with respect to the surface. The sample holder is placed on a finestage, machined out of aluminum, which can be moved in all spatial directions by actuating laminated piezoelectric extension stacks. Using this, we can now have good control of the height up to the full range of the finestage of $2.3 \mu\text{m}$.¹⁵

We swept the drive frequency at a drive amplitude small enough to avoid non-linear responses of the cantilever's motion, while measuring the SQUID signal. We measured with a sampling time of 2 s every 0.02 Hz. Fitting the data with a Lorentzian, we obtain f_r and $Q = \frac{f_r}{FWHM}$. At each height, the temperature was varied from the lowest achievable temperature ≈ 25 mK, up to 500 mK. Above 500 mK, the aluminum shielding of the experiment starts to become non-superconducting. An example of the data with the Lorentzian fits at all used heights at 70 mK is shown in Fig. 3.2.

¹⁵ The piezoelectric extension stacks are of type P-883.51 by Physik Instrumente GmbH and Co. KG, Germany. To determine the range of the finestage, we extrapolated data from reference Taylor et al. 2006 for the actuator constant from 20 K to 0 K.

Height (μm)	spin density (nm^{-2})	Relaxation time (ms)
0.08	0.142	0.42
0.19	0.137	0.52
0.38	0.140	0.48
0.57	0.142	0.42
0.77	0.136	0.38
1.15	0.130	0.32
1.72	0.133	0.28
2.30	0.168	0.33
mean:	0.14 ± 0.01	0.39 ± 0.08

Table 3.1: Obtained values for the spin density σ and relaxation time T_1 for every height z above the sample. See Fig. 3.3 for the individual fits figure. The bottom row shows the average value and the standard deviation.

3.3 Results and discussion

THE RESULTS OF OUR MEASUREMENTS described above are shown in Fig. 3.3 together with the fits according to Eqs. 3.1 and 3.2. At every height z and temperature T we calculate the value for C according to Eq. 3.3. The quality factor far from the surface $Q_0 = 2.8 \cdot 10^4$. The stiffness $k_0 = 7.0 \cdot 10^{-5} \text{ Nm}^{-1}$ of the cantilever is calculated using $k_0 = m_{eff} (2\pi f_0)^2$ with $f_0 = 3.0 \text{ kHz}$ and $m_{eff} = 2.0 \cdot 10^{-13} \text{ kg}$. The effective mass m_{eff} is calculated using the geometry of the cantilever and the magnetic particle. The magnetic particle is taken as a spherical dipole with magnetic moment m . According to the model, the temperature at which the resonance frequency close to the sample has a maximum, is independent of σ and T_1 , but is dependent on the absolute value of m and the distance to the sample. We find $m = 1.9 \cdot 10^{-11} \text{ JT}^{-1}$. From this we find an effective saturation magnetization of 1.15 T for a sphere that is fully magnetic. Alternatively we can assume $\mu_0 M_{sat} = 1.3 \text{ T}$ and an outer layer of 200 nm which is magnetically dead. The magnetic moment of the dangling bonds¹⁶ is equal to the Bohr magneton $\mu = 9.274 \cdot 10^{-24} \text{ JT}^{-1}$. The solid lines in Fig. 3.3 are fits to the data according to Eqs. 3.1 and 3.2 with σ , T_1 and f_0 as the only fitting parameters. All fitting parameters are separately fitted for each height, for both the frequency data and the quality factor data. f_0 is a temperature independent parameter different for each height, which we attribute to an unknown mechanism, since the coupling to the SQUID is too small of an effect at these distances and has a height dependence with opposite sign to the one observed. The results of the fits for T_1 and σ can be found in table 3.1. We left σ as fitting parameter for each height, to verify the correctness of our analysis, since this number should be the same for each height. We see that T_1 slightly increases when the magnetic particle approached the surface, as is also observed for bulk spins in electron spin resonance experiments.¹⁷ T_1 could depend on temperature,

¹⁶ Haneman 1968

¹⁷ Stipe et al. 2001b

but by taking the ratio of Eq. 3.1 with Eq. 3.2 we extract T_1 for each measurement, and we find that T_1 is constant with temperature to within 20%. The average values of all individual fits are $\sigma = 0.14 \pm 0.01$ spins per nm^2 and $T_1 = 0.39 \pm 0.08$ ms. The found value for σ is similar to values measured using Electron Paramagnetic Resonance.^{16,18}

¹⁸ Lemke and Haneman 1975

The dashed line in figure 3.3 is the frequency shift calculated with the commonly used expression $k_s = p\mu \cdot \frac{d^2B}{dx^2}$, with $p = \tanh\left(\frac{\mu B(r)}{k_B T}\right)$. Important is that for this curve, the spin density is ten times smaller than we find with our analysis.

The deviation of the data from the fit for low temperatures and small values for z can be understood by considering that we do not have only spins at the surface. Electron spins inside the bulk will cause deviations to the fits, already when the density is in the order of 10^4 spins per μm^3 which is less than 1 ppm of the silicon atoms. Considering the nuclear spins, the 4.7% natural abundance of the ^{29}Si isotope can only account for less than 1 percent deviation.

Note that in electron spin resonance studies with our MRFM setup, a value for T_1 in the order of seconds was reported.¹⁹ With our new analysis we believe that it is possible that the reported long lived frequency shifts could be caused by nuclei polarized by interactions with these electron spins, and that these electron spins were actually much shorter lived, as is reported²⁰ for nitroxide-doped perdeuterated polystyrene films. Our analysis suggests that the spin mediated dissipation is the main mechanism leading to a significant reduction in the quality factor of the cantilever. Previous work at higher temperatures² reports dielectric fluctuations as the main non-contact dissipation mechanism. We do not see any evidence in our measurements for this. Possibly, the use of a laser in the setup to read out the cantilever causes extra charge fluctuations. Furthermore, we work at lower temperatures, where the large spin polarization enhances the magnetic dissipation and possibly reduce fluctuating charges.

¹⁹ Vinante et al. 2011a

²⁰ Chen et al. 2013

We calculated the magnetic dissipation for a magnetic imag-

Calculated quality factors ($\cdot 10^6$)			
	$T = 10$ mK	$T = 300$ mK	$T = 4.2$ K
$B_{ext} = 0$ T	0.49	0.20	0.98
$B_{ext} = 0.1$ T	1.50	0.19	0.91
$B_{ext} = 6$ T	1.50	1.50	1.17

ing experiments at higher temperature and a different tip-sample geometry. The results can be found in Tab. 3.2. We used the experimental parameters for a state-of-the-art MRFM.²¹ In this apparatus, the bare non-magnetic cantilever is centered approximately 50 nm above a magnetic particle on the substrate, which is assumed for simplicity to be a spherical particle with a radius of 100 nm. This setup is equivalent to a magnetic dipole attached to the cantilever itself approaching a surface with the shape of the cantilever. The magnetic dipole and external field are oriented in the z-direction while the fundamental mode of the cantilever is in the x-direction. For the cantilever, we used the parameters of a recently developed diamond cantilever¹ which is shown to have at low temperatures an intrinsic quality factor $Q_0 = 1.5 \cdot 10^6$, resonance frequency $f_0 = 32$ kHz and stiffness $k_0 = 6.7 \cdot 10^{-2}$ Nm⁻¹. A spin density $\sigma = 0.14$ nm⁻² is used, which is found in this report to be the density for the silicon surface, but it is also close to the typical values found for diamond surfaces.²² Only spins at the very end of the cantilever are considered since this surface contributes most to the dissipation, which is 0.66 μ m thick and 12 μ m wide. Although Eq. 3.1 cannot be used since we do not have a uniform infinite surface anymore, according to the original expressions⁷ one can continue to use Eq. 3.2 for the dissipation replacing the integral in Eq. 3.3 over the end of the cantilever. The relaxation time is chosen such that the dissipation is maximum: $T_1 = (2\pi f_0)^{-1} = 5.0$ μ s. The values in Tab. 3.2 show that the magnetic dissipation could be an important source of non-contact friction. Furthermore we see that applying external fields can reduce the magnetic dissipation. Considering these

Table 3.2: Calculated quality factor Q for three different temperatures and external magnetic fields assuming magnetic dissipation as the only source for non-contact friction. Calculations are based on a state-of-the-art MRFM apparatus with a ‘sample on cantilever’ geometry and a cantilever with an internal quality factor $Q_0 = 1.5 \cdot 10^6$.

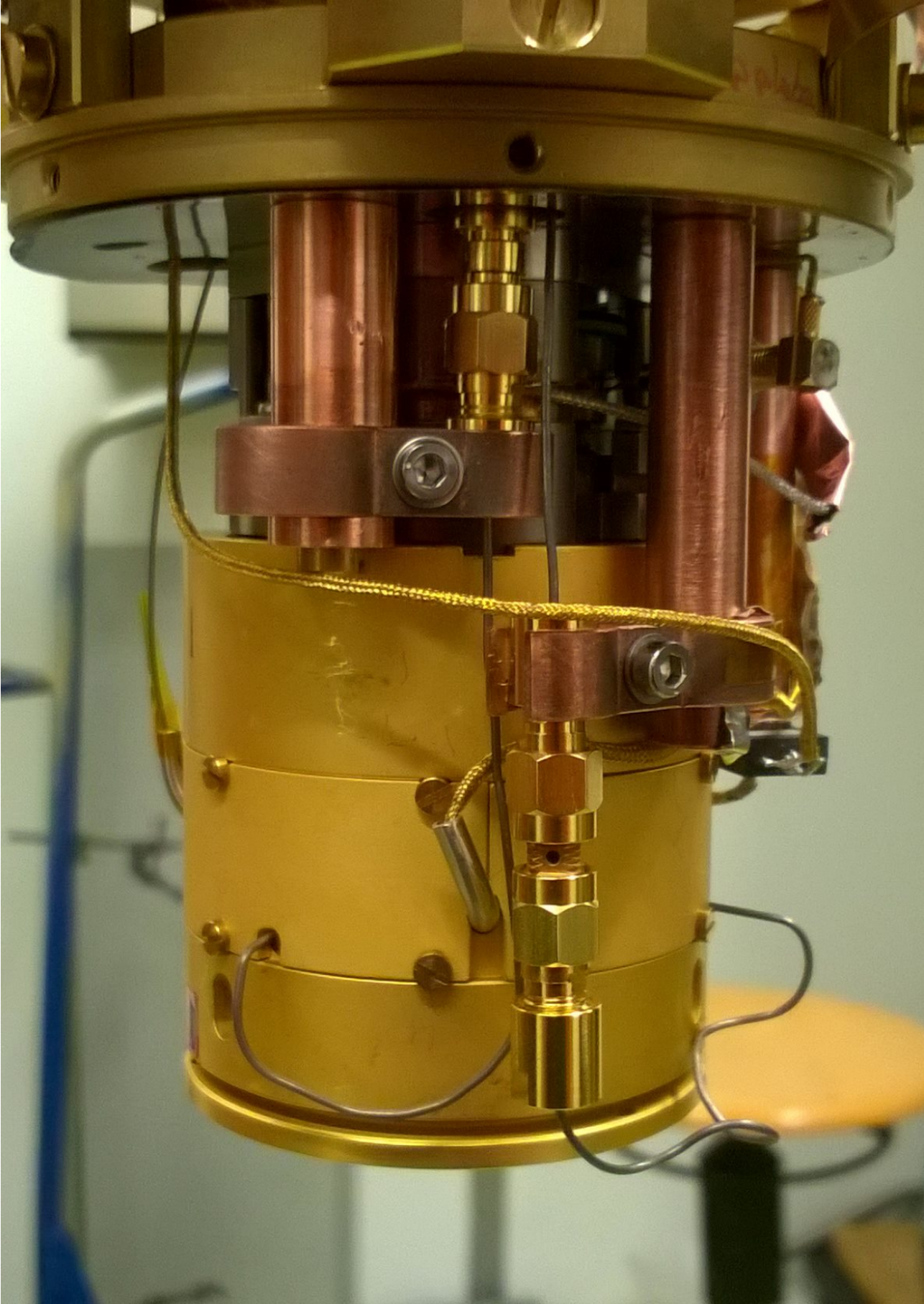
²¹ Degen et al. 2009a

²² Roskopf et al. 2014

calculations we believe that the magnetic dissipation we find at low temperatures can be avoided with the correct choice for the substrate and the use of large external magnetic fields.

3.4 *Conclusions*

TO SUMMARIZE, we have shown how the dissipation and frequency shift mediated by spins in magnetic force experiments can be fully understood. The new analysis suggest that in order to achieve higher sensitivity in magnetic imaging techniques, one should not only focus on improving the intrinsic losses of the micro-mechanical cantilever, but also on the reduction of electron spins in the sample. Furthermore we have shown how the spin's relaxation time can be extracted without the use of resonance techniques. For silicon substrates with native oxides, we find a relaxation time of $T_1 = 0.39 \pm 0.08$ ms and a spin density of $\sigma = 0.14 \pm 0.01$ per nm^2 . The understanding of the spin mediated dissipation is important to further improve the mechanical resonators in magnetic imaging experiments.



4 MRFM on diamond

DIAMOND is well known for its extreme properties. For example, it is the hardest known natural material, and at room temperature it can even have a higher thermal conductivity than that of copper. Synthetic single crystalline diamond that is grown by a Chemical Vapor Deposition (CVD) process can be extremely clean, offering < 0.05 ppb of impurity levels.¹ Most of these impurities are nitrogen atoms, sometimes accompanied by an atom vacancy (NV-center). The abundance of the impurities and the ratio of NV-centers to nitrogen impurities can be tuned by nitrogen implementation techniques and/or annealing.² Before applying these techniques, we expect an NV-center to nitrogen impurity ratio of 10^{-3} .¹

TO HAVE A COHERENT INTERACTION between the MRFM-tip and an NV-center, one should have an exceptional setup that satisfies many constraints. We have combined the ideas and experiences that we collected since we started MRFM experiments in 2008 into a new setup.³ In this chapter we describe the first experiment with this setup where we test the interaction of our cantilever's magnetic tip with the diamond sample. The experiment has two scientific goals: 1) to measure the resonance frequency shift and extra dissipation coming from the nitrogen impurities in the bulk and influence of the spins in the dirt on top of the diamond, and 2) to measure the nitrogen impurities by doing ESR using various MRFM protocols. The holy grail is to optimize the experiment in such a way that eventually a single NV-center can be

¹ *The element six CVD diamond handbook*, Element Six Technologies 2015

² Cardellino et al. 2014

³ See Ch. 6 for an explanation of the technical aspects.

used to create an entanglement with a mechanical resonator.⁴ Here we show that the diamond provides a significant dissipation path for the mechanical resonator. In fact, we show that the dissipation cannot only be ascribed to impurities in the bulk, but also the spins on the diamond surface have a large influence - probably even larger than the bulk spins.

⁴ This is the subject of Ch. 5.

THE TECHNICAL CHALLENGES faced in this experiment are numerous and a detailed explanation about our current solutions is given in Ch. 6. The experiment described in this chapter will show us the new challenges to be taken. A special feature in the design is the unmatched superconducting microwave line over the diamond that should be able to transmit ~ 10 mA currents up to a frequency of 5 GHz. The question this experiment should answer is whether the radio frequent (RF) magnetic field that is generated by these currents is strong enough to invert the targeted spins while not heating up the spin bath. Although unwanted heating seems to play a role in saturation experiments, the fields should be strong enough to do coherent spin manipulations such as adiabatic inversions, even though the bulk of our sample only has only 1 electron spin per $(24 \text{ nm})^3$. A more precise determination is left for successive experiments. In Secs. 4.1, 4.4 and 4.5 we provide analyses for the expected signals and we show that our current setup should be able to measure these. With the theoretical and experimental ingredients available, future experiments are very promising.

4.1 Defects in diamond

DEFECTS in diamond can be found in the lattice structure, such as vacancies, interstitial defects or dislocations, or from the abundance of impurities; i.e. atoms that are not ^{12}C . Many of the defects feature optical transitions and can therefore be studied by photoluminescence. In this chapter we are only interested in systems that interact with the mag-

netic field, regardless of their optical properties. Loubser and van Wyk⁵ provided an overview of electron spin resonance (ESR) in diamond describing many defects involving nitrogen impurities. Neutral nitrogen atoms have one more electron than the carbon atoms they replace. The extra electron(s) are shared with adjacent atoms and they can form a spin system which is different from a free electron spin. However, the g-factors of the defects described in this chapter ranges only from 2.002 – 2.009, close enough to the electron g-factor for us to assume we are dealing with simple electron spins. These spins can, however, be distorted due to the hyperfine structure which we will explore in more detail.

Given our sample,⁶ and what has been reported in literature,^{5,7} we can assume that the P1 and the P2 defects will have the largest contribution to the total tip-sample interaction considering their abundance and strong magnetic moment.

A P1 defect consists of a single nitrogen that shares its electron with a neighboring carbon atom, featuring a simple spin- $\frac{1}{2}$ system. Due to the Jahn-Teller effect, which breaks the T_d symmetry to C_{3v} , the electron is shared predominantly with only one of the four neighboring carbon atoms. It is likely that the nitrogen is ^{14}N ,⁸ which has a spin-1 nucleus. The hyperfine interaction between the atom and nucleus causes a splitting of each e^- -spin energy level into three levels which leads to the ESR spectrum as shown in Fig. 4.1. However, the hyperfine coupling is not purely isotropic. In our experiment we do not know the precise direction of the magnetic field at the P1 center's position, so we assume the directional dipolar coupling to be an unknown deviation from the isotropic term. This leads to a splitting of 92.2 ± 10.8 MHz. An accidental⁹ neighboring ^{13}C atom with spin- $\frac{1}{2}$ can split the levels even more. The level spacing depends strongly on the precise position of ^{13}C . As the abundance of ^{13}C atoms is low, we neglect this effect for now.

P2 centers have a more difficult structure as the system exist of three nitrogen atoms surrounding a vacancy. Although the P2 center was one of the first to be found in EPR-experiments,¹⁰

⁵ Loubser and Wyk 1978

⁶ According to the manufacturer, our sample has < 1 ppm nitrogen impurities. See next section for more information.

⁷ Anderson and Payne 2006

⁸ Natural abundance of ^{14}N is 99.64%.

⁹ Natural abundance of ^{13}C is 1.1%.

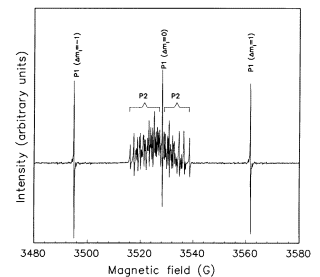


Figure 4.1: The typical 10 GHz ESR spectrum of a type Ia diamond. The P2 lines are absent in the case of Ib diamonds. Figure reprinted from Wyk et al. 1997.

¹⁰ Smith et al. 1959

it was only after a correlation between optical N₃ centers and P₂ was found, that it became clear that a vacancy is part of the system.¹¹ The free electron is most of the time between the vacancy and the single adjacent carbon atom. This leads to a much smaller hyperfine splitting compared to the P₁ center. On the other hand, the electron couples to three ¹⁴N nuclei which causes a splitting of each electron spin state into 54 levels. Due to the close spacing of these levels we will treat the system as a free electron spin with a large line-broadening. Based on Fig. 4.1, we approximate the lineshape to be a Gaussian with 17 MHz standard deviation.

THE RELAXATION TIMES of these P₁ and P₂ centers have been measured last century at various temperatures, magnetic fields, for different samples with changing spin densities, and with different techniques.^{12,13} These numbers do not always coincide. Let us start by noting that at room temperature the relaxation times for P₁ and P₂ are approximately the same, in fact (for homogeneous fields) the T_1 and T_2 times are found to be 2 ms¹² and 3 μ s¹⁴ respectively. Moreover, the T_2 time does not seem to change much as long as the spin density is < 10 ppm, see Fig. 4.2. Similar values are measured for P₁ defects in a later experiment. Takahashi *et al.*¹⁵ did see a more or less constant T_2 time when they lowered the temperature until the thermal energy became smaller than the energy splitting. The last situation leads to much larger T_2 times; there are indications that for low enough temperatures the T_2 converges to 250 μ s.¹⁵ This effects happens upon complete polarization of the e^- -spin ensemble, indicating that the limiting factor for higher temperature is the flipflop rate. On the one hand, in our experiment this rate is suppressed due to the magnetic field gradients, while on the other hand it is enhanced by the movement of the cantilever, thereby opening new ways of spin diffusion.² Spin diffusion, which in crystals is determined by the flipflop rate, is in MRFM effectively a form of longitudinal relaxation as the magnetization can simply diffuse out of the detection

¹¹ Wyk 1982

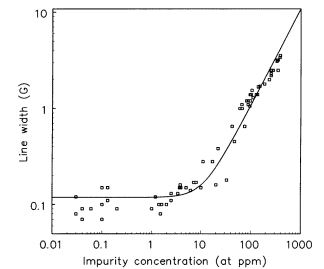


Figure 4.2: The dependence of the line width of the ESR lines of P₁ centers in diamonds on the concentration of P₁ and P₂ paramagnetic centers. *Figure reprinted from Wyk et al. 1997.*

¹² Terblanche and Reynhardt 2000

¹³ Briddon and Jones 1993

¹⁴ Wyk et al. 1997

¹⁵ Takahashi et al. 2008

volume. At low temperatures and homogeneous fields the T_1 time was enhanced to a value in the order of 1 – 100 s for temperatures well below 2 K.¹⁵ Let us take a closer look at the flipflop rate to see if the MRFM experiment changes the T_1 and T_2 significantly.

LET US ASSUME that these flipflops are mostly between a spin and it's nearest neighbor (NN). The distance distribution to this uniform randomly distributed nearest neighbor is, for three dimensions, given by the probability density

$$\mathcal{P}(\text{NN at distance } r) = 4\pi\rho r^2 e^{-\frac{4}{3}\pi\rho r^3}, \quad (4.1)$$

where ρ is the spin density and r the distance between nearest neighbor spins, see also Fig. 4.3. This distribution is a measure of the distance over which the flipflops occur. A possible suppression of the flipflop rate due to magnetic field gradients¹⁶ should be viewed in perspective of these distances.

The probability that two neighboring spins exchange magnetization is proportional to the overlapping of their lineshapes,^{17,18} and is given by¹⁹

$$\Phi_g(\mathbf{r}) = \frac{\int g(\omega)g(\omega - \gamma_s \mathbf{r} \cdot \nabla B)d\omega}{\int g^2(\omega)d\omega}, \quad (4.2)$$

where $g(\omega)$ is the normalized lineshape of the spin without taking flipflops into account. This expression is a rough estimation of the van Vleck's formula without taking into account the coupling, the relative orientation of the B -field and the temperature dependent polarization. The expression above is just enough to determine an average suppression of the flipflop rate for a given field gradient.

Comparing the typical interaction length scales, see Fig. 4.3, to our magnet with a diameter of 2.99 μm , we can assume that the spin sees a spatially *constant* magnetic field gradient G . This simplifies $\mathbf{r} \cdot \nabla B = r \cos(\phi)G$, where we introduced the polar angle ϕ chosen such that the poles are along the direction of the gradient. So, when $\phi = \frac{\pi}{2}$, there is no suppression ($\Phi_g = 1$) while we have an r -dependent suppression otherwise. If we take for example the lineshape of P1 centers,

¹⁶ Namely, spins at a certain distance from each other may have a completely different Larmor frequency and therefore do not interact.

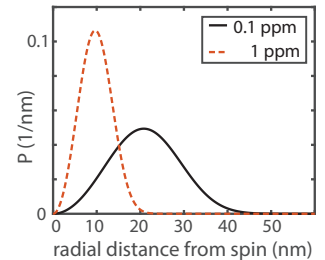
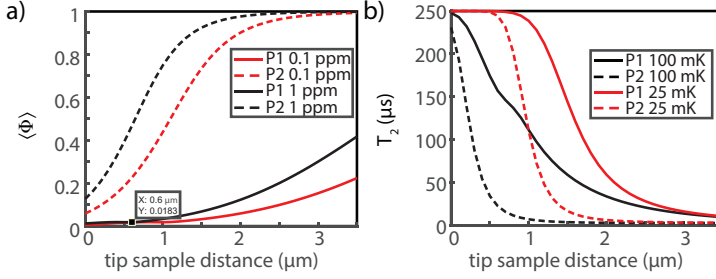


Figure 4.3: Nearest neighbor distance distribution for different spin concentrations in diamond.

¹⁷ Abragam and Hebel 1961

¹⁸ Vugmeister 1978

¹⁹ Budakian et al. 2004



see Fig. 4.5, we find a flipflop probability as shown in Fig. 4.6.

BECAUSE THE FLIPFLOP RATE in the homogeneous field is, under our assumptions, proportional to $\int_{\mathbb{R}^3} d^3r \mathcal{P}$ (NN at distance r), the average flipflop suppression per spin in the inhomogeneous field is given by

$$\langle \Phi \rangle = \frac{\int_{\mathbb{R}^3} d^3r \mathcal{P} (\text{NN at distance } r) \Phi_g(r)}{\int_{\mathbb{R}^3} d^3r \mathcal{P} (\text{NN at distance } r)}, \quad (4.3)$$

where $\langle \Phi \rangle = 0$ means complete suppression. We calculated this factor for spins beneath our MRFM-tip,²⁰ see Fig. 4.4a. The same can be done for P2 centers that we estimate to have a Gaussian lineshape with a standard deviation of about 17 MHz, see dashed lines in Fig. 4.5. Also for P2 centers below the MRFM-tip we show the average suppression in Fig. 4.4a.

THE FLIPFLOP RATE of the P1 spins in the sample is thus suppressed to less than 2% of the original flipflop rate at distances less than 1 μm below the MRFM-tip. The spin-spin relaxation time can be expressed as

$$\frac{1}{T_2} = \Gamma_{\text{flipflop}} + \Gamma_{\text{res}}, \quad (4.4)$$

where Γ_{res} is a residual relaxation rate that is expected to come from C_{13} atoms and estimated to be $\frac{1}{250 \mu\text{s}}$.^{15,21} Γ_{flipflop} is the flipflop rate which is also temperature dependent. Combining our spin suppression with the temperature dependency,¹⁵

Figure 4.4: Flipflop suppression versus the distance of the spins to the magnet surface. The magnet has a radius of 1.5 μm and its magnetization is perpendicular to the displayed distance. a) Here we show the suppression factor where 0 and 1 are full and no suppression respectively. Due to the effectively broad absorption curve, P2 centers are only suppressed within a few hundred nanometer from the surface of the magnet. b) Expected T_2 time where we have taken the suppression $\langle \Phi \rangle$ for a density of 0.4 ppm spins (the same value as is measured in Sec. 4.3) for two temperatures.

²⁰ NdFeB magnet with a diameter of 2.99 μm and a remanence of $\mu_0 M = 1.15$ T.

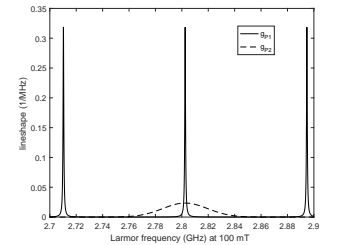


Figure 4.5: Lineshapes of P1 and P2 centers such as used in the calculations. g_{P1} is a triple Lorentzian with each FWHM $\frac{1}{3 \mu\text{s}}$, and g_{P2} a Gaussian with a standard deviation of 17 MHz.

²¹ Laraoui et al. 2012

we find

$$\frac{1}{T_2} = \langle \Phi \rangle \frac{A}{\left(1 + e^{\frac{\hbar\gamma_S B}{k_B T}}\right) \left(1 + e^{-\frac{\hbar\gamma_S B}{k_B T}}\right)} + \Gamma_{\text{res}}, \quad (4.5)$$

where A is a constant of $4 \left(\frac{1}{3 \mu\text{s}} - \frac{1}{250 \mu\text{s}} \right) \approx 1.3 \frac{1}{\mu\text{s}}$. Substituting the results of $\langle \Phi \rangle$ (Fig. 4.4a), we find the T_2 time beneath our cantilever as shown in Fig. 4.4b. Considering that our cantilever has a half period of $\frac{1}{2.2750 \text{ Hz}} \approx 181 \mu\text{s}$, we find that the T_2 time of the P1 spins is larger than the half cantilever period when the distance to the magnet surface is smaller than $0.4 \mu\text{m}$ when at 100 mK, and even $1.2 \mu\text{m}$ at 25 mK. This is important, because some spin manipulating pulses that we will apply²² should coherently manipulate the electron spin for a half period.

4.2 Methods

IN OUR EXPERIMENTS we have used a commercially available diamond sample of $2.6 \times 2.6 \times 0.3 \text{ mm}^3$ size and $< 1 \text{ ppm}$ nitrogen and $< 0.05 \text{ ppm}$ boron concentrations.²³ One surface is polished twice to an $\text{Ra} < 5 \text{ nm}$.²⁴ Cleaning the diamond subsequently in acetone, 2-propanol, fuming nitric acid and hydrofluoric acid makes sure we start the fabrication process with a clean surface and without oxides. We fabricated a Niobium Titanium Nitride (NbTiN) microwave line and a pick-up loop on top of the surface. After fabrication, the sample was exposed to atmospheric conditions for several months. Before mounting the sample it was ultrasonically cleaned in acetone, and thereafter in 2-propanol to remove organics and dust. In future experiments one might again clean the sample with hydrofluoric acid to remove possible oxygen contaminants, since oxygen compounds can contain dangling bonds and thus free electron spins, as we showed in Ch. 3.

THE MICROSCOPE for this experiment consists of a three di-

²² Such as OSCAR protocols, see Sec. 4.5

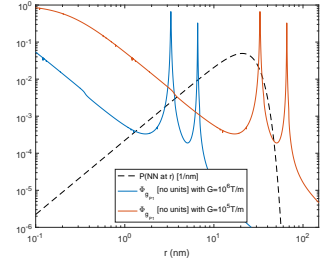


Figure 4.6: Φ_g calculated for a P1-center within a field of 100 mT and a magnetic field gradient of $1 \text{ T}/\mu\text{m}$ (blue curve) and $0.1 \text{ T}/\mu\text{m}$ (red curve). As a reference we plotted the average nearest neighbor distance distribution for 0.1 ppm P1 concentration.

²³ SC Plate CVD, $<100>$, PL from Element Six

²⁴ Second polish: scaife polishing from Stone Perfect

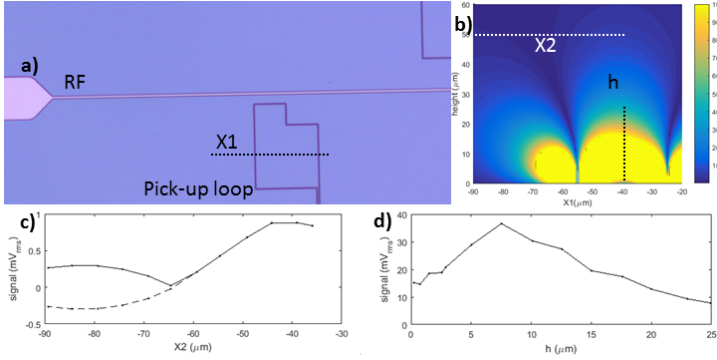


Figure 4.7: The coupling between the MRFM-tip and pick-up loop depends on the relative position. a) A microscope photo of the fabricated structures on diamond. b) Calculated signal intensity in color (arbitrary units) as function of the height between bottom MRFM-tip and sample surface, and as function of the position axis X_1 as depicted in a). For visibility reasons, the signal is cutoff at 100 (yellow). c,d) The measured signal intensity as function of respectively position axis X_1 and h , as denoted in b). When the cantilever passes the lines of the pick-up loop, the Lock-In measured response rotates 180° . If this phase change is taken into account one gets the dashed line in c). The zero crossing of the data taken along X_2 tells the precise position of the cantilever with respect to the pick-up loop.

dimensional positioning system²⁵ that should work down to millikelvin temperatures. The MRFM-chip, with a very soft silicon cantilever and a NdFeB magnet,²⁶ is mounted at the stage such that it can probe the sample. The diamond sample is glued with silver paint to a gold-plated copper sample holder. The holder is cooled via a silver strip that is thermally connected to the mixing chamber of a dilution refrigerator. A thermometer is mounted at the sample holder and a heater halfway the silver strip, such that the sample holder can be homogeneously heated to any temperature between 10 mK and 1 K.

THE MOVEMENT OF THE MRFM-TIP is detected by measuring the magnetic flux change within a pick-up loop fabricated on top of the diamond. The amount of flux change that is picked up depends strongly on the position of the tip, see Fig. 4.7. The flux is transferred to a two-stage SQUID,²⁷ see for more details Sec. 6.3.

The conversion factor C from the movement of the cantilever to the SQUID output voltages can be determined in several ways.²⁸ We determine C by measuring the thermal noise. The surface under the curve of the thermal spectral density S_V should follow the equipartition theorem, i.e.

$$\int S_V df = C^2 \int S_q(2\pi f) df = C^2 \frac{k_B T}{k}, \quad (4.6)$$

where S_q is the spectral density as defined in Ch. 1, f is the

²⁵ CPSHR stage from Janssen Precision Engineering. More info in Sec. 6.5

²⁶ Spring constant cantilever is $k = 48.6 \mu\text{N/m}$ and the ball shaped magnet has a diameter of $2.99 \mu\text{m}$, see Sec. 6.2

²⁷ C6M116 from Magnicon

²⁸ Wijts 2013

frequency, T the temperature and k the spring constant. Of course, for this method the thermal motion of the resonator should exceed the detection noise floor. The spectral density is fitted with a Lorentzian plus an offset to account for the detection noise. The fitting parameters automatically yield the surface under the curve. Doing this at relatively high temperatures (> 100 mK) we may expect that the mode temperature is thermalized with the temperature of the environment. Once C is calculated at a certain position it may be used to check if the mode is also thermalized at temperatures below 100 mK, see Fig. 4.8.

With the conversion factor, one can calculate the detection noise floor as is done in Fig. 4.9 which shows 10 to 100 $\frac{\text{pm}}{\sqrt{\text{Hz}}}$. Surprisingly, the noise floor depends on T even at low temperatures, indicating that the detection noise is not limited by the SQUID.²⁹ Based on the bare SQUID characteristics one could expect a noise floor of at least an order of magnitude less.

It should be noted that for the data as shown in Figs. 4.8 and 4.9, the noise floor is suboptimal as it depends on the position of the tip, however the position of the tip was chosen based on other factors. In the future, optimizing the detection noise and the position of the cantilever could push the noise floor (far) below $1 \frac{\text{pm}}{\sqrt{\text{Hz}}}$.

ONE OF THE DESIGN CRITERIA was to design the mechanical loop from the cantilever holder to the sample as stiff as possible, see also Sec. 6.5. Avoiding the mechanical resonances or moving them to (much) higher frequencies than the cantilever frequency prevents interference with the cantilever mode and thus with the force signal. Unfortunately, resonances outside the mechanical loop can also interfere as these modes accumulate to an interfering signal, such as can be seen in Fig. 4.8 as a deviation of the noise temperature from the bath temperature. The peak at 0.7 K for a tip-sample distance of 20 can be ascribed to the temperature de-

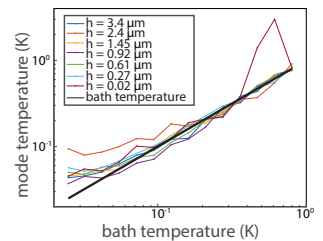


Figure 4.8: Thermalization of the cantilever to the environment versus temperatures for different heights. The data should follow the large black line in case of perfect thermalization, however, the mode temperature saturates at about 50 mK. The data is measured at different positions and is the same as used in Sec. 4.3

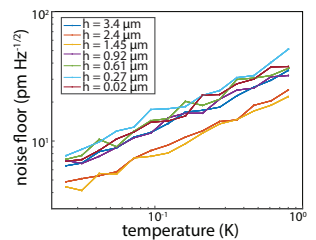


Figure 4.9: Movement detection noise floor around the cantilever's resonance frequency from the same data as Figs. 4.8 and 4.10.

²⁹ Due to the currents through the shunt resistors in a DC-SQUID, one can, as a rule of thumb, expect a saturation of the SQUID noise below 300 mK.

pendent frequency shift that shifts the resonator's resonance frequency over an external resonance peak. The mechanical mode can interfere via pressure waves (sound),³⁰ or via electromagnetic effects.³¹ The disturbing signal can also come from noise sources.³² All of these signals can increase the stored energy in the cantilever motion. If the noise source is coherent, the excess motion can be compensated using feedback schemes employing for example Kalman filters. When the noise source is not coherent (including thermal noise) one can simply feed the signal phase-rotated back into the device.³³ The maximum suppression of the motion is restricted by the detection noise floor.

In this first experiment, however, we practically shifted the resonance frequency to an area where the spectrum was clear of other resonances and where the mode temperature would follow the environment temperature well. The resonance frequency can be shifted due to the repulsion of some trapped flux inside the pick-up loop.³⁴

4.3 *Equilibrium dynamics*

WE APPROACHED THE SAMPLE and measured the cantilevers response at different heights for various temperatures. With this data we can verify if the theory as described in Ch. 2 also applies to the spins in our diamond sample, just like we tested this on silicon in Ch. 3. The temperature and position-dependent shifts in resonance frequency and changes in the Q-factor can tell the densities of spins with T_1 -times comparable to or larger than the resonator period.

After determining the tip-height by softly touching the sample, we started a temperature sequence at a tip-sample distance (height) of 3.4 μm . Each subsequent measurement we moved closer to the sample and also moved in lateral position until the resonator is in a clean spectral area. This was to prevent that external excitations excite the resonator. Due to the tilt of the sample, we introduced here some uncertainty in

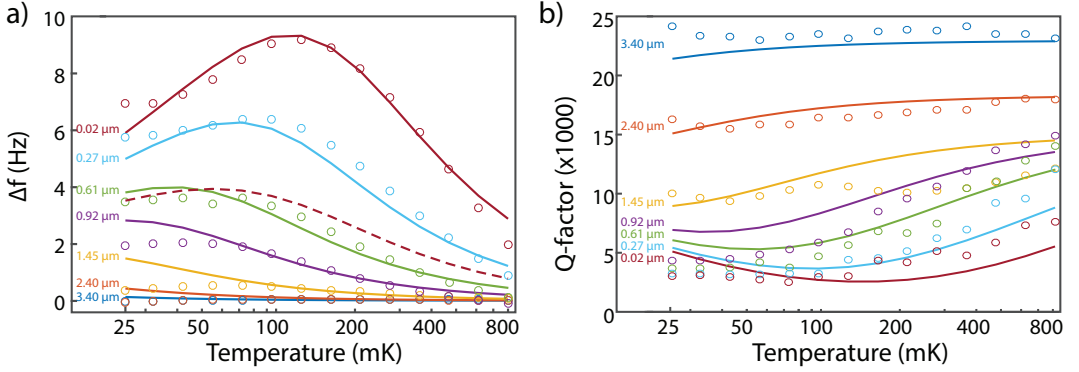
³⁰ e.g. modes in mass spring systems that act as tuning forks for some frequencies

³¹ e.g. resonating wirebonds attached to the sample

³² e.g. turbo pumps(coherent) or the hammering from the pulsetube cooler (not coherent at high frequencies)

³³ Vinante et al. 2012

³⁴ Unlike the repulsion due the Meissner effect of the superconducting line itself, such as Wijts 2013 calculated, we believe our superconducting lines are so small that the largest effect will be due to some trapped flux inside the loop.



the height. As a reference, we measured the height after the measurement series again and found a difference of 200 nm over a lateral distance of about 3 μm and used this value.³⁵ The results were obtained at seven heights between 3.4 μm and 20 nm, and 14 temperatures logarithmically spaced between 25 and 800 mK.

FOR THE FREE ELECTRON SPINS in the bulk of the diamond (P1 and P2 centers) we expect to have a large relaxation time $T_1 \gg \frac{1}{\omega_0}$, as explained in Sec. 4.1. Hence the theoretical function for the shifts due to the bulk spins become

$$\Delta f_{\text{bulk}} = \frac{f_0}{2k} \rho C_{\text{bulk}},$$

$$\Delta \frac{1}{Q_{\text{bulk}}} = 0,$$

$$\text{with } C_{\text{bulk}} = \frac{\mu_e^2}{k_B T} \int_{V_{\text{bulk}}} d^3 r \frac{|\mathbf{B}'_{\parallel \hat{\mathbf{B}}_0}|^2}{\cosh^2\left(\frac{\mu_e B_0}{k_B T}\right)}, \quad (4.7)$$

where $f_0 \equiv \frac{\omega_0}{2\pi}$ is the resonance frequency before the shift, ρ the bulk spin density, μ_e the free electron magneton.

However, we noticed that the Q-factor decreases significantly from > 30000 at a large distance to about 2500 at 20 nm and 71 mK. The decrease is less than what was obtained on silicon in Ch. 3, but still a clear sign that spins must be present with a T_1 similar to $\frac{1}{\omega_0}$. Therefore we include a surface spin density

Figure 4.10: Data (circles) and theory (lines). a) Shows the shift in resonance frequency and b) how the Q-factor changes over temperature, for different heights. For the curves (solid lines) we used the ‘simultaneous’ values from Tab. 4.1. The dashed lines show the contribution from the bulk spins inside the diamond only.

³⁵ The last measurements were closest to the surface, and thus for these it is most important to have a correct value. The last four measurements (0.02 – 0.92) were also laterally close to each other (within 0.4 μm distance).

in our analysis. The additional shifts due to the surface spins are given by

$$\begin{aligned}\Delta f_{\text{surface}} &= \frac{f_0}{2k} \sigma C_{\text{surface}} \frac{(\omega_0 T_1)^2}{1 + (\omega_0 T_1)^2}, \\ \Delta \frac{1}{Q}_{\text{surface}} &= \frac{1}{k} \sigma C_{\text{surface}} \frac{\omega_0 T_1}{1 + (\omega_0 T_1)^2}, \\ \text{with } C_{\text{surface}} &= \frac{\mu_c^2}{k_B T} \int_{\mathcal{V}_{\text{surface}}} d^2 r \frac{|\mathbf{B}'_{\parallel \hat{\mathbf{B}}_0}|^2}{\cosh^2\left(\frac{\mu_c B_0}{k_B T}\right)},\end{aligned}\quad (4.8)$$

where σ is the surface spin density.

THE FUNCTIONS Δf_{bulk} and $\Delta f_{\text{surface}}$ are not completely independent, which makes it hard to fit them simultaneously.³⁶ Therefore we fixed ρ ,³⁷ and fitted σ and the T_1 of the surface spins over the temperature traces, for the each height. Next, we modified ρ until the average fitting error was minimized. The results are given in table 4.1, as well as the other system parameters. As we had to move the resonator laterally to shift

³⁶ The fitting of the functions separately is a very robust procedure and largely independent of the starting point.

³⁷ We first fitted ρ (and the surface spins) at 20 nm height, and used this ρ as an initial value for minimizing the simultaneous fitting error over all traces.

height (μm)	ρ (ppm)	σ (spins/ nm^2)	T_1 surface spins (ms)	f_0 (Hz)
simultaneous	0.40	0.059	0.85	—
0.02	0.4	0.058	0.99	2624
0.27	(0.4)	0.066	0.83	2618
0.61	(0.4)	0.058	0.53	2613
0.92	(0.4)	0.043	0.31	2606
1.5	(0.4)	—	—	2541
2.4	(0.4)	—	—	2629
3.4	(0.4)	—	—	2684

Table 4.1: The fitting values for each trace. Note that ρ was only fitted to all traces simultaneously. For heights $> 1 \mu\text{m}$ the fitting procedure did not work. Note that f_0 is separately calculated from the data.

The second table shows the known system parameters; see also Sec. 6.2.

parameters	k ($\mu\text{N}/\text{m}$)	\odot magnet (μm)	$\mu_0 M$ (T)	μ_s (J/T)
	48.6	2.99	1.3	$9.27 \cdot 10^{-24}$

the resonance frequency to cleaner spectral areas, f_0 changes per height. We calculated f_0 by extrapolating the measured frequency shift data to higher temperatures.³⁸

THE FITTING did not work for heights 1.5 to 3.4 μm , presumably due to the low amount of spins,³⁹ making other long range effects more significant: pure diamond is insulating at any temperature which could lead to charging effects and therefore larger electrostatic interactions⁴⁰ compared to the

³⁸ This produces the same results as when we left f_0 as a fitting parameter, however, calculating f_0 separately seems more robust.

³⁹ According to our interpretation, the diamond has fewer surface spins than found on SiO, resulting in a higher Q in Fig. 4.10 than in Fig. 3.3.

⁴⁰ Kuehn et al. 2006

experiment on silicon.

Next, we choose one initial value for ρ , σ and T_1 for all data, and changed these values to minimize the squared error over all traces simultaneously. The results, as shown in Tab. 4.1, turn out to be independent of the initial values if they are chosen within an order of magnitude difference of the individual fit values. The data and the theoretical lines with the simultaneous fit values are shown in Fig. 4.10.

WE HAVE MEASURED the equilibrium interaction from the MRFM-tip with the spins in the bulk and at the diamond surface. We have found the diamond bulk spin density to be 0.4 ppm, the surface spin density $0.06 \frac{\text{spins}}{\text{nm}^2}$, and a T_1 time of the surface spins of a bit less than a millisecond. We can conclude that the surface spin density on diamond is much lower than on silicon, as expected.⁴¹ Combining this with the knowledge that the sample has been exposed to air for about a year, we anticipate that by cleaning and/or passivating the surface thoroughly, the surface spin density can be reduced to non-disturbing values. What remains is the frequency shift due to the bulk spins only as shown by the dashed lines in Fig. 4.10a. The effect from the bulk spins on the Q-factor should be very small because of the very long T_1 times.

4.4 Spin resonance I: saturation

SATURATION is a fairly simple protocol that works in MRFM for samples with spins that have a T_1 time much larger than the cantilever period.⁴² Referring to Sec. 2.1, we know that when the saturation condition Eq. 2.6 does not apply for sufficiently long times, i.e. $\pi\gamma_e^2 B_1 T_1 g(\omega) \gg 1$, the spins will lose their net magnetization. Here γ_e is the gyromagnetic ratio, and B_1 is the amplitude of an oscillating magnetic field with frequency ω . If we apply this B_1 -field externally, by means of the RF-wire, we can excite a specific resonance slice. The only requirement is that B_1 is strong enough and the

⁴¹ Myers et al. 2014 found a surface spin density of $0.04 \frac{\text{spins}}{\text{nm}^2}$ which is relatively close to our 0.06.

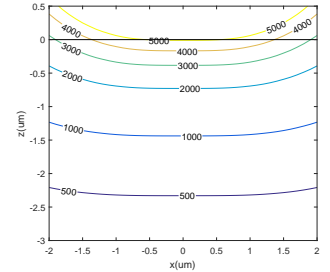


Figure 4.11: Some resonance slices indicated by their free electron spin Larmor frequency in MHz. The distance between sample (at zero height) and the surface of the tip is $0.5 \mu\text{m}$. Here z points out of plane of the sample, and x in the direction of the magnetization.

⁴² Note that for $T_1 = \mathcal{O}\left(\frac{1}{\omega_0}\right)$ we can use the equilibrium dynamics to measure T_1 .

pulse long enough. The precise duration and strength, as well as the magnetic field gradient, will determine the resonance slice thickness, as explained in detail by Wagenaar.⁴³ For now we will assume a constant slice thickness.

FIG. 4.11 SHOWS some of the resonance slices when the tip is positioned at a height of $0.5\ \mu\text{m}$. This is the distance at which we tried the experiment as described in this section and the next.

Within the resonance slice, not all spins contribute equally to the frequency shift of the cantilever; in fact, some spins produce opposite frequency shifts, see Fig. 4.12. Given an RF-frequency, a temperature, a T_1 and a T_2 time, and the other standard system parameters, we can integrate over the surface of the resonance slice to retrieve the total frequency shift per slice thickness. To get the frequency shift for P1 and P2 centers, we convolve this curve with their lineshapes. The results are shown in Fig. 4.14a.

THERE ARE TWO MAJOR PROBLEMS we encountered when we tried to apply this protocol. The first is the signal strength; due to the low density of spins the signal is just below the fluctuations in the measured frequency of the force sensor which are higher than we wanted due to the excess SQUID noise, see Sec. 4.2. This is something that could be solved for a future experiment. Further, we noticed that the RF-source produces large RF-leakage, such that it can still heat up the spin bath.⁴⁴ Finally, applying RF-pulses with frequencies higher than 5 GHz can give comparable frequency shifts as RF-frequencies at for example 4 GHz, which does not agree with Fig. 4.14a. This could be the result of other spin-like level systems at the surface of the diamond that respond to higher frequencies, but it could also be a simpler reason: the direct heating of RF-current or field. We have found that the dissipated power of a pulse in the sample is $0.9\ \mu\text{W}/\text{mA}$, see Fig. 4.13. Although the sample's temperature is kept within a few mK from the setpoint value, the question is if the pulse

⁴³ Wagenaar 2017

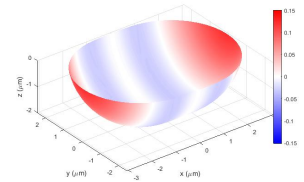


Figure 4.12: Resonance slice indicating which spins give positive or negative frequency shifts. Here, the magnetic field strength is 100 mT, the height is $0.5\ \mu\text{m}$ and T_1 is taken to be infinite.

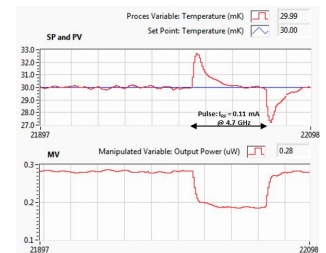


Figure 4.13: Screenshot of experiment to test pulse power. The sample holder is kept at constant temperature (PV) by a PID controller when we apply an RF-pulse. The difference between the heater power (MV) before and during the pulse should be the power the pulse induces.

⁴⁴ The source produces about $-40\ \text{dB}$ leakage, so when the amplitude before the output is set to 10 dBm, but the modulation such that no power should come out, the output still transmits $-30\ \text{dBm}$.

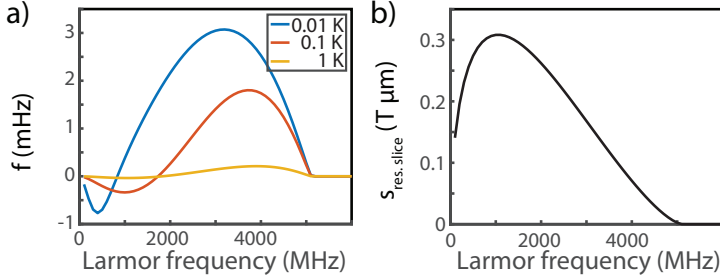


Figure 4.14: Calculated signals for magnetic resonance protocols for a MRFM-tip at a height of 500 nm above our diamond sample. a) Shows the frequency shift per resonance slice of 10 nm thickness after applying a saturation pulse (making the spin-temperature infinite locally). The results are shown for a free electron spin; in this graph the results for P1 or P2 deviate less than 1% from the free electron spin. b) The signals obtained with the protocols as described in Sec. 4.5 are proportional to $\left|B'_{\parallel B_0}\right|$ integrated over a resonance slice surface. Here we show the value of this integral for different resonance slices.

doesn't also drive the local spin temperature outside the resonance slice much higher.

4.5 Spin resonance II: spin coherence

IN THIS SECTION we describe two measurements which directly measure the force from the spins on the cantilever. The two methods in this section are distinguished by the way the spin manipulates the cantilever; the first measures the extra induced movement when the resonator is only thermally excited, while the second measures a frequency shift when it is driven in a Phase-Locked Loop (PLL).

The spin-manipulating protocols for both measurements are based on the principle of adiabatic spin inversion,⁴⁵ which is necessary due to the inhomogeneous B_1 -field. Unlike partial-Rabi-cycle sequences,⁴⁶ an Adiabatic Rapid Passage (ARP) flips the spin, independent of the precise B_1 -field strength as long as it satisfies the following conditions:

$$\frac{1}{T_2} \ll \frac{d}{dt} \tanh \left(\frac{B_1(t)}{B_0(t) - \frac{\omega_{RF}(t)}{\gamma_e}} \right) \ll \gamma_e B_1, \quad (4.9)$$

i.e. a pulse must be designed such that it sweeps through the resonant condition at a rate faster than the T_2 dephasing rate, but slower than the Rabi frequency that is set by the amplitude of the pulse.

For the first measurement (the force measurement) we use

⁴⁵ Slichter 1990

⁴⁶ Such as combinations of $\pi/2$ and π -pulses that are used to measure spin echoes.

ARP in which both the amplitude B_1 and the frequency ω_{RF} of the B_1 -field are changed. For the second measurement, which we will call the frequency shift measurement, we use Oscillating Cantilever-driven Adiabatic Reversals (OSCAR) where ω_{RF} is kept constant while the motion of the magnetic tip causes the spins to be swept through resonance.⁴⁷

⁴⁷ Stipe et al. 2001b

FOR THE FORCE MEASUREMENT, the cantilever is only very sensitive to the Fourier components of the spin force around the cantilever's resonance frequency. More precisely, given the MRFM tip's susceptibility χ , the measured voltage is

$$V_{\text{signal}}(\omega) \propto \tilde{q}(\omega) = \chi(\omega)\tilde{F}(\omega), \quad (4.10)$$

where \tilde{F} is the Fourier transform of

$$F(t) = \langle \boldsymbol{\mu} \rangle_{ARP} \cdot \mathbf{B}' \text{sgn}(\cos(\omega_S t)), \quad (4.11)$$

$$\approx \frac{\pi}{4} \mu_{ARP} \left| \mathbf{B}'_{\parallel \hat{\mathbf{B}}_0} \right| \cos(\omega_S t). \quad (4.12)$$

Here μ_{ARP} is the net magnetization and ω_S the frequency of the spin rotating 360° . As a spin will flip 180° during a single ARP, two pulses are needed to return the longitudinal magnetization to equilibrium position.⁴⁸ In the last step we have taken the Fourier components around ω_0 , which is valid when we choose $\omega_S \sim \omega_0$. For the total signal we integrate over the resonance slice and find⁴⁹

$$q(t) = \int_{\mathcal{V}_{\text{res.slice}}} \rho \mu_{ARP} \left| \mathbf{B}'_{\parallel \hat{\mathbf{B}}_0} \right| d\mathcal{V} \times \frac{1}{k} \left(2 \frac{\omega_0 - \omega_S}{\omega_0} \cos(\omega_S t) + Q \sin(\omega_S t) \right), \quad (4.13)$$

where ρ is the bulk spin density. Thus when we choose the pulse sequence such that the spin force follows a reference sinusoid with $\omega_S = \omega_0$, then all spin signal will be in the quadrature component (Y) of the measurement signal, while the in-phase component (X) only contains thermal motion. Before the sequence, the X and Y components contain on average the same amount of thermal energy (i.e. $\langle Y^2 \rangle = \langle X^2 \rangle$).⁵⁰ Therefore, during the pulse sequence, the pure spin signal is $\sqrt{\langle Y^2 \rangle - \langle X^2 \rangle}$.

⁴⁸ Thus the pulse frequency is not equal to ω_0 (but $2\omega_0$) and therefore there should be little crosstalk between RF-pulse and cantilever.

⁴⁹ Similar to the derivation of Eqs. 1.5-1.6. See also Peddibhotla 2013

⁵⁰ Here energy means signal squared.

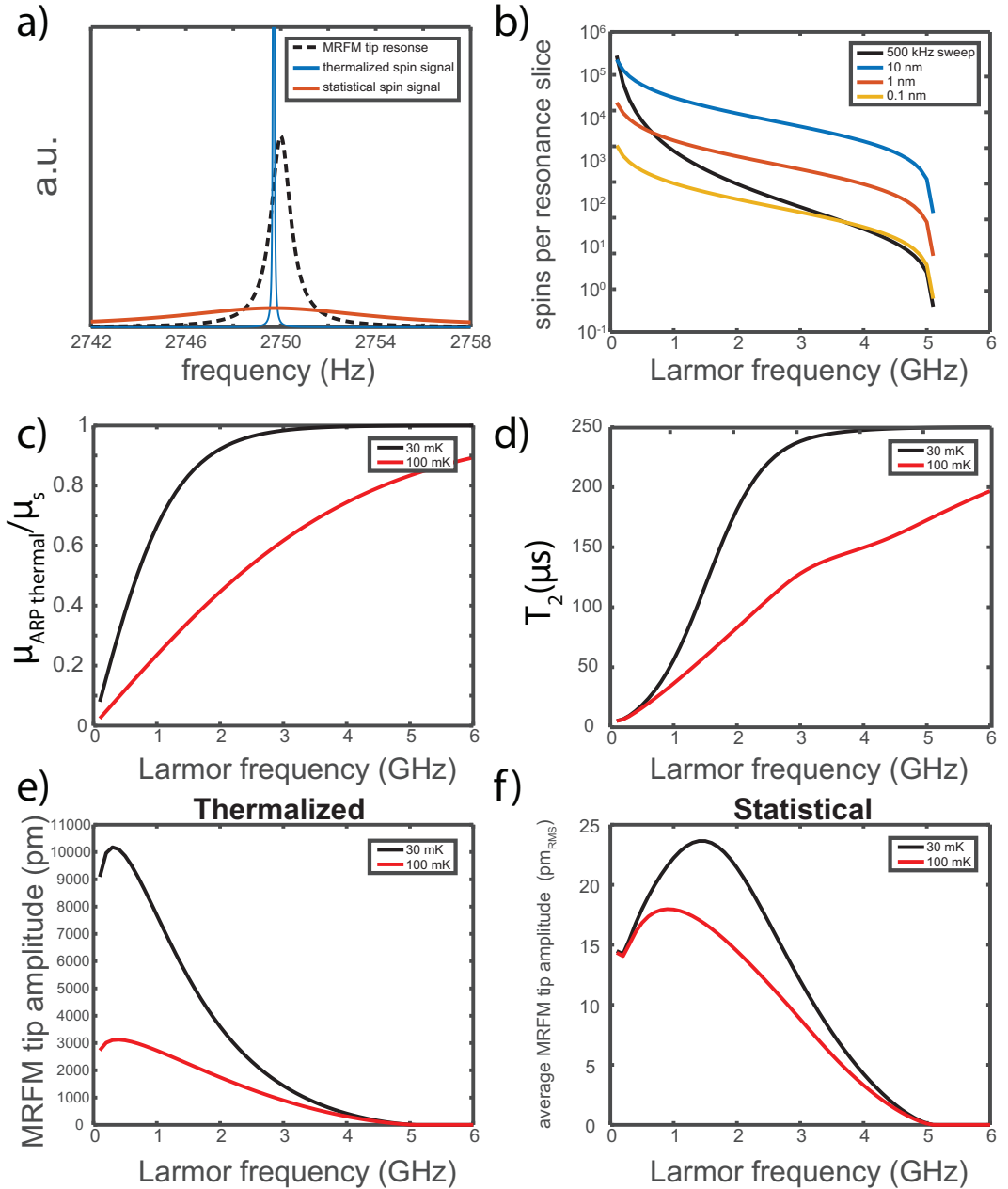


Figure 4.15: Theoretical expectations of the ARP experiment outcome. a) Spectral densities of the signals of thermally and statistically polarized spins compared to the linear response of the MRFM-tip. ω_S is set to 2749.9 while ω_0 is 2750. b) Number of spins in a resonance slice of fixed thickness, and a resonance slice where the width is determined by the frequency sweep range of the ARP pulse (500 kHz FWHM in the first ARP experiments). c) Net magnetization of thermalized spins as function of the resonance slice's Larmor frequency. d) Estimated T_2 time which is calculated as described in Sec. 4.1. e) The expected MRFM amplitude if the spin inversion autocorrelation time is longer than the duration of a single experiment e.g. the thermally polarized regime. f) Expected RMS averaged amplitude of the MRFM tip if the magnetization is statistically determined.

The advantage of measuring the energy X^2 and Y^2 rather than X and Y is that the sign of initial magnetization does not matter. Therefore, this method still works if the initial magnetization is not determined by thermalization but by statistical polarization. This statistical magnetization can be the dominant term for the net magnetization in small ensembles at temperatures $k_B T > \mu_s B_0$.⁵¹ So, although we will try to stay in the thermalized regime, statistical polarization might help us out if the spin temperature becomes too high.

⁵¹ Mamin et al. 2003

SO FAR, we assumed that both conditions of Eq. 4.9 are satisfied. In our experiment, however, we use ARP pulses of length $\sim \frac{1}{2f_0} \approx 180 \mu\text{s}$. Comparing this with the T_2 values in Fig. 4.4b, we notice that our ARP protocol with pulses this long, and at 100 mK, should only work within about $0.5 \mu\text{m}$ distance from the tip. More precisely, for spins at resonance, the net magnetization after an ARP pulse is $|\mu_{after}| = |\mu_{before} e^{-\frac{K}{T_2}}|$,⁵² where K is a pulse shape dependent parameter and proportional to the single pulse duration.⁵³ The success rate, or fidelity, of one spin inversion is thus $e^{-\frac{K}{T_2}}$. However, we apply a series of these inversion pulses. A typical sequence length is $\frac{Q}{f_0} \approx 1$ s. Longer sequences would not be beneficial as the resonator cannot collect more spin signal due to the cantilever's relaxation time (and because of reasons explained below). On the other hand, shorter sequences do not use the full capacity of the resonator.⁵⁴ In our case, this means we have to apply a series of about 6000 spin inversion pulses. To ensure that a significant amount of net magnetization will create a spin signal during the pulse sequence, a single spin inversion fidelity should be about 0.9999. This means that to measure the pure spin signal curve of Fig. 4.14b, the pulse dependent parameter K must be smaller than $10^{-4} T_2$ for all spins in the resonance slices that we want to measure.

⁵² Norris et al. 1991

⁵³ Hajduk et al. 1993

⁵⁴ Another way to see this is that for series shorter than $\frac{Q}{f_0}$ the spectral leakage of the spin signal is wider than the resonator's resonance peak, so the spin signal is not optimally transduced.

During our first ARP experiments,⁵⁵ it is not likely that we satisfied this condition. In fact, based on similar pulse shapes⁵³ we estimate K to be as large as $30 \mu\text{s}$, while $250 \mu\text{s} > T_2 > 3 \mu\text{s}$ as explained in Sec. 4.1. This means that soon after the

⁵⁵ Upon finishing this thesis consecutive experiments are performed that might have better conditions.

pulse sequence is started, the average thermal net magnetization is reduced to insignificant values. However, statistical polarization helps us out as the average magnetization amplitude⁵⁶ due to statistical polarization would be about $\mu_{ARP} \propto \sqrt{N}\mu_s$, where N is the number of spins inside the resonance slice. The slice thickness can be set by the frequency sweep range of the pulse with a lower limit set by the resonator's RMS displacement. In our case this limit is on the order of 0.1 nm due to thermal excitations, but can increase during the pulse due to the force of the spins driving the resonator. See Fig. 4.15b for a comparison of the number of spins per resonance slice when the thickness is fixed or set by a frequency sweep of 500 kHz.

When spin inversions are imperfect, not only does the amplitude of the spin signal change, also the force becomes distributed over a frequency range due to the limited autocorrelation time. As the fidelity of a single spin inversion is e^{-K/T_2} and the spin is flipped with frequency $2\frac{\omega_s}{2\pi}$, the net magnetization averages out as $\langle \mu_{ARP}(0) \mu_{ARP}(t) \rangle \propto e^{-t/\tau}$ with $\tau \equiv \frac{\pi T_2}{\omega_s K}$ the autocorrelation time, and where we assumed $T_1 \gg \tau$. The autocorrelation time tells us that the spin signal has a frequency width of $1/\tau$ and also that if it is larger than the ARP sequence duration, we are in the thermal magnetization regime. While if τ is much smaller than the sequence duration, we are in the statistical polarization regime.

Next, we calculate the autocorrelation of the single-spin force of Eq. 4.12 by substituting the average autocorrelation of a single spin into μ_{ARP} that we have found to be $\mu_s^2 e^{-t/\tau}$ for $t > 0$. We can use the Wiener-Khinchin theorem to find the force power spectral density (averaged for a single spin) to be

$$S_F(\omega) = \left(\frac{\pi}{4} \mu_s \left| \mathbf{B}'_{\parallel \hat{\mathbf{B}}_0} \right| \right)^2 \tau \frac{1 + i\omega\tau}{1 + (\omega_s\tau)^2 - (\omega\tau)^2 + 2i\omega\tau} \quad (4.14)$$

$$\approx 0.4 \tau \left(\mu_s \left| \mathbf{B}'_{\parallel \hat{\mathbf{B}}_0} \right| \right)^2 \quad \text{for } \omega \approx \omega_s. \quad (4.15)$$

We only need the value of the force around the resonance peak of the transducer (the MRFM-tip). The force signal is

⁵⁶ With average magnetization amplitude we mean the root mean squared (RMS) magnetization. We naturally measure the RMS magnetization if we take the mean of the measured X^2 and Y^2 signal (and take the square root afterwards).

spectrally widespread compared to the MRFM-tip if $\tau \ll \frac{Q}{\omega_S}$ and therefore can be approximated linearly, see Fig. 4.15a. The approximation is valid up to a factor of $\sqrt{2}$ depending on the precise value of τ , which should be accurate enough for our heuristic approach.

The derivation of the power spectrum of the MRFM-tip movement is similar to Eqs. 1.7-1.11, and leads to

$$S_q(\omega) \approx 1.4 \frac{T_2}{K} \frac{Q}{k^2} \int_{\mathcal{V}_{res.slice}} \rho \left(\mu_s \left| \mathbf{B}'_{\parallel \hat{\mathbf{B}}_0} \right| \right)^2 d\mathcal{V} \times \frac{\frac{\omega_0}{2\pi Q}}{(\omega_0 - \omega)^2 + \left(\frac{\omega_0}{2Q} \right)^2}. \quad (4.16)$$

Note that in contrast to Eq. 1.11 the phase is still well defined $\phi(\omega) = \text{atan2} \left(\frac{-\omega_0 \omega_S}{Q}, \omega_0^2 - \omega_S^2 \right)$ with respect to the phase of the spin force. For the total spin signal of the resonance slice we have to integrate over the power spectrum. The last line of Eq. 4.16 integrates to unity, leaving us with the first line only.

To conclude the differences between the statistical and thermally polarized experiments, we find that the regime is determined by the autocorrelation time of the net magnetization $\tau = \frac{\pi T_2}{\omega_S K}$ during the ARP experiment. If τ is longer than the ARP experiment duration, which wisely would be chosen of the order $\frac{Q}{\omega_0}$, then we are in the thermally polarized regime and Eq. 4.13 applies. Then the signal is proportional to the number of spins N in the resonance slice (Fig. 4.15b), to the gradient of B_0 in the direction of the movement of the resonator (Fig. 4.14b), and to the thermal polarization (Fig. 4.15c), which ultimately leads to Fig. 4.15e. The statistical regime applies when $\tau \ll \frac{Q}{\omega_0}$ and Eq. 4.16 applies. The final signal, the square root of the power spectrum of Eq. 4.16 integrated over frequency, is proportional to \sqrt{N} (square root of Fig. 4.15b), the RMS of gradient of B_0 in the direction of the movement of the resonator, and the square root of the T_2 time (square root of Fig. 4.15d) which leads to Fig. 4.15f.

OUR FIRST ARP EXPERIMENTS were carried out at a height of 500 nm and a distance of 27 μm from the RF-wire. We

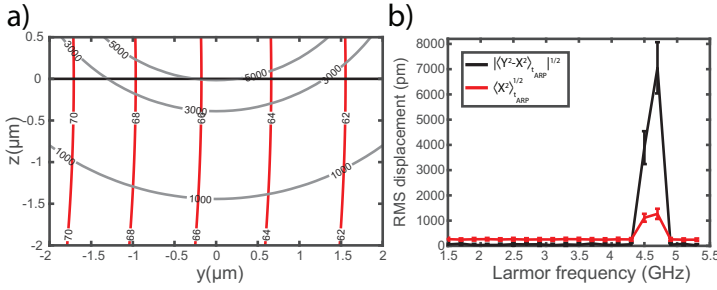


Figure 4.16: The first ARP experiments. a) The equipotential lines of constant B_1 -field in kHz (red) and, as reference, some resonance slices with constant Larmor frequency in MHz (gray). b) The measured spin-force signal in black, and the average in-phase signal in red. If the ARP experiment was done in the thermal regime, red is the thermal motion/ $\sqrt{2}$ plus the spectral leakage due to the finite pulse sequence duration.

applied ARP pulses of 0.63 mA through the RF-wire creating $\gamma_e B_1 \approx 66$ kHz at the position of the resonance slices, see Fig 4.16d. This B_1 is high enough to satisfy the last condition of Eq. 4.9 for all resonance slices.

For most Larmor frequencies we find that $\langle Y^2 \rangle = \langle X^2 \rangle$; except for two data points: 4.5 and 4.7 GHz have a significant signal inside the quadrature part. Reasons for these two points to appear could be: that we are suddenly in the thermal regime due to the higher field and field gradient (rather wishful thinking), that the spins from the surface add to the spin signal (not likely due to small T_2 of surface spins), resonances in the RF-wire (the peak is too broad for a single resonance in a superconducting circuit), heating of the system (not clear why only at this frequency), or that the RF leaks into the SQUID device and creates nonlinearities. Recent experiments that are outside the scope of this thesis tend to support the last hypothesis. The other data points (black points in Fig. 4.16b) are too far below the thermal signal (red signal) to show any significant spin signal.

As this analysis was only performed after the experiment, a closer determination of the spin signal with ARP is left for consecutive experiments. The RF-current lines can handle several mA, providing enough freedom to shorten the ARP pulses⁵⁷ and reveal more of the theoretical curve of Fig. 4.15e or f. Also phase measurements can be optimized by doing the quadrature measurements faster than τ and using the MRFM-tip's frequency-phase relation to suppress the influence of the thermal motion.

⁵⁷ This can be used to optimize the ARP pulse shape and thereby lower the parameter K by one or two orders of magnitude.

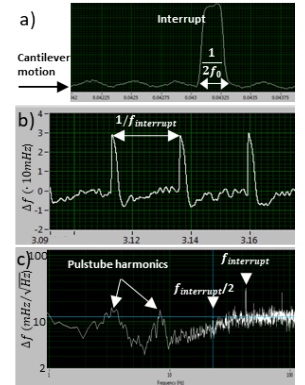


Figure 4.17: Screenshot of live data capturing during iOSCAR protocol. a) SQUID signal in time-domain, showing the cantilever movement. b) PLL frequency tracking in time domain. The sudden interrupt of the RF-signal messes up the PLL for a short while. c) PLL frequency in frequency domain. The spin signal is in the small peak at $f_{\text{interrupt}}/2$.

DURING THE OSCAR PROTOCOL the cantilever is driven with several nanometers amplitude to use the gradient of the magnet to invert the spin each time the magnet 'passes by', causing the spin to lock, or antilock to the cantilever motion.⁵⁸ Turning the RF off for half a period should switch the locked spins to antilock and vice versa, and thereby the resonance frequency changes as there is usually an imbalance between the amount of locked vs antilocked spins. Doing this regularly and measuring the periodic change of the resonance frequency is called iOSCAR.⁵⁹ The RF can also be pulsed (piOSCAR)⁶⁰ to narrow the resonance slice, which in a follow-up experiment might also be done in view of the short T_2 time. Let us for now stick with iOSCAR. The frequency shift due to a single spin is given by⁵⁸

$$\delta f \approx \frac{2f_0}{\pi k A} \mu_{eq} \left| \mathbf{B}'_{\parallel \hat{B}_0} \right|, \quad (4.17)$$

where A is the resonator's amplitude. Of course, this δf has to be integrated over all the spins inside the resonance slice. When the interrupting frequency is $f_{\text{interrupt}}$, the magnetization changes with $f_{\text{interrupt}}/2$, and the amplitude of the frequency shift at $f_{\text{interrupt}}/2$ gives δf , see Fig. 4.17. Theoretically, this δf should follow the curve as given in Fig. 4.14b. However, for now the data as retrieved in Fig. 4.17, was too noisy to be useful. It is likely that one has to go to very short⁶¹ piOSCAR pulses, to invert the spins within T_2 .

⁵⁸ Lee et al. 2012

⁵⁹ Rugar et al. 2004

⁶⁰ Cardellino et al. 2014

⁶¹ With respect to the cantilever period.

4.6 Conclusions and outlook

COMPARED TO PRECEDING EXPERIMENTS,^{62,63} we have made notable progress in sending large RF-currents, fast temperature monitoring and controlling, and we solved the problem of very large frequency shifts.⁶⁴ However, the MRFM-experiment on diamond has also shown several points that need to be fixed or optimized such as the SQUID excess noise, RF-leakage that heats up the spin bath, and the vibrations and resonances that drive the resonator. The first two can be easily solved, but the latter needs a much better

⁶² Vinante et al. 2011a

⁶³ Usenko et al. 2011

⁶⁴ Wijts 2013

vibration isolation, and probably a new MRFM-design.⁶⁵

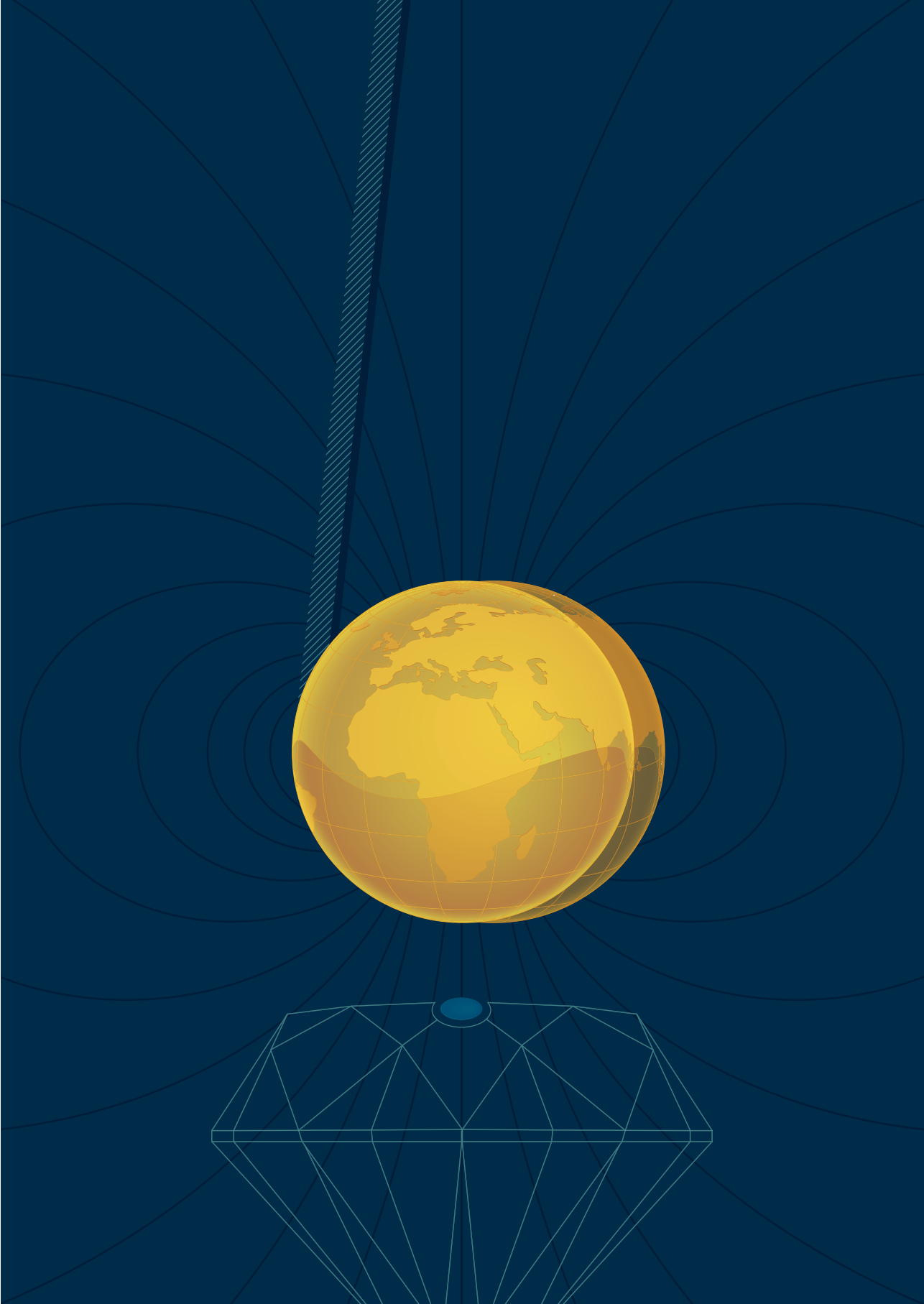
The experiment so far has been successful in obtaining spin density information of the bulk *and* the surface spins on diamond. Furthermore, we have calculated the influence from the limited T_2 relaxation time in ARP experiments. We suggest that for future experiments pulse shapes are used that ensure that the spin inversions take place with much higher fidelity.

To conclude the analysis of our resonance experiments we might say that an important factor is the quality of the spin lock which determines the bandwidth over which the spin signal is spread out. The quality of the spin lock is to a large degree determined by the duration of a single spin inversion which determines the K parameter. The duration is limited by the strength of the B_1 field. Furthermore the quality of the spin lock can be deteriorated by possible disturbances of spins in the vicinity. In the single spin experiment of Rugar et al. 2004 an excellent spin lock of longer than 1 second was achieved with a B_1 field of 0.3 mT. In their sample of quartz, the spins were generated by gamma ray irradiation with an estimated spin density of $10^{13} - 10^{14} \text{ cm}^{-3}$, or an average spin-spin distance of around 300 nm. This is significantly farther apart than the 20 nm separating the nitrogen spins in our diamond.

In the experiment of Cardellino et al. 2014 the spins implanted as a wire in diamond were studied. At 6 ppm or 10^{18} cm^{-3} (rather than our 0.4 ppm) these spins were significantly closer to each other (5 – 10 nm) than in our experiment, however, in the iOSCAR protocol used, they could lock the spins to the cantilever motions for more than 20 ms, even though the flip-flop time was 0.2 ms.

In our experiment we are able to generate B_1 fields larger than 0.1 mT at 1 micron distance from our superconducting RF wire. We believe that we can generate spin locks for at least 20 ms. This would mean the spin signal will be spread out over a bandwidth of well below 50 Hz and therefore a single spin could become detectable in a single shot experiment.

⁶⁵ More on this in Sec. 6.5



5 Gravitational decoherence of NV-resonator systems

"Science itself is badly in need of integration and unification. The tendency is more and more the other way... Only the graduate student, poor beast of burden that he is, can be expected to know a little of each. As the number of physicists increases, each specialty becomes more self-sustaining and self-contained. Such Balkanization carries physics, and, indeed, every science further away from natural philosophy, which, intellectually, is the meaning and goal of science."

quote Rabi 1970

AS DESCRIBED in Ch. 1, the goal of the proposal that led to this thesis is clear; an experiment that verifies or falsifies gravitational collapse models would have major implications for the physicist's perceived worldview. Besides that an experiment like this would enlighten the almost century-old discussion about the correct interpretation of quantum mechanics, it could also point towards the right way to unify the theories of gravity and quantum mechanics. As Rabi states in the quote above, science needs unification but tends to disperse into different fields, branches, and subbranches.

To design such an experiment we need to work the other way around and collect the expertise of many branches to overcome technical and theoretical challenges. As Rabi also mentioned, a PhD-student can be expected to extract the information of all the necessary fields, albeit that he or she might have too little time to design a well defined exper-

iment. Therefore this chapter is different from the others: instead of trying to draw firm conclusions we end most sections with an emphasized question, which is meant to guide successive research.

IN THE FIRST three sections we will discuss the effect of the possible gravitational collapse effect onto the MRFM-resonator. The first section will review the original gravitational collapse theory as founded by Diósi and Penrose.^{1,2} Next, we will suggest a modification predicting that the boundaries between quantum and classical mechanics occur for much smaller masses. The third section will review the proposed^{3,4} effect of heating due to spontaneous collapse of the wave function.

The last two sections focuses on the experiment as suggested by Van Wezel and Oosterkamp 2012,⁵ in which a well controlled spin should entangle with a massive resonator, hence creating a massive superposition. Sec. 5.4 will point out the relevant quantum mechanical interactions in this experiment that need to be understood very well to be able to measure a deviation from conventional quantum mechanics. Moreover, the quantum interactions are needed to push the system out of the safe regime of quantum mechanics. Finally, in Sec. 5.5 we describe the possibilities to concretely construct the experiment.

As this is the last scientific chapter regarding the main subject of this thesis, we will make up the balance in Sec. 5.6 and also look ahead in this last section.

¹ Diósi 1989

² Penrose 1996

³ Bassi et al. 2013

⁴ Vinante et al. 2016

⁵ Wezel and Oosterkamp 2012

5.1 *Gravitational collapse*

IN THE COPENHAGEN INTERPRETATION of quantum mechanics, if one measures an observable of a quantum state, the classical measurement apparatus lets the wave function collapse. This means that the quantum state is reduced to an

eigenvalue of the observable.⁶ It is, however, not clear what a classical apparatus precisely does or what classical even means. If the large amount of degrees of freedom in this apparatus are entangled with the measured state, does that mean that for each possibility there is another reality? Or does the state collapse, i.e. it chooses one reality? In the next section we will discuss that the first interpretation is not falsifiable, while collapse mechanisms lead to non-unitary quantum mechanics.

THE QUALITATIVE SOLUTION suggested by Diósi,¹ Penrose,⁷ and many others,^{3,8,9} is that the concept of gravity induces non-unitary behavior, which then leads to spontaneous collapse. Note that we work at non-relativistic speeds and in an almost flat spacetime. In other words, our physics consists of non-relativistic quantum mechanics and a weak gravitational field, albeit we will investigate what might happen when the gravitational field is generated by a mass in superposition. This conservative field can be described by the gradient of the gravitational potential $\Phi(\mathbf{r})$. For weak fields, the potential can be written as a first order perturbation to the flat spacetime.¹⁰ Hence the local elapsed time interval $d\tau$ (proper time) becomes

$$d\tau = \left(1 + \frac{\Phi(\mathbf{r})}{c^2} + \dots\right) dt, \quad (5.1)$$

where c is the speed of light and dt the time interval of an infinitely far away observer (coordinate time).¹¹ As Φ is always negative at finite distance of a massive object, the proper time is always slower than the coordinate time.

The gravitational potential is related to the mass distribution by Poisson's equation, which in integral form can be written as

$$\Phi(\mathbf{r}) = -G \int_{\mathbb{R}^3} d^3r' \frac{\rho(\mathbf{r}')}{|\mathbf{r} - \mathbf{r}'|}, \quad (5.2)$$

where G is the gravitational constant.

⁶ In the case of a perfect position measurement, which we will be interested in, the wave function collapses to a delta function.

⁷ Penrose 2014

⁸ Oosterkamp and Zaanen 2013

⁹ Rademaker et al. 2014

¹⁰ Carroll 2003, Sec. 4.1

¹¹ The far away observer and the local experiment do not move (significantly) with respect to each other, so special relativistic effects can be neglected.

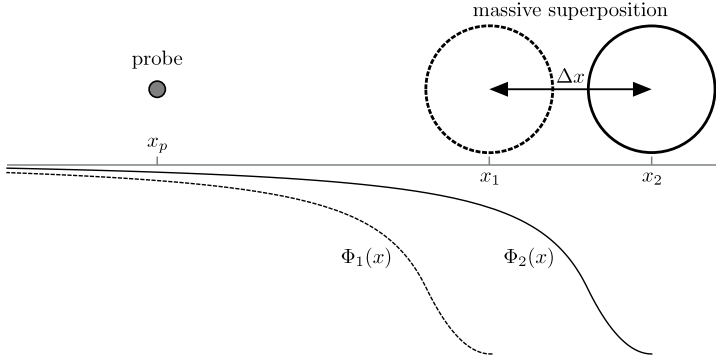


Figure 5.1: A massive ball is brought into a superposition of states at positions x_1 and x_2 . This leads to a superposition of the gravitational potentials $\Phi_1(x)$ and $\Phi_2(x)$. Is the probe particle at position x_p in a superposition of spacetimes or does it experience a superposition of time evolutions? Figure reprinted from Rademaker et al. 2014.

The mass density ρ is trapped inside the gravitational potential as it costs work to remove each bit of mass. The total work to move each infinitesimal part from its current position to infinity is, up to a minus sign, the so called binding energy, E_b , which is given by

$$\begin{aligned} E_b &= \frac{1}{2} \int_{\mathbb{R}^3} d^3r \Phi(\mathbf{r})\rho(\mathbf{r}) \\ &= -\frac{G}{2} \int_{\mathbb{R}^3} d^3r \int_{\mathbb{R}^3} d^3r' \frac{\rho(\mathbf{r})\rho(\mathbf{r}')}{|\mathbf{r} - \mathbf{r}'|}. \end{aligned} \quad (5.3)$$

To see what parameters need to be optimized for measuring a gravitationally induced collapse of the quantum state, we need to ask ourselves how gravity sees the mass of the wave function. In quantum mechanics a particle is assigned a mass, but it does not tell how this mass is distributed over space. In other words, for choosing the right experiment we should know how the gravitational potential $\Phi(\mathbf{r})$ and a wave function $\Psi(\mathbf{r})$ are connected. However, here we encounter the 100 year old conundrum of the unfeasible unification of theory of gravity and quantum mechanics. As there is no answer known to how the gravitational potential is formed around a quantum state, let us revisit some possibilities. To stay close to our MRFM-experiment, we will evaluate the possibilities on a massive ball that is in a Schrödinger cat state as shown

in Fig. 5.1. Hence, we could write the quantum state as

$$|\Psi\rangle = \frac{1}{\sqrt{2}} (|1\rangle + |2\rangle), \quad (5.4)$$

where $|1\rangle$ and $|2\rangle$ correspond to the states with the center of mass of the ball at positions x_1 and x_2 respectively. If we assume that gravity does not know about 'mass distributions of quantum states', but rather is constructed for each possible outcome, we end up with two gravitational fields: Φ_1 and Φ_2 respectively.

It was argued by Penrose,² that an uncertainty in the gravitational binding energy occurs when the mass distribution is in a superposition. The lifetime that is associated with this state due to this uncertainty is guessed by dimensional analysis to be

$$\text{lifetime} = \frac{\hbar}{|E_\Delta|}. \quad (5.5)$$

The uncertainty energy E_Δ is some energy measure that can be related to the gravitational binding energy difference between the two possible outcomes of a two-state superposition

$$E_\Delta = -4\pi G \int_{\mathbb{R}^3} d^3r \int_{\mathbb{R}^3} d^3r' \frac{(\rho_1(\mathbf{r}) - \rho_2(\mathbf{r})) (\rho_1(\mathbf{r}') - \rho_2(\mathbf{r}'))}{|\mathbf{r} - \mathbf{r}'|}, \quad (5.6)$$

where $\rho_1(\mathbf{r})$ and $\rho_2(\mathbf{r})$ are the mass densities that correspond with Φ_1 and Φ_2 respectively. A similar quantity was suggested by Diósi¹ a few years earlier. In Fig. 5.2 we plotted $\frac{\hbar}{E_\Delta}$ for our NdFeB magnetic particle of 1.5 μm radius as a function of superposition distance Δx . The Δx values shown here are way too large to be feasible, and the lifetimes far too long to be measured with current techniques. *If this is the macroscopic boundary of quantum mechanics, why is it so incredible hard to get the MRFM-tip into a quantum superposition even on millisecond timescales?* An often-heard answer argues that this is due to the coupling to environmental degrees of freedom which makes it difficult to prove superposition in an interference experiment. However, this does not explain the single

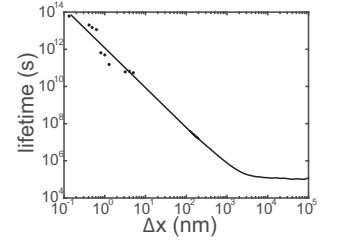


Figure 5.2: Numerical calculation of the Penrose collapse time for a magnet in a position cat state with a separation of Δx between the two states of which the total wave function is a superposition. The ball is of diameter 3 μm , similar to the size of the magnet as used in our MRFM experiment. For Δx values larger than $\sim 3 \mu\text{m}$ the two states do not overlap anymore. The line starts to flatten due to the trade-off of larger separation between the two states and weaker gravitational field that is generated by one state around the other. The shown points at small Δx that deviate from the straight line asymptote are due to numerical errors because of the large difference in scale between object size and Δx . Around these points the straight line is merely a guide to the eye.

outcome of measurements of quantum states.¹² In the next section we will argue that the rate might be much faster than in Eq. 5.6 as not only the mass from the object itself counts but also all other masses that feel the gravitational potentials from the massive quantum object.

¹² The environmental decoherence can explain the diagonalization of the density operator, however it does not explain why the remaining diagonal values are *probabilities*, i.e. why we have only one outcome per measurement.

5.2 *Probing the instability of a quantum superposition of time dilations*

SO FAR we have looked at the massive object in superposition itself. However, it also changes the spacetime at the position of other objects. Compared to Diósi's and Penrose's ideas, including the surrounding mass is of vital importance. We demonstrate in this section on what typical timescales ordinary quantum mechanics might fail when not only the gravitational self energy of the object in superposition itself, but also the surrounding mass is taken into account. For calculating the time evolution of objects near a mass in superposition in the quantum domain, we should have a valid theory of quantum gravity. However, such a theory does not yet exist. Therefore, in order to find the typical timescale on which the quantum world becomes classical, we follow the reasoning from Oosterkamp and Zaanen 2013¹⁶ where, based on a gedankenexperiment, they argue at which timescale the gravitational time dilation might force a collapse of the wavefunction, which turns out to be similar to the Diósi-Penrose interpretation. In contrast to that paper, we will include the effect of all surrounding mass.

This section is based on and continues on: Rademaker, L *et al.* Probing the Instability of a Quantum Superposition of Time Dilations. arXiv:1410.2303 [quant-ph] (2014).

CONSIDER a probe particle at position x_p as shown in Fig. 5.1. Later on we will assume that the surrounding mass exists of many noninteracting probe particles. If the probe particle is subject to a time-independent Hamiltonian, its time-

dependent wave function can be written as

$$|\Psi_p(t)\rangle = e^{-i\hat{H}\tau/\hbar} |\Psi_p(0)\rangle. \quad (5.7)$$

Here \hat{H} is the Hamiltonian (without gravity) and τ is the proper time from Eq. 5.1 which is equal to t in flat space. But spacetime is not flat and the neighboring massive object causes the probe particle's time to run slower. The problem is that a cat state of the massive object causes the proper time to be in superposition as well.

Let us consider the total quantum state of the probe particle $|\Psi_p\rangle$ and that of the massive object in superposition $|\Psi_M\rangle$ (with $|\Psi_M(0)\rangle = \frac{1}{\sqrt{2}}(|1\rangle + |2\rangle)$), where we assume that $|\Psi_p\rangle$, $|1\rangle$, and $|2\rangle$ are eigenstates of the position operator. When the particles do not interact¹³ the total quantum state is

$$|\Psi(t)\rangle = \frac{1}{\sqrt{2}} e^{-i\hat{H}_M\tau_M/\hbar} \left(|1\rangle e^{-i\hat{H}_p t \left(1 + \frac{\Phi_1(x_p)}{c^2}\right)/\hbar} + \right. \quad (5.8) \\ \left. |2\rangle e^{-i\hat{H}_p t \left(1 + \frac{\Phi_2(x_p)}{c^2}\right)/\hbar} \right) |\Psi_p(0)\rangle.$$

Note that the gravitational field acts on the probe particle's state as an operator with eigenvalues $\Phi_1(x_p)$ and $\Phi_2(x_p)$ for the position eigenstates. In fact, we also could have quantized the gravitational potential and included this into a new Hamiltonian $\hat{H}_{\text{with } \Phi} = \hat{H}(1 + \frac{\hat{\Phi}}{c^2})$. For the result of Eq. 5.8 we neglected the fact that \hat{H} and $\hat{\Phi}$ do not commute, as this only gives errors on the order of $\left(\frac{G}{c^2}\right)^2$.

So what we actually have done is quantizing gravity. However, this leads to a whole set of problems as explained in a review by Isham 1993.¹⁴

Of course, we could assume that for all positions of the massive quantum object in superposition we have a completely disjointed spacetime.¹⁵ Assuming the superposition started at $t = 0$, the phase factor of the probe particle's wave function evolves in each spacetime differently. In this section we note that besides the probe particle, all surrounding matter continues in these spacetimes as well, including the measurement

¹³ The total Hamiltonian (without gravity) of two non-interaction states can be written as a sum of two commuting parts $\hat{H} = \hat{H}_M + \hat{H}_p$. In flat space, the total quantum state would simply be $|\Psi\rangle = |\Psi_M\rangle |\Psi_p\rangle = e^{-i\hat{H}t/\hbar} |\Psi_M(0)\rangle |\Psi_p(0)\rangle$, where we omitted the direct-product sign for simplicity.

¹⁴ Isham 1993

¹⁵ A.k.a. a many worlds formalism.

apparatus and the observer. When a measurement is performed, the outcome depends on the spacetime the observer is in. Since all possible outcomes fully exist, it is not clear what the probability distribution $|\Psi(x)|^2$ physically means, other than some Bayesian probability for how much the observer continues to a certain 'world'. Also, this many worlds formalism is a non-falsifiable theory because ultimately we would consider a system consisting of a quantum system together with its measurement apparatus. The two possible outcomes of a measurement would then remain evermore in separate parts of the Hilbert space.

Note that the problems that arises due to the quantization are connected to the problematic straightforward unification of gravity and quantum theory, while the non-falsifiability of the many worlds interpretation touches the measurement problem in quantum mechanics. And so, although Eq. 5.8 is the most straightforward construction of the time evolution of the quantum state from a quantum mechanical and general relativity point of view, the problems above speak against it. However, we know that quantum mechanics works very well on small time scales. So instead of abandoning Eq. 5.8 we continue with this naive solution and try to estimate on what typical timescale things go awry. Oosterkamp and Zaanen 2013¹⁶ followed the same approach, but they focused on the proper time of the massive object itself; the τ_M term in Eq. 5.8. They argued, based on the possible truly classical nature of the gravitational field (spacetime) that the phase difference between the two states of the massive object gives a measure of the collapse time. Doing so they found an expression very similar to Penrose's and Diósi's.

In our case, we do not consider the phases of the states of the massive object explicitly, but rather the states of the surrounding mass, starting with a single probe particle. Applying the same arguments^{16,17} we find that quantum mechanics becomes ill-defined when the phase difference between

¹⁶ Oosterkamp and Zaanen 2013

¹⁷ Rademaker et al. 2014

the probe particle's state in either of the two spacetimes is $\pm\pi$, i.e.

$$\frac{Et}{\hbar c^2} (\Phi_1(\mathbf{x}_p) - \Phi_2(\mathbf{x}_p)) = \pm\pi, \quad (5.9)$$

where E is approximately¹⁸ the energy of the state. To evaluate Eq. 5.9 for our experiment, we must know the energy.¹⁹ Gravity is not so selective on the type of energy, so we use the by far dominant term to the particle's energy which is $E = m_p c^2$, with m_p the probe particle's mass.²⁰ It follows that the time it takes for the state of the collapse equals

$$\tau_p = \frac{\pi\hbar}{m_p |\Phi_1(\mathbf{x}_p) - \Phi_2(\mathbf{x}_p)|}. \quad (5.10)$$

Note that although we derived τ_p as a typical measure of the lifetime of the probe particle, it actually also limits the lifetime of the superposition of the heavy quantum object that generates the two spacetimes.¹⁷ Thus in the case of multiple probe particles, we sum over the probe masses in the appropriate positions. If the superposition starts at $t = 0$, the spacetime can only be in superposition within a radius of $c\tau_p$ as the fabric of space can only change at the speed of light. This leads to a self-consistent equation which, when written as a continuous sum over the environment (probe particles), is given by

$$\tau_p = \frac{\pi\hbar}{\int_{|r| \leq c\tau_p} d^3r \rho_p(\mathbf{r}) |\Phi_1(\mathbf{r}) - \Phi_2(\mathbf{r})|}. \quad (5.11)$$

This typical measure of the gravitational induced decoherence time is calculated for our MRFM-tip where we took the earth as the environment. The obtained values for τ_p , shown in Fig. 5.3, are extraordinarily small compared to the values of Sec. 5.1. For example, for the same size of massive object, we now find a value of 4 μs for a superposition width of the size of the zero point motion. Note that any quantum state has a quantum uncertainty of at least this size. *This brings us to the question if there is not already an experiment done that shows signatures of the collapse time τ_p .* Certainly if the topic of the

¹⁸ Remember that $|\Psi_p\rangle$ is not an eigenstate of the Hamiltonian. However, the difference in energy between various states is small compared to the dominant term and we can neglect these differences.

¹⁹ This is the absolute energy, as explained in Oosterkamp and Zaanen 2013.

²⁰ It can be expected that for normal down-to-earth systems, the mass is the dominant term for the energy eigenstates used, thus making the assumption that $|\Psi_p(0)\rangle$ is an eigenstate of the Hamiltonian redundant.

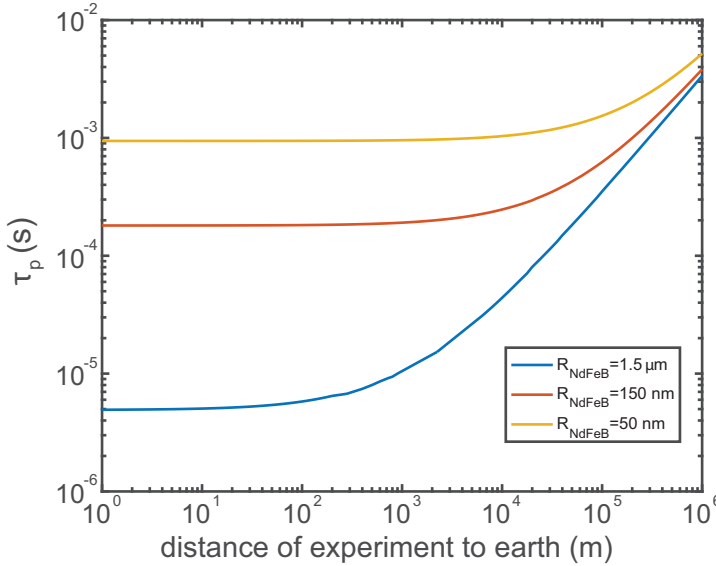


Figure 5.3: The typical measure of instability time τ_p for different distance to earth. The values are found by solving $\tau_p - \frac{\pi\hbar}{\int_{|r| \leq c\tau_p} d^3r \rho_p(r) |\Phi_1(r) - \Phi_2(r)|} = 0$ in MATLAB. The calculation is done for tip diameters of 3 μm , 300 nm, and 100 nm of NdFeB. The width of the superposition was set to the zero point motion of a typical MRFM-cantilever $x_{zpf} \approx 141 \text{ fm}$.

next section is valid and taken into account, it is likely that signatures of the collapse time are already measured. Hence it could also be that Eq. 5.11 is falsified already. However, keep in mind that the generalization of Eq. 5.10 to Eq. 5.11 is based on the assumption that we can simply integrate over the probe particles mass distribution, which might not be valid.²¹

5.3 Mode heating due to spontaneous wave function collapse

ONCE the wave function collapses, naturally the kinetic energy of the system increases.^{3,22,23} Roughly speaking, this is because the collapsed state will on average have a higher energy than the energy expectation value of the original state and it will release this energy as heat into the resonator when the system evolves in time.²⁴ The resonator can lose its heat-energy to the environment only if there is a temperature difference, similar to what is described in Sec. 1.4.

²¹ For example, instead of summing over the probe particle's phases of Eq. 5.9, one might also take the root mean square of these phases. This would lead to a slower collapse time.

²² Diósi 2015

²³ Diósi 2014

²⁴ In principle into the qubit-resonator system, but since the resonator has much higher heat capacity, the energy stored in the spin-part is insignificant. The heat-energy flow from the resonator to the environment through the spin is already included by means of the effective Q-factor.

Diósi 2015 calculated the temperature raise for the Diósi-Penrose model type of spontaneous wave function collapse $\Delta T \sim \frac{\hbar Q}{k_B \omega_0 \tau_p^2}$,²⁵ assuming that $k_B T \gg \hbar \omega_0$. For the largest magnet from Fig. 5.3, and our standard resonator values of $Q \sim 10^4$ and $\frac{\omega_0}{2\pi} = 3$ kHz, we find $\Delta T \sim 10^{-2}$ K which is larger than the offset measured by Vinante et al. 2016⁴, but similar to the saturation temperature in both the Vinante and our experiments.²⁶

The heating effect does not only apply to a resonator in the quantum regime, but provides a lower boundary for the temperature of any resonator, also in the classical regime. In Sec. 4.2 we found a saturation of the mode temperature around 50 mK that we ascribed to vibrations or other noise sources. Usenko et al. 2011 found a saturation at similar temperatures.²⁷

That Vinante et al. 2012 reached lower temperatures by doing active feedback does not contradict the above numbers as the active feedback signal does not tell if the heat input comes from the temperature difference between the heat bath and the environment, from vibrations in the system, or from spontaneous collapse.

The relevant question for our experiment is whether this intrinsic heating might prevent the cooling of the system towards the ground state. If yes, then we are very close to observing the effects of spontaneous wave function collapse. If in the proposed experiment we find that there is no significant intrinsic heating, this would either disprove the assumption on which the heating is based, or ask for modifications or exclusion of some spontaneous collapse models (not only the modified Diósi-Penrose model from Sec. 5.2).⁴

WE CAN CONCLUDE that the masses and oscillation periods of the conventional MRFM-tips fall precisely in the regime where, following the model of Sec. 5.2, the transition occurs from the quantum to the macroscopic world. This chap-

²⁵ This comes from Eq. 16 in Diósi 2015: $\Delta T \sim \frac{\hbar \omega_G^2}{2k_B} \tau$, where $\tau = \frac{Q}{\omega_0}$ is the cantilever time constant and $\omega_G \sim \frac{1}{\tau_p}$, the inverse of the collapse time.

²⁶ Usenko et al. 2011

²⁷ Which they attribute to black body radiation from a 4K thermal shield that heat up the force sensor.

ter will elaborate on the construction of an experiment to test this and other spontaneous collapse models. It must be noted, however, that the theory of Secs. 5.1-5.3 is based on various assumptions and generalizations that are not straightforward. There are many other routes possible in which gravitation might induce an uncertainty into the quantum state.³ What we really need in this field is an experiment.

5.4 Quantum description of spin - resonator system

SO FAR we have checked how the spin-resonator system could be pushed over the boundaries of quantum mechanics. However, we should also know how the experiment would be described in a purely quantum formalism. Firstly because we need quantum mechanics to push the system towards the quantum/classical boundaries, and secondly because we need to have a reference for our results once the experiment passes the boundaries.

THE HAMILTONIAN of the coupled resonator - spin system is given by

$$H = \frac{1}{2m}p^2 + \frac{1}{2}kq^2 + \omega_s \mathbf{B}(q) \cdot \mathbf{S}, \quad (5.12)$$

where p and q are the resonators canonical momentum and position variable respectively, m the mass of the resonator, k the spring constant, ω_s the Larmor frequency, and \mathbf{S} the orientation of the spin.

The magnetic field \mathbf{B} can be expanded to first order in q . Higher orders can be omitted if the spin is positioned such that $\frac{\partial^2 \mathbf{B}}{\partial q^2} \ll \frac{2\mathbf{B}'}{q_{ZPF}}$, where $\mathbf{B}' \equiv \frac{\partial \mathbf{B}}{\partial q}$, $q_{ZPF} \equiv \sqrt{\frac{\hbar}{2m\omega_0}}$ the ground state energy motion (zero point fluctuation in position), and $\omega_0 = \sqrt{\frac{k}{m}}$ the cantilever's natural frequency. The magnetic field can be expanded as $\mathbf{B} \approx B_0 \hat{z} + q\mathbf{B}'$ where we have chosen a Cartesian basis with $\hat{z} = \frac{\mathbf{B}(q=0)}{B_0}$.²⁸ Quantizing the

²⁸ Note that xyz is a local basis for the qubit and is not related to the commonly chosen basis in MRFM-experiments such as in Fig. 3.1 or 4.12.

Hamiltonian leads to

$$\hat{H} = \hbar\omega_0 \left(\hat{a}^\dagger \hat{a} + \frac{1}{2} \right) + \omega_s \hat{S}_z + \left(\hat{a}^\dagger + \hat{a} \right) \left(g_\perp^* \hat{S}_+ + g_\perp \hat{S}_- + g_\parallel \hat{S}_z \right), \quad (5.13)$$

where $\hat{a}^\dagger \equiv \frac{1}{2q_{ZPF}} \left(\hat{q} - \frac{i}{m\omega_0} \hat{p} \right)$ and \hat{a} the creation and annihilation operators respectively. Furthermore, $g_\parallel \equiv -\gamma_s q_{ZPF} B'_z$, and $g_\perp \equiv -\gamma_s q_{ZPF} \left(B'_x + iB'_y \right)$. \hat{S}_x, \hat{S}_y and \hat{S}_z are the spin operators and $\hat{S}_\pm = \hat{S}_x \pm i\hat{S}_y$ the spin raising and lowering operators.

UP TO NOW, the Hamiltonian is general enough for any spin number. For simplicity let us focus on a two level system (2LS).²⁹ Taking the ground state as zero energy, we can write $\hat{S}_z = \hbar\hat{\sigma}^\dagger \hat{\sigma}$, $\hat{S}_+ = \hbar\hat{\sigma}^\dagger$, and $\hat{S}_- = \hbar\hat{\sigma}$, and omit the $\frac{1}{2}$ in the Hamiltonian.

Particularly interesting is the situation where the system is driven with a coherent external radio-frequent magnetic field with frequency ω_d and amplitude B_1 . Because $B_1 \ll B_0$, we can neglect the direct effect on the longitudinal magnetization. For convenience let us choose \mathbf{y} such that $B_{1y} = 0$, and use $\Omega_1 \equiv \gamma_s B_{1x}/2$. Hence, the Hamiltonian becomes

$$\begin{aligned} \hat{H} &= \hat{H}_0 + \hat{H}_{1\perp} + \hat{H}_{1\parallel} + \hat{H}_{drive}, \quad \text{with} \quad (5.14) \\ \hat{H}_0/\hbar &\equiv \omega_0 \hat{a}^\dagger \hat{a} + \omega_s \hat{\sigma}^\dagger \hat{\sigma} \\ \hat{H}_{1\perp}/\hbar &\equiv \left(\hat{a}^\dagger + \hat{a} \right) \left(g_\perp^* \hat{\sigma}^\dagger + g_\perp \hat{\sigma} \right) \\ \hat{H}_{1\parallel}/\hbar &\equiv g_\parallel \left(\hat{a}^\dagger + \hat{a} \right) \hat{\sigma}^\dagger \hat{\sigma} \\ \hat{H}_{drive}/\hbar &\equiv 2\Omega_1 \cos(\omega_d t) \left(\hat{\sigma}^\dagger + \hat{\sigma} \right). \end{aligned}$$

Going to the rotating frame to make the Hamiltonian above time-independent shows that interesting physics comes up depending on frequency ω_d . This is either due to the interaction term $\hat{H}_{1\perp}$ or $\hat{H}_{1\parallel}$, but not for the same values of ω_d . Therefore we review two situations: the first with Hamiltonian $\hat{H}_\perp \equiv \hat{H}_0 + \hat{H}_{1\perp}$ and the second with $\hat{H}_\parallel \equiv \hat{H}_0 + \hat{H}_{1\parallel} + \hat{H}_{drive}$.

²⁹ The two level system, or two state quantum system, might still be part of a bigger (non-degenerate) system.

THE HAMILTONIAN H_{\perp} is particularly interesting for spontaneous interaction between the spin and resonator, thus without the external field turned on:

$$\hat{H}_{\perp} = \omega_0 \hat{a}^{\dagger} \hat{a} + (\omega_s - \omega_d) \hat{\sigma}^{\dagger} \hat{\sigma} + (\hat{a}^{\dagger} + \hat{a}) (g_{\perp}^* \hat{\sigma}^{\dagger} + g_{\perp} \hat{\sigma}). \quad (5.15)$$

Although this is one of the simplest Hamiltonians of interacting quantum systems, achieving an analytical solution for the Schrödinger equation is not easily feasible due to the fact that there is no conserved quantity other than the energy. If one takes the rotating wave approximation, the system would reduce to the Jaynes-Cummings model which has a continuous $U(1)$ symmetry. However, this approximation is only valid if $|\omega_s - \omega_0| \ll |\omega_s + \omega_0|$ and $g \ll \omega_0$. The first is definitely not a valid assumption in our system where ω_s is in the GHz regime, and ω_0 only several kHz. Moreover, it is questionable whether $g \ll \omega_0$ as we will show in the next section that g can be hundreds of Hz.

³⁰ Braak 2011

Braak³⁰ showed that the system can actually be solved. Although a bit different from the Jaynes-Cummings ladder state solution, level crossing of various states can still occur, enabling the transition from higher to lower phonon number states (and vice versa). It can be guessed that the typical transition rate is g_{\parallel} . Making the transition rate asymmetric by pulling the qubit into its ground state would cool (or heat) the resonator. Braak³⁰ showed, however, that level crossings only occur when the external transition rate is a multiple of $\omega_0/2$. This method is different from what is used in optomechanics and not fully explored in the regime where $\omega_0 \ll \omega_s$. *A thorough theoretical analysis is needed to fully explore the possibilities that the system described with this Hamiltonian might reveal.*

THE HAMILTONIAN \hat{H}_{\parallel} can be made time-independent when the wave function $|\Psi\rangle \rightarrow e^{i\omega_d \hat{\sigma}^{\dagger} \hat{\sigma} t} |\Psi\rangle$. Then according to the

Schrödinger equation, the effective Hamiltonian is

$$\hat{H}_{\parallel} = \omega_0 \hat{a}^\dagger \hat{a} + (\omega_s - \omega_d) \hat{\sigma}^\dagger \hat{\sigma} + g_{\parallel} (\hat{a}^\dagger + \hat{a}) \hat{\sigma}^\dagger \hat{\sigma} + \Omega_1 (\hat{\sigma}^\dagger + \hat{\sigma}), \quad (5.16)$$

where we neglected the fast oscillating terms $e^{\pm 2\omega_d t}$. This Hamiltonian is very similar to the Hamiltonian for optomechanics,³¹ with the only difference that the photons from the laser (bosons) are replaced with a spin state (fermion). The main difference here is that $\hat{\sigma}^\dagger \hat{\sigma}$ is finite,³² meaning that when the system is continuously driven, the 2LS oscillates between its states. Compared to optomechanics, we are in a special regime, the single photon regime. The otherwise nonlinear behavior³³ does not happen, because for a 2LS $(\hat{\sigma}^\dagger \hat{\sigma})^2 = \hat{\sigma}^\dagger \hat{\sigma}$. What remains is a resonance frequency shift for the spin by $|g|^2 / \omega_0$. Note that when $\omega_d = \omega_s - \omega_0$ the first two terms of \hat{H}_{\parallel} are degenerate, meaning that the interaction term will let the state oscillate between a quantum state with n phonons and the spin in the ground state, and a state with $n - 1$ phonons and the spin in the excited state.

³¹ Aspelmeyer et al. 2014

³² There are only two values, 0 and 1, for spin- $\frac{1}{2}$.

³³ See Aspelmeyer et al. 2014, Sec. X.F.

MANY PROPOSALS to explore the quantum regime with mechanical devices require cooling of the resonator to(wards) the ground state.^{34,35,36} It is easier to do statistics on quantum measurement outcomes once the probability amplitudes are not convoluted with the thermal spectrum. Moreover, harmonic oscillators with a lower number of phonons exhibit a lower rate of decoherence.³⁷ As explained by Aspelmeyer,³¹ the average phonon number \bar{n} changes according to

$$\frac{d\bar{n}}{dt} = (\bar{n} + 1) (A^+ + A_{th}^+) - \bar{n} (A^- + A_{th}^-), \quad (5.17)$$

where A^\pm are the rates per phonon for upward (higher number of phonons) and downward transitions. The thermal transition rates are given by $A_{th}^+ = n_{th} \frac{\omega_0}{Q}$ and $A_{th}^- = (n_{th} + 1) \frac{\omega_0}{Q}$.³¹ When the interaction term in the Hamiltonian is not relevant, the average number of phonons reaches an equilibrium value $\bar{n} = n_{th} \approx \frac{k_B T}{\hbar \omega_0}$ with T the temperature of the

³⁴ Marquardt et al. 2007

³⁵ Braginsky et al. 1995

³⁶ Marshall et al. 2003

³⁷ Gardiner and Zoller 2004

surrounding heat bath.

The A^\pm transition rates can be calculated using Fermi's golden rule and following Ref. 31

$$A^\pm = 2\pi\hbar g_\parallel^2 S(\omega_d \pm \omega_0) \quad (5.18)$$

where $S(\omega_d \pm \omega_0)$ is the spectral density of the spin.³⁸ The transition rates are clearly different as $\omega_d = \omega_s - \omega_0$, however, the precise imbalance between the transition rates depends on the width of the distribution S .

As a point of concern: *it is questionable if the results obtained from optomechanics are valid in our case. Namely, we are not necessarily in the weak coupling regime. On the other hand the polaron description as used in the strong coupling regime³¹ might need a closer look to check if the same measurement protocols can be applied as in optomechanics.* Note that \hat{H}_\parallel is similar to the Holstein Hamiltonian which can be transformed into \hat{H}_\perp ,³⁹ leaving us with the same questions as before. However, if we can manipulate the qubit in other ways, we can simply hack the transition rates by continuously pushing the qubit into a chosen state using these alternative ways, such that spontaneous transitions can only occur into the required direction. For now let us assume everything works as in optomechanics.

By setting $\frac{d\bar{n}}{dt} = 0$ and assuming $\frac{1}{T_2} \ll \omega_0$, we find the equilibrium phonon number

$$\begin{aligned} \bar{n} &= \frac{A^+ + A_{th}^+}{A^- + A_{th}^- - A^+ - A_{th}^+} \\ &= \frac{n_{th}}{C_0 + 1}, \quad \text{with} \\ C_0 &= \frac{4g_\parallel^2 T_2 Q}{\omega_0}. \end{aligned} \quad (5.19)$$

If the cooperativity C_0 is larger than n_{th} , the system can be cooled to between the ground state and the first excited state. Therefore it is often more useful to work with

$$C \equiv \frac{C_0}{n_{th}} = \frac{4\hbar g_\parallel^2 T_2 Q}{k_B T} \quad (5.20)$$

³⁸ S is the spin's lineshape: a normalized distribution with units of 1/frequency and centered at ω_s , or $\omega_s - g_0^2/\omega_0$ when taking the whole Hamiltonian into account. For spin- $\frac{1}{2}$ the function is normalized. For a spin without interactions, S is a Lorentzian function with a full width at half maximum of $\frac{1}{T_2}$.

³⁹ Tayebi and Zelevinsky 2016

which is an important figure of merit in optomechanical systems and other quantum hybrid systems. If we compare this boson-fermion system with a standard optomechanical setup, the cooperativity cannot be enhanced by adding more photons in the cavity as there are only two spin states. However, if the coupling is strong enough such that $C > 1$, it is easier to bring the mechanical resonator into a cat state as the quantum nature of the single qubit, in contrast to the many photons, is not averaged out.

NOW THAT THE RELEVANT INTERACTIONS are on the table, we can focus on how to construct an experiment that uses these interactions to go beyond quantum mechanics.

5.5 The experiment blueprint

THE PROPOSED EXPERIMENT involves the coupling between a heavy harmonic oscillator and an controllable quantum object. As argued in Ch. 1, the best suited objects with long coherence times are defects in diamonds that consists of nitrogen, an adjacent vacancy and an extra electron. These NV⁻ centers⁴⁰ have a particular energy level scheme that allows for precise control of the three level spin-state. The system can always be driven into the spin ground state by applying a laser pulse, see Fig. 5.4 for a graphical explanation. Depending on the follow-up research on Sec. 5.4, this feature is helpful to make the transition rates asymmetric. Furthermore, the released light is valuable as it gives information about whether the system was in the $m_s = 0$ or $m_s = \pm 1$ state.

The spin state can also be controlled by magnetic resonance. Due to the zero-field splitting that the NV-center features, see Fig. 5.5, an atypical spin-state energy splitting results as the $m_s = 0$ state has a lower energy than the $m_s \pm 1$ states. Luckily the $m_s \pm 1$ states have a different transition energy,

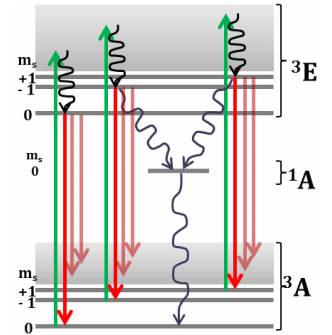


Figure 5.4: Energy level structure of an NV⁻ center. The $m_s = 0$ states from the 3A and 3E states are separated by a 637 nm-photon energy. If the states are excited with green light there is a probability that the system decays back to the same m_s value in the 3A state (eventually via the grey sidebands), however for the $m_s = \pm 1$ states there is a significant probability that it decays to the 1A state which is not m_s preserving. From there it falls back to $m_s = 0$. Applying the green pulse long enough will always bring the system to the $m_s = 0$ state.

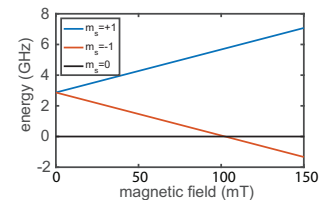


Figure 5.5: Energy of the m_s states in the optical ground state 3A . The three level spin system has a zero field splitting of 2.87 GHz.

⁴⁰ From now on just NV-centers, or NVs.

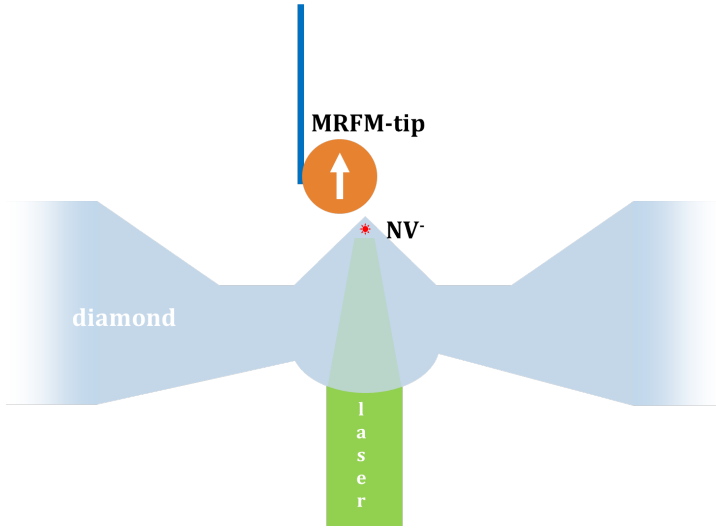


Figure 5.6: Sketch of the proposed experiment. The diamond that contains the NV-center is shaped as a cone or pyramid with 45° angles for maximal light reflection. At the same time there is plenty of space for the MRFM-tip, thereby enabling an intermediate coupling g_\perp or g_\parallel of order ω_0 between MRFM-tip and sample.

so we can address the transitions individually by exciting the $m_s = 0$ state with the right frequency. Because of this, and because we can always initialize the spin in the $m_s = 0$ state, we can treat the NV-center as two superimposed 2LSs.

THERE ARE two practical realizations of how we can couple the NV-center and the resonator: 1) the magnet on the resonator and the NV below, or 2) the NV on the tip and the magnet below. In both cases the magnet or NV-center cannot be positioned beside the resonating cantilever, but only below, otherwise the soft cantilever would snap to contact.

The first realization, the magnet-on-tip method, is the one used in Chs. 3 and 4. The advantage is that the magnet is not only useful for the coupling between resonator and spin, but its motion can also be detected by SQUID-readout.⁴¹ Remember that measuring the motion of the resonator with a laser is not an option as inevitable absorption of the light will raise the temperature of the resonator. For controlling the NV, however, we do need laser light in the experiment. The pulses are typically $1 \mu\text{s}$ or less with $0.1 - 10 \text{ mW}$ laser power. If we apply one pulse per cantilever oscillation, the induced

power into the experiment is in the order of μW . The laser power can be reduced by using on-resonance laser pulses (637 nm), which reduces the needed power by three orders of magnitude.⁴² The drawback of this method is the possible bleaching of the NV^- -center to the useless NV^0 -center.⁴³ The laser power that hits the resonator can also be lowered by using a reflector between the spin and the magnet. A mirror is, however, not an option as a dielectric mirror would be too thick and a metal one will give rise to eddy currents. Luckily due to the high refractive index of diamond⁴⁴ we can construct a corner reflector as shown in Fig. 5.6. There is no need to use reflective coatings or other mirrors providing that the incoming beam is parallel enough. The critical angle for total internal reflection for the diamond-vacuum interface is 24.4° . The incoming angle of the beam shouldn't divert more than 20.6° from the ideal 45° to both interfaces. An advantage of having a parallel beam is that the laser beam's mode is not distorted, which leads to a higher collection efficiency of photons into the fiber and thus less heating.

There are more reasons why a pyramid-shaped diamond feature would be better than a simple flat surface: the coupling between the NV-center and the resonator is very small when the magnet is right above the NV-center, but it is maximal when it is positioned a bit off-center as shown in Fig. 5.6. Due to the pyramid shape the magnet can come closer to the NV-center without touching the surface. A risk of this particular shape is that the cantilever might be pulled towards the pyramid because of electrostatic or Van der Waals forces.

On the other hand, however, due to the reduced amount of diamond bulk and surface in the neighborhood of the MRFM-tip, it interacts less with the unwanted two level fluctuators on the surface which leads to less dissipation, see Chs. 2-4.

For a NdFeB magnet of $3\ \mu\text{m}$ diameter, such as typically

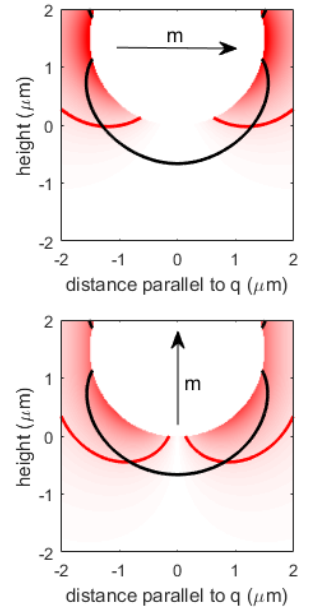


Figure 5.7: Shown are the magnetic field gradients that are relevant for the interaction strength. The magnet is magnetized in q -direction (top figure) and in height direction (bottom figure). In red the gradient component in direction of the magnetic field is shown, and in black the component perpendicular to the magnetic field. Both contour lines are given for $0.2\ \text{T}/\mu\text{m}$. The perpendicular component does not depend on the direction of magnetization (but it does depend on the direction of q). The position of the qubit would ideally be chosen inside the area enclosed by the black and red line, and the magnet. Therefore a magnetization in the height direction seems to be more suitable.

⁴¹ Usenko et al. 2011

⁴² Robledo et al. 2010

⁴³ Manson and Harrison 2005

⁴⁴ The refractive index of diamond is 2.42.

used in Chs. 2-4, we can easily achieve magnetic field gradients of $0.2 \text{ T}/\mu\text{m}$ if the qubit is well positioned as shown in Fig. 5.7. With the ultrasoft silicon cantilevers that have a spring constant of $50 \mu\text{N}/\text{m}$ and an electron spin, the interaction strength g_0 is about 0.8 kHz . Together with a Q of 10^4 and an T_2 of 1 ms , we find a single phonon cooperativity $C \approx 250$.

Due to the softness of the cantilever, the zero point motion is 141 fm which is relatively large compared to other optomechanical experiments.³¹ However, note that the temperature corresponding to the ground state energy is extremely low with a value of only 72 nK .

THE OTHER REALIZATION with the NV on the tip of the resonator has several advantages and challenges. One of the main problems is the readout of the resonator. Since the detection of the motion cannot be done optically due to excessive heating, then practically it should be done with either the static electrical field or magnetic field.⁴⁵ It is advantageous to not have a magnet on the tip of the resonator to make the hybrid quantum system insensitive to stray magnetic fields that are difficult to avoid. It is much easier to shield the system from an electrical field. Detecting the static electrical field, like a SQUID did for the magnetic field, can be done with single electron transistors or similar devices exploiting the Coulomb blockade.⁴⁶ A problem with this method is the relatively high dissipation of these devices compared to SQUIDS.

Another problem would be the need of a laser interacting with the NV-center. The coupling could be done by putting the diamond containing NV particle close to an optical waveguide and let it interact with the evanescent field.⁴⁷ Although it still seems subject to heating, keep in mind that also in the magnet-on-tip situation the magnet is so close to the pyramid that it also can couple to the evanescent field.⁴⁸ *The question*

⁴⁵ Static here means varying slower such that the wavelength is much longer than the typical size of the system.

⁴⁶ Okazaki et al. 2013

⁴⁷ Fu et al. 2008

⁴⁸ Patel et al. 2016

is whether the heating due to optical modes on the magnet's surface in the magnet-on-tip situation isn't worse for heating than the optical electrical field heating up the diamond in the diamond-on-tip situation.

Beside the insensitivity of this method to stray magnetic fields, a big advantage of this realization is that the magnetic field does not have to be generated by a magnetic particle, but can be controlled using thin crossed electrical lines for generating the magnetic field in the wanted strength and direction.⁴⁹

5.6 Roadmap and outlook

THE PROPOSED REALIZATIONS are promising candidates for experiments that might explore the macroscopic boundaries to quantum mechanics when it comes to large mass, large displacement. The protocols to bring the system in a cat state depend on the precise realization. Moreover, the detection methods applied will decide the best way to do the quantum statistics and check whether the system is in the quantum regime, or whether it is collapsed/decohered to a classical state. The collapse/decoherence time as function of the superposition separation, the mass of the cantilever tip, and the distance to earth are the holy grails of these experiments. It is, however, not straightforward to measure such a curve and indirect measurement methods might be needed to obtain the same information. For example, the measurement of spontaneous heating as explained in Sec. 5.3 would provide a simple, although not unambiguous, measurement of the collapse time.

NEVERTHELESS, the first steps on the route to these measurements are straightforward. The exploration and optimization of the control and detection methods while and after building the experiment of Fig. 5.6 or Fig. 5.8 would be the first priority. Before the NVs and the resonator are combined in

⁴⁹ Nichol et al. 2012

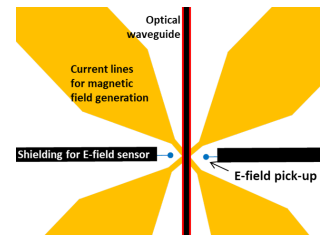


Figure 5.8: Sketch of structures that are needed on the detection chip for a NV-on-tip realization. The optical waveguide for wavelengths of ~ 637 nm are needed to control and probe the NV-center. The generators for the magnetic field can magnetize the NV-center by a DC-current that is flowing through them, and flip the spin if the current is radio frequent. The voltage of the shielded lines would change if the cantilever-tip has a high voltage with respect to the shielding, and the tip oscillates. The position read-out is then performed by sensing the electric field that these lines generate using single electron tunneling devices that consist of quantum dots that are tuned very sensitively to the electrical field.

one setup, one can already optimize the detection method of the tip displacement⁵⁰ and the control of the NV-center. After combining the NV-center part with the mechanical resonator part, the NV can be used as magnetometer to measure the magnetic field profile which can be used to position the NV close to the magnet. Measurements of this type are already done by Kolkowitz et al. 2012. Moreover they could detect the resonator's displacement and thermal spectrum exploiting NV-centers. This demands superb control of the NV-centers without disturbing the resonator. The upside is that this experiment can be started at room temperature which means a much faster iteration process to optimize the experiment.

Naturally, the next step would be to measure a single NV-center doing MRFM improving on the measurements of Ch. 4. Measuring a single electron spin can be done in the footsteps of the methods from Rugar et al. 2004. However, nowadays more advanced protocols are available which accelerates the measurements.^{51,52} Moreover, using the feature that the NV-center can be very precisely controlled, the extensive averaging of measurement data that was necessary in 2004 will be minimal or can even be avoided.

IF EVERYTHING WORKS, we approach rapidly the most interesting regime. At this point it is straightforward to test the methods of active feedback cooling.⁵³ More challenging are the different ways to do sideband cooling, as explained in Sec. 5.4, especially if spontaneous heating spoils the pure quantum interactions. At this point detailed simulations of expected signals are needed to recognize the signatures of the various mechanisms that come into play. Even more so if one tries to generate cat states. However, whatever comes out of these experiments may be interesting for various branches in physics. We can conclude that we are on the doorstep of exciting times; technologically for creating macroscopic

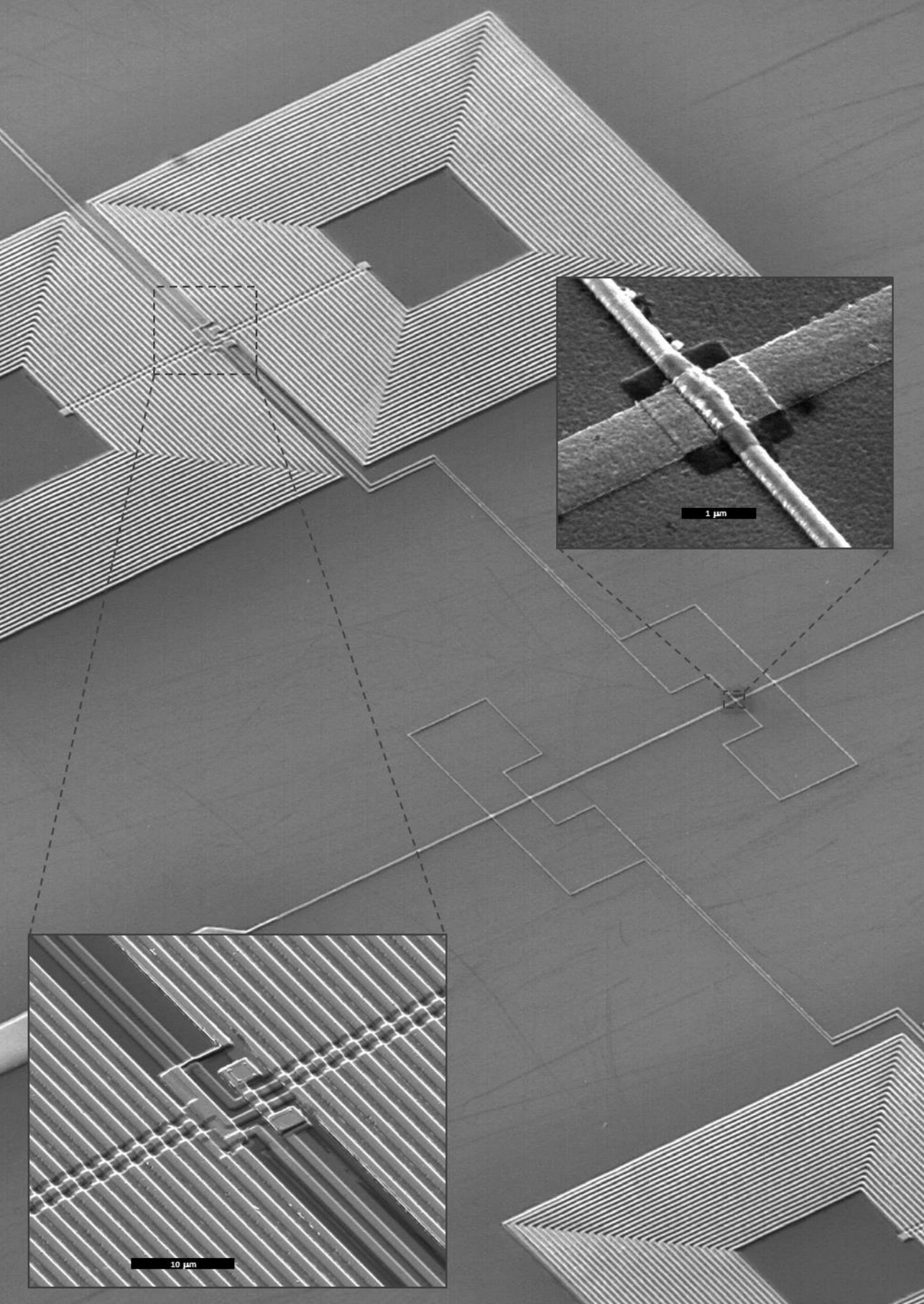
⁵⁰ The SQUID readout for displacement detection is optimized during the work done for this thesis. See also Ch. 6.

⁵¹ Poggio and Degen 2010

⁵² Cardellino et al. 2014

⁵³ Vinante et al. 2012

quantum systems, theoretically for testing the boundaries of quantum mechanics and finding experimental directions for unifications of fundamental theories, and, hopefully, an unequivocal interpretation of quantum mechanics that amends our worldview in a consistent matter.



6 *Techniques and instrumentation*

RESEARCHERS sometimes refer to MRFM as the ‘crosstalk microscope’ when the analysis of obtained signals drive them crazy. The reason for this is on the one hand the supreme sensitivity, and on the other hand the extreme technical criteria and operational conditions for an MRFM apparatus. For example: to show the required sensitivity, consider the thermal force noise amplitude spectral density $\sqrt{S_F} = \sqrt{4k_B T \frac{k}{\omega Q}}$ which is¹ about 1.3 aN/ $\sqrt{\text{Hz}}$. This is even lower when the experiment cools to temperatures of 10 mK and the cantilever reaches Q-factors exceeding 100 000, numbers that are actually reached in our setup, leading to an ultimate force noise of about 0.1 aN/ $\sqrt{\text{Hz}}$. A popular analogy illustrating this tiny number is the gravitational force between a mosquito and a human body at a distance of 365 m.² Note however that, for reasons explained in Ch. 2, the Q-factor can become much lower close to the sample and that the vibrational noise can prevent the mechanical mode from cooling to 10 mK. This exemplifies the extreme conditions at which the MRFM should operate and the as yet seemingly impossible and mutually conflicting criteria the setup should meet.

THIS CHAPTER gives a brief account of some of the things that we conceived, designed, or further developed for the research done in Chs. 3 and 4.³ For these experiments we also used techniques that are reused or copied from previous experiments without improving them significantly, such as

¹ Using typical parameters from our experiments: $T \sim 100$ mK, $k = 50$ $\mu\text{N/m}$, $\frac{\omega}{2\pi} = 2750$ Hz, and $Q = 10000$.

² A consistent analogy should remark that the mass of the mosquito flickers on and off at the resonance frequency.

³ Upon finishing this thesis many of these things are still in use, or used for other research.

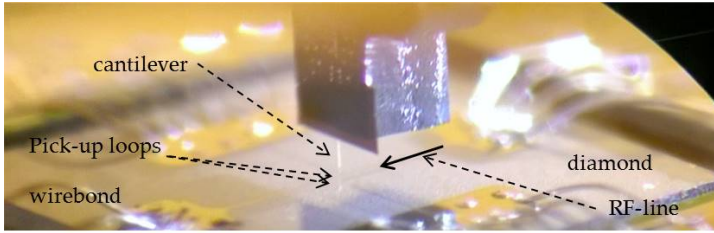


Figure 6.1: In situ image of the diamond sample with wire-bonded RF-line (emphasized with the solid arrow) and two pick-up loops (too small to see). The tiny bright beam beneath the silicon chip is a projection of the cantilever.

vibration isolation. Therefore they are not described in this chapter, but left in the theses of predecessors.^{4,5,6}

In this chapter we will for didactic reasons start describing the system at the heart of the experiment, and from there working our way out.

⁴ Usenko 2012

⁵ Wijts 2013

⁶ Haan 2016

6.1 Sample

IT IS THE DEFECTS IN DIAMOND that we wanted to measure. The defects can be seen as small magnets (spins) that interact with the magnetic tip of the cantilever which is suspended just above the sample. The photo in Fig. 6.1 shows the cantilever positioned above the diamond substrate just before cooling down the experiment. When the spins rotate, the magnetic tip starts to oscillate and vice versa. Another way of rotating the spins is resonantly exciting them with a fast oscillating magnetic field (RF-field). The needed frequency depends on the magnetic field and the type of spin. The ones that we are interested in need to be excited between 0.1 and 5 GHz considering our conditions, see for more information Secs. 4.4 and 4.5. In our experiment, the larger the amplitude of the RF-field, the more accurate the response of the spin. Conventional magnetic resonance experiments use antennas to rotate the spins because antennas can accumulate the incoming RF-power and thus create large magnetic fields. In our experiments this is not an option as antennas are quite narrow banded and cannot easily be tuned to other

frequencies when cooled down to temperatures of 10 mK. For MRFM there are three reasonable options: 1) use an antenna and apply an external magnetic field to tune the frequency of the spins, 2) use an antenna and move the magnetic tip at the end of the cantilever to get the spins into the resonance slice, or 3) don't use an antenna but fabricate a wideband microstripline on top of the sample and only work with spins close to the line.

In our setup it is really difficult to apply an external field because we read out the motion of the cantilever using a SQUID, see Sec. 6.3, which is extremely sensitive to magnetic fields. We have tried this, but until now the SQUID became unstable, or the SQUID's noise-floor was dramatically increased.⁷

⁷ Waarde 2016

The second option is very hard as one relies even more on the reliability of nanopositioning. The actuation at ultralow temperatures and its problems are described in Sec. 6.5. Another drawback is the trade-off between maximal depth of the resonance slice into the sample and the sensitivity⁸ when designing the antenna's resonance frequency.

⁸ Having the resonance slice closer to the tip implies a higher gradient which in turn implies better sensitivity.

This leaves open the third option. For the microstrip line we use superconducting wires as they have minimal dissipation. The thickness and width of the wire is a trade-off between heating⁹ and how close the magnetic tip can approach. Wijts¹⁰ has shown that superconducting wires cause significant repulsion due to the Meissner effect.

⁹ Besides dielectric losses, superconductors still dissipate RF-currents, presumably due to moving of trapped flux quanta.

¹⁰ Wijts 2013

Theoretically, the characteristic impedance of the microstrip, or more general 'waveguide', should be tuned as closely as possible to the characteristic impedance of the RF-power supply lines in the setup which is 50Ω . However, let us assume a reasonable phase velocity of $\sim \frac{1}{2}c$,¹¹ then the wavelength is 50 mm at a frequency of 3 GHz. If the length of the unmatched part of the waveguide stays far below 50 mm, say ~ 5 mm, then the transmitted wave is much larger than the reflected part¹² so we may assume that almost all RF-power arriving at the sample will be transmitted and thus will cre-

¹¹ c is the speed of light.

¹² Pozar 2011

ate an oscillating magnetic field in the sample.

THE MOVEMENT OF THE CANTILEVER needs to be detected as it encodes the information about the interacting spins. Conventional MRFM uses laser interferometry which can heat up the cantilever due to absorption and is limited in sensitivity due to the shot noise of a laser. Therefore we detect the movement of the magnetic tip in a different way: we measure the flux difference that is generated by the tip in a small superconducting pick-up loop. On our small diamond samples the fabrication is already difficult enough to fabricate a good single layer structure, however in the future the design of the pick-up loop could be much improved if we could go to multi-layer fabrication.¹³ The general pattern as shown in Fig. 6.2, can also be used on other samples and is optimized for any of the three possible tip-magnetization directions.

THE ACTUAL DIAMOND SAMPLE is $2.6 \times 2.6 \times 0.3 \text{ mm}^3$ which is an inconveniently small size to handle. Therefore we glued the diamond into the middle of a silicon carrier with either rubber cement¹⁴ or wax.¹⁵ The wax was easier to use as it becomes liquid at $\sim 60^\circ\text{C}$, is very stiff at ambient temperatures, and, the process is reversible. A piece of metal of the same thickness as the sample is glued on all sides to prevent the resist from piling up at the edge of the diamond.

We used the following recipe:

- Spincoat copolymer MMA EL11 (thickness $\sim 610 \text{ nm}$) @4000 RPM, bake 80 s @150 °C.
- Spincoat PMMA A4 (thickness $\sim 190 \text{ nm}$) @4000 RPM, bake 30 min. @120 °C in a vacuum oven.
- Spincoat PSSA¹⁶ @4000 RPM, bake 5 min. 90 °C in vacuum oven.
- Sputter 15 nm of chrome.
- Expose $1050 \mu\text{C}/\text{cm}^2$ ¹⁷ @100 kV.

¹³ We tried this on silicon and the result is promising, but we need more testing. See also Sec. 6.3

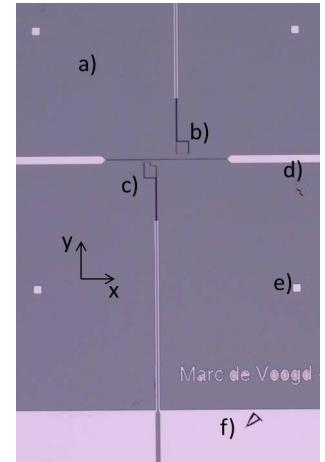


Figure 6.2: Optical microscope photo of diamond sample. This general single layer layout can be used on any sample as the pick-up loops are optimized for any magnetization direction and the added markers make it possible to position another layer or sample. a) Diamond sample, b) simple pick-up loop, c) pick-up loop with extra corner for a tip magnetized in the y -direction, d) RF-line, e) marker, f) bonding pad.

¹⁴ Marubu Fixogum

¹⁵ SPI supplies, crystalbond 509 #5110-AB

¹⁶ Poly(4-styrenesulfonic acid) solution in water. This layer makes a chrome etch unnecessary as PSSA can be removed in water: the chemical chrome etch leaves residues when removing complete layers.

¹⁷ This is the base dose; proximity effect correction (PEC) calculates the best dose for each area of the pattern.

- Sample in water for ~ 1 min, then intensively but gently rinsing.
- (if necessary) When chrome is not completely removed do a quick chemical chrome etch in CE no1.
- Develop 40s in MIBK 1:3 IPA¹⁸.
- Dissolve developer 60 s in IPA and dry gently with N_2 .
- (if necessary) Just before applying NbTiN, do very soft oxygen plasma etch (100 W, 30 s) to enhance sticking.
- Sputter 250 nm NbTiN.
- From this part it becomes difficult to not drop the diamond as it comes off the carrier! Lift-off: 15 min. in acetone, then while (!) rinsing with acetone, move the diamond to a cleaner beaker with acetone and leave it overnight.
- After one night, while rinsing with IPA, move the sample to a beaker with IPA, do ultrasonic cleaning for few minutes, rinse with IPA, then rinse with water and dry with N_2 .

TESTING THE SAMPLE was done in a helium dewar. A newly designed helium dipstick made it possible to quickly cool the sample under the expected superconducting temperature of 15 K. The sample holder is equipped with a heater and a thermometer. Furthermore, each superconducting bonding pad was wirebonded to two electrodes such that a four point measurements could be conducted. The results are given in Fig. 6.3.

6.2 Cantilever

AN ULTRASOFT SILICON CANTILEVER¹⁹ with dimensions 150

¹⁸ MIBK is short for 4-methylpentan-2-on, and IPA stands for iso-propanol but is officially known as propan-2-ol.

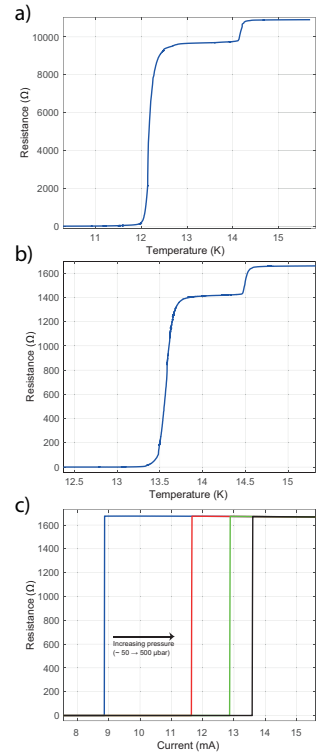


Figure 6.3: The superconducting lines are tested in a vacuum chamber inside a helium dewar. a,b) The resistance as function of temperature for the pick-up loop a) and RF-wire b). The steps can be ascribed to to impurities in small lines of the structure due to the resist present during the NbTiN deposition process. The effect is larger in a) than b) since the pick-up loop has smaller structures than the RF-wire. c) Measurement of the critical current of the RF-wire, determining the maximal B_1 -field strength that can be applied.

¹⁹ Chui et al. 2003

μm long, $4 \mu\text{m}$ wide, 100 nm thick is clamped upon a HV-compatible nanomanipulator that can work inside an electron microscope. On the other side of the manipulator we stuck a carbon tape covered with NdFeB powder which consists of nice spherical balls ranging from $1 \mu\text{m}$ to $100 \mu\text{m}$ in diameter. After aiming for a particle of about $3 \mu\text{m}$ diameter size,²⁰ we glued a particle of $2.99 \mu\text{m}$ onto the cantilever tip.

It is possible to measure the resonance frequency of the new magnetic force sensor inside the electron microscope. The spring constant can be obtained by measuring the resonance frequency before and after attaching the magnet.²¹ The final spring constant and frequency are named k_{sem} and f_{sem} respectively. If due to environmental conditions inside the cryostat the frequency changes to f_0 , the new spring constant k_0 can be calculated by

$$k_0 = \sqrt{\frac{f_0}{f_{sem}}} k_{sem}. \quad (6.1)$$

At cryogenic temperatures and no influence from the sample we obtained $f_0 = 2748.5 \text{ Hz}$ and $k_0 = 48.6 \mu\text{N}$.

6.3 SQUID

TO MEASURE THE FLUX generated by the moving magnet on the MRFM-tip, we use a SQUID. This Josephson junction based device only works at cryogenic temperatures as it uses superconductivity principles.²² The typical flux noise floor is about $1 \mu\Phi_0/\sqrt{\text{Hz}} \approx 2 \cdot 10^{-21} \text{ Wb}/\sqrt{\text{Hz}}$. The other two important parameters are the input inductance L_{in} and mutual inductance M between the input coil and the SQUID loop as shown in Fig. 6.4a. It is suggested²³ that the Johnson noise in the internal currents through the Josephson junctions is so small that it can be ignored, meaning there is no backaction from the SQUID unto the cantilever.

²⁰ Smaller NdFeB magnets tend to lose their remanence field, larger particles have lower field gradients.

²¹ Wijts 2013

²² When we talk about SQUIDS, we mean DC-SQUIDS.

²³ Quantum Design 2001

THE FLUX ϕ_{in} generated by the magnetic tip depends on the movement of the cantilever and the pick-up loop geometry. ϕ_{in} does not depend on the inductances and thus can be seen as constant in this section. The current generated by ϕ_{in} does depend on the total inductance L_{tot} of the loop, thus

$$\frac{\phi_{out}}{\phi_{in}} = \frac{M}{L_{tot}}, \quad (6.2)$$

where ϕ_{out} is the flux that is transferred to the SQUID. As can be seen in Fig. 6.4, $L_{tot} = L_{in} + L_{pul} + L_{par}$, where L_{pul} is the inductance of the pick-up loop and L_{par} the parasitic inductance.²⁴ Taking into account typical values of M and L_{tot} , we only reach percentages of less than 1% of the flux ϕ_{in} that is transferred to the SQUID ϕ_{out} .

This can be improved by using transformers to match the inductances. The incoming versus outgoing flux ratio is given by²³

$$\frac{\phi_{out}}{\phi_{in}} = \frac{MM_{12}}{L_{pr}L_{se} + M_{12}^2} \quad \text{for Fig. 6.4b, and} \quad (6.3)$$

$$\frac{\phi_{out}}{\phi_{in}} = \frac{MM_{12}M_{34}}{(L_{se}L_{te} + M_{34}^2)L_{pr} + L_{te}M_{12}^2} \quad \text{for Fig. 6.4c.} \quad (6.4)$$

It is now easy to calculate an optimal L_1 and L_2 given a certain coupling factor. For superconducting transformers we believe we can achieve inductive coupling factors of ~ 0.9 . This would make the maximal flux input $\sim 50\%$ if we could fabricate the transformers with the optimal values for L_1 and L_2 . However, in practice we were bound by the available transformers whose L_1 is too small and L_2 too large. Hence the flux coupling was 0.5 – 5%, depending on the SQUID type used.²⁵

A second transformer as shown in Fig. 6.4c could easily boost the flux ratio to 10 – 15%, or more if the transformer is made on-chip, considering the absence of parasitic inductances in the first loop. We fabricated an on-chip transformer on silicon as a proof of principle that we can fabricate it at the desired dimensions and without damaging the sample surface, see Fig. 6.5. The double metal-layer fabrication has more advan-

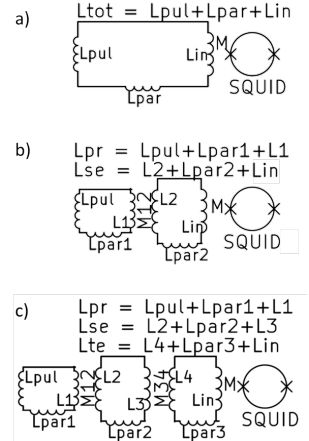


Figure 6.4: Impedance matching becomes inductance matching for circuits without resistances (due to superconductivity) and capacitances (neglectable due to low impedance circuits). L stands for the self inductance of the coils and M for the mutual inductances. The flux comes into the circuit via the small L_{pul} , usually around 10 pH, and needs to be transferred to the SQUID via the relatively large L_{in} , usually > 100 nH and < 10 μ H.

²⁴ For example: L_{par} can come from wirebonds, other wiring, or even superconducting filters.

²⁵ The value of M and L_{in} are determined by the SQUID type.

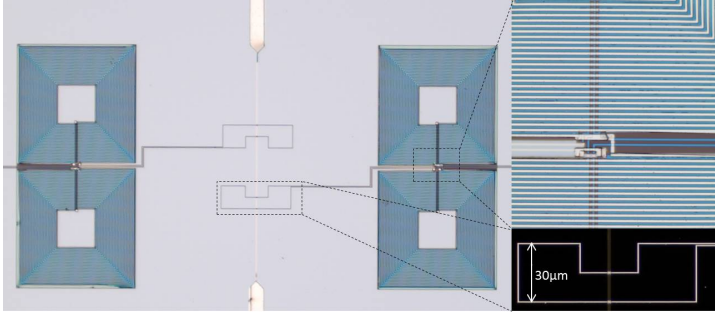


Figure 6.5: NbTiN structures fabricated on silicon. The vertical line is the RF-wire, separated from the overlying U-shaped pick-up loops by $3 \times 3 \mu\text{m}^2$ squares of SiN as can be seen in the right-bottom inset. The signal generated inside the pick-up loop is up converted onto higher impedances by means of a gradiometric transformer. The nontrivial connection in the center of the transformers enables fabrication of the device in only two metal (NbTiN) layers and one insulating spacer (SiN). The lines inside the transformer and the RF-line have a width of $1 \mu\text{m}$ and the pick-up loop has a linewidth of $0.4 \mu\text{m}$

tages such as minimization of the mutual inductance between pick-up loop and RF-line. The improvement of the flux ratio is expected to be about a factor of ten higher compared to the current setup. Testing and implementing of this design is left for successive research projects.

6.4 Anneal-o-tron

THE WIREBONDS to the structures on the sample need to be superconducting. Any resistance will decay the signal and/or heat up the sample. For many experiments we used aluminum wirebonds only, since we would run them solely below 1 K. For some experiments, like testing the RF-line currents, it is advantageous to use materials with a T_c higher than liquid helium temperatures. The problems with Niobium wirebonds are that the material is very stiff due to some impurities, and it has a thick oxide layer. This problem can be made easier by annealing the material for a short time close to its melting temperature. Annealing too long will stiffen the wire again; an anneal time of ~ 5 min. seems to produce the optimal softness.

WE INVENTED A SYSTEM to do this annealing quickly. The system can be mounted directly on top of a pump station. This 'anneal-o-tron' is a simple vacuum pipe with viewports

halfway. The main part of this system is the vacuum insert consisting of three metal rods with two clamps each. The clamps are very fine machined as they can tightly grab a $25\ \mu\text{m}$ diameter wire without breaking it. The anneal-o-tron can be pumped down to 10^{-5} mbar within 15 min. The annealing itself takes about 5 – 6 minutes. For the first wire one might try to find the current at which the wire breaks, for us around 0.2 A. A bit less current, ~ 0.18 A, should produce a good annealing temperature, see Fig. 6.6.

The bonding itself might still be hard because of the niobium oxide layer. Considering the limited amount of wire, we position the wire with a tweezer and stamp it onto the bonding pad with a waffle foot wedge²⁶ using an ultrasonic wirebonder system. The waffle foot makes it possible to apply a lot of force without breaking the wire and hence ultrasonically welding through the oxide layer.



Figure 6.6: *top*: anneal-o-tron, *middle*: clamps holding a $25\ \mu\text{m}$ diameter wire, *bottom*: annealing of niobium wire.

²⁶ 7145W-M-0055-L-M-A, waffle foot wedge from Small Precision Tools

6.5 Nanopositioning

ONE of the hardest parts of an MRFM microscope is the maneuvering of the tip with respect to the sample while the experiment is cooled to temperatures below 1 K. A short design brief for such a positioning system considering only the most important aspects includes:

1. (sub) nanometer positioning with at least 1 mm travel range in all three dimensions,
2. reliable working at ultra low temperatures,
3. maximal dissipation $< 1\ \mu\text{W}$,
4. stiffness of mechanical loop $> 3\ \text{kHz}$,
5. nonmagnetic, heat conducting materials,
6. magnetic-field shielding outerbody,
7. absolute position readout with nanometer precision.

All practical solutions to the individual requirements, except for the last one, are conflicting with at least one other requirement. For example, copper is a nonmagnetic, very well heat conducting material and is a practical solution; meaning it is relatively cheap and easy to machine. However, the material is not stiff and very heavy, thereby decreasing the stiffness of the mechanical loop. From a scientist's viewpoint, a better choice would be beryllium with the outerbody covered with a layer of lead,²⁷ which would, at least partially, satisfy requirements 4 – 6, however machining this is an engineer's death wish. In our last design we have chosen an aluminum body with a thick gold layer to cool the motor body when the aluminum is below its superconducting temperature.²⁸ Some manufacturer parts are used as is and they are mainly made of titanium and stainless steel. This is unfortunate as titanium has a superconducting transition within the measurement temperature range, and stainless steel is a little bit magnetic and has poor heat conducting properties. These compromises had to be taken in view of time constraints. Due to requirements 3 and 6, motors that create large magnetic fields are not suitable. Considering the low temperature, low vibrational environment, we are naturally left with piezoelectric driven motors. Piezos are not free of problems either, however, as their thermal expansion differs from most other materials and their travel range lowers by a factor five when cooled below ~ 80 K. This means that piezowalking motors need extremely fine machining to overcome imperfection with respect to the reduced travel range.²⁹ It is therefore much simpler to use a stick-slip based design, although this probably violates requirement 3. Commonly used piezostacks, that have larger travel ranges than single piezos, have low resonance frequencies and therefore it is best to find a design where these piezos are not part of the mechanical loop.

A WELL ESTABLISHED DESIGN and a trade-off between most requirements is the tripod design as schematically shown in

²⁷ Lead is superconducting below 7.19 K.

²⁸ Pure aluminum has a critical temperature of 1.2 K, but aluminum often used for machining has a critical temperature just below 1 K.

²⁹ The piezowalker is further discussed at the end of this section.

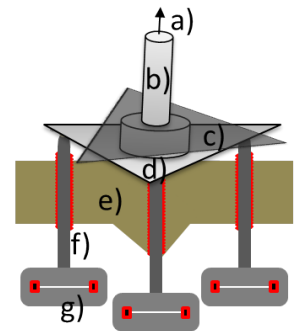


Figure 6.7: Schematic of tripod motor design. a) MRFM probe, b) tower to convert rotation into displacement, c) (dark grey triangle) leaf spring to fix horizontal position of tower base, corners of leaf spring are fixed to motor body, (not shown), d) (light grey triangle) tower base which is moved by spindles, e) motor body, f) spindle, g) piezo knob.

Fig. 6.7. The three parallel mounted linear motors move the triangular base of the tower, thereby wiggling the tower with the cantilever on top in three directions. The linear motors are spindles which are driven by JPE's piezo knobs³⁰ that move using the inertia of the heavy ring around the knob. The piezos that hold the ring can create this inertia. The stick-slip effect takes place between the spindles and nuts, and between the tips of the spindles and the feet of the tower. The knob itself is completely outside the mechanical loop of the cantilever to the sample, see Fig.6.8. The power each motor dissipates is about 1 mW, generated in a brief slip moment in the piezos and also at the contact surface between spindle and nut. To make the cooling faster than in earlier designs, where most of the heat flow goes through the motor body, we connected copper strips between the nuts and the cryostat's mixing chamber plate.

OTHER THINGS we have done to cool the experiment efficiently involves a flame annealed silver strip providing an excellent heat conductance from sample holder and cantilever to the mixing chamber plate. The strip is isolated from other parts of the experiment. A heater is mounted on the strip which can heat the sample and cantilever homogeneously or can be used to keep the temperature constant. The combination of minimal heat capacitance for the sample and cantilever holders and a fast thermometer³¹ mounted on the sample holder makes heating the sample to any specific temperature between 10 mK and 1 K a matter of seconds. Also cooling to any temperature can be done well within a minute, provided that the base temperature of the cryostat is at least about 15 mK below the required temperature.

FOR THE POSITION READOUT with nanometer precision we considered two options. The first option is interferometry. Despite the subnanometer precision, there are two problems with this technique: it can heat up the system and, more im-

³⁰ Cryo Linear Actuator, piezo knobs, from Janssen Precision Engineering

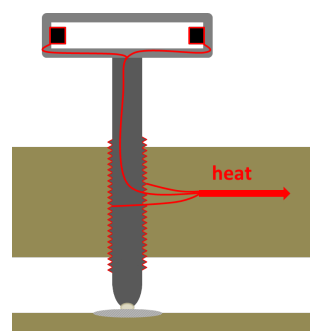


Figure 6.8: Cross section of spindle and piezo knob.

³¹ Custom thermometer from HDL

portantly, it is difficult to measure absolute distances on the micrometer to millimeter scale. We choose to use capacitance readout. The advantages are that the readout itself does not dissipate energy, the position readout is absolute, and it is relatively easy to fabricate the sensors, such that you can make them for every custom application. In fact, for conducting probes one can even use the capacitance between probe and sample as a measure for tip-sample distance. This is further explored in Sec. 7.2, that also explains the details of the principle of capacitance measurements.

We used the capacitance readout to determine the three dimensional position of the probe with respect to the sample. The capacitor was designed as a three-segmented ring to which a variational voltage is applied, see Fig. 6.9. The orientation of the receiver ring, mounted at the bottom of the tower, can be easily measured, and thereby the orientation of the tower and thus the position of the probe. The parallel plate capacitance is

$$C = \frac{\epsilon_0 a}{d}, \quad (6.5)$$

with ϵ_0 the permittivity in vacuum, a approximately the surface of the overlay of the capacitor plates and d the distance between the capacitance plates. As to first order the effective surface of the capacitor plates does not change when the spindles move to length L , and since $L \propto d$, we can write a general linear dependency

$$\begin{pmatrix} L_1 \\ L_2 \\ L_3 \end{pmatrix} = A \begin{pmatrix} 1/C_1 \\ 1/C_2 \\ 1/C_3 \\ 1 \end{pmatrix}, \quad (6.6)$$

where A now is a 3×4 matrix, with the first three columns converting reciprocal capacitance to length and the last column is used to set an arbitrary origin in the L -basis. The conversion from L -basis to a Cartesian basis for the probe's position can now be calculated. The only thing that is needed

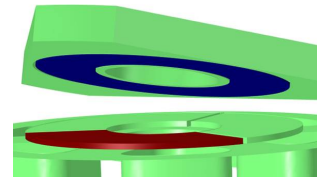


Figure 6.9: Capacitance sensors for 3D-position readout drawn in COMSOL. The three segments at the lower part (one of which is red) are sequentially activated by a 1 kHz voltage. This can be measured with the blue receiver plate due to the mutual capacitance. The capacitance of each of the three segments to the blue plate determines the orientation of the upper part (which is the foot of the tower, not drawn here). The tilt of the upper part is much less in reality.

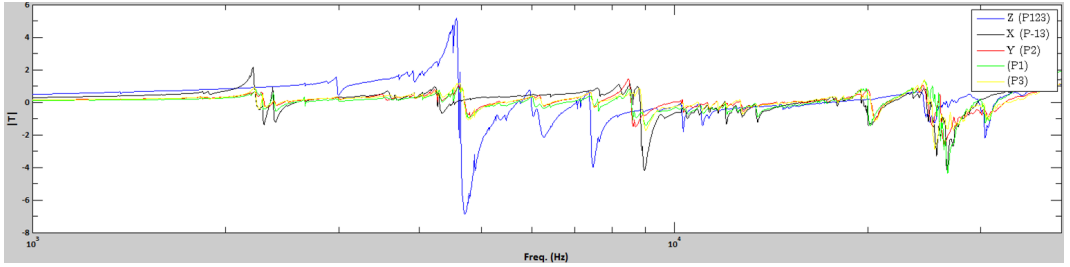


Figure 6.10: Correction to transferfunction of finestage piezo compared to theoretical piezo transferfunction, measured when actuated in Cartesian directions. Here we have chosen z to be a linear combination of all three piezo's (P1+P2+P3), x the difference between two piezo's (P3-P1), and y is proportional to a single piezo (P2).

to be done now is finding A . Each L is the height of a hyperplane above a three dimensional reciprocal capacitance plane. Each row of A can then easily be calculated by fitting the hyperplane through a set of calibration points. For the j^{th} row of A , the coefficients can be calculated by

$$\begin{pmatrix} A_{j1} \\ A_{j2} \\ A_{j3} \\ A_{j4} \end{pmatrix} = \left[\sum_{i=1}^n \begin{pmatrix} \left(\frac{1}{C_{1i}}\right)^2 & \frac{1}{C_{1i}C_{2i}} & \frac{1}{C_{1i}C_{3i}} & \frac{1}{C_{1i}} \\ \frac{1}{C_{1i}C_{2i}} & \left(\frac{1}{C_{2i}}\right)^2 & \frac{1}{C_{2i}C_{3i}} & \frac{1}{C_{2i}} \\ \frac{1}{C_{1i}C_{3i}} & \frac{1}{C_{2i}C_{3i}} & \left(\frac{1}{C_{3i}}\right)^2 & \frac{1}{C_{3i}} \\ \frac{1}{C_{1i}} & \frac{1}{C_{2i}} & \frac{1}{C_{3i}} & 1 \end{pmatrix} \right]^{-1} \left[\sum_{i=1}^n \begin{pmatrix} \frac{1}{C_{1i}L_{ji}} \\ \frac{1}{C_{2i}L_{ji}} \\ \frac{1}{C_{3i}L_{ji}} \\ \frac{1}{L_{ji}} \end{pmatrix} \right], \quad (6.7)$$

where $\left(\frac{1}{C_{1i}}, \frac{1}{C_{2i}}, \frac{1}{C_{3i}}, L_{ji}\right)$ is one of n calibration points. There should be more than 4 independent³² points for each j with a spread much larger than any measurement errors. This method automatically minimizes the summed square errors of the data points with respect to the hyperplane in the L -direction.³³

Once A is known it is straightforward to measure the three capacitances,³⁴ to calculate L , and from there the tip position. In full operational conditions, the absolute resolution was 10 to 100 nanometers for the tip position in the Cartesian basis.³⁵

THE RESONANCES in the mechanical loop are determined by the linear response of small piezo elements that are placed at the end of the spindles. The linear response is derived from an electrical impedance measurement. The result is shown in Fig. 6.10. The largest resonance at 4.5 kHz is certainly higher than the cantilever frequency of about 3 kHz, however small peaks still appear around the cantilever frequency. This is

³²Independent meaning that one point does not scale to another by multiplication by a scalar (plus offset for L).

³³JPE Precision Point 2013

³⁴For which we use an automated capacitance bridge: AH2550 from Andeen-Hagerling.

³⁵Depending on the orientation of the tower. In test situations the resolution was better, however capacitance measurements are very sensitive to ground loops and noise currents, inevitable in large set-ups.

what we also noticed when cooled to milliKelvin temperatures: these small peaks can drive the cantilever if their resonances overlap a bit. We can tune the cantilever's frequency a little bit by positioning it close to the superconducting RF-line, and thereby move the cantilever's frequency to cleaner parts of the spectrum.

TO CONCLUDE THE CURRENT DESIGN, we review requirements 1 – 7. We have satisfied points 1 and 7 well enough for the experiments in Chs. 3, 4, and 7.³⁶ The trade-offs in the design led to only partially meeting requirements 3 – 6 which was fine for now, but might need other solutions in the near future. The most difficult requirement, however, turned out to be 2: When the system is cooled down after thoroughly cleaning the spindles, then the motor usually does work only for the first hundred of microns of movement. Suddenly a spindle can get stuck. This is something we have encountered in many designs and we have not been able to determine the exact problem. Despite changing geometries, materials, piezo knobs and lubricators; the reliability is still a large issue.

MEANWHILE WE HAVE GESTATED many piezowalker designs. The piezowalker consists of a piezo construction that makes a contact with the slider, shifts the slider, then retracts, returns to its starting position, and comes into contact again to set the next step. The design does not depend on fine-tuning of forces to overcome friction forces like in stick-slip mechanisms and is therefore radically different. Also, larger forces might be applied that can solve reliability problems as well as satisfy the other requirements generously. However, this is only possible if the tolerances on the material properties are tight enough and the machining can be done with sub micrometer precision, limited by the range of the piezos. The largest problem is the difference in thermal expansion of materials and the reduction of the piezo's travel range when

³⁶ Especially the absolute position readout (point 7) is an important feature that also led to understanding the tip-sample capacitance in scanning probe microscopes, as published as Voogd et al. 2017a (Ch. 7).

going to low temperatures. In close collaboration with LSI B.V., we developed and tested new designs. We made serious progress as we tested the motors thoroughly in liquid helium to measure the crimp, hysteresis, and reliability. Home made capacitance sensors were used to determine the differences in crimp between various parts with ~ 50 nm precision. This led to a promising new design, which hopefully will provide a solution for low temperature MRFM and bring us a step closer to a commercial MRFM.³⁷

³⁷ Wagenaar 2017

6.6 Cryostat wiring

THE WIRING IN A MULTI-USER CRYOSTAT is subject to multiple constraints: First of all, all wires together have a tight upper bound on the heat conductance they might add between any two different temperature plates. The heat load on the 3 K stage should remain below ~ 1 W; while the heat load onto the mixing chamber should be below ~ 10 μ W. A wire with low heat conductance implies low electrical conductance wires or superconducting wires. The latter is usually only practical between plates that have a temperature lower than 4 K. The second constraint is the interference of signals between experiments. Therefore, using twisted pairs and never using the frame or shielding as return path is mandatory for low frequency signals.³⁸ Preferably every twisted pair should be shielded for electrical fields, while the twisting will minimize the magnetic field interferences. For high frequencies we prefer semirigid cabling as they feature minimal RF-leakage. At low temperatures (10 mK) the maximum frequency of thermal phonons and photons is about 200 MHz, while the RF-signal can be much higher in frequency. So avoiding RF-leakage, which heats the experiment due to electron-phonon coupling, and filtering the low frequency wiring with filters is essential.

³⁸ Low frequency means wavelengths much longer than electrical signal path.

#	conductor	insulator	shielding	use
1	phosphor-bronze	PTFE & graphite	CuNi braid	RT to MC; sensitive signals with $\ll 10$ MHz and $\ll 100 \mu\text{A}$
2a	copper	PTFE	CuNi braid	RT to 4K; coarse signals with $\ll 10$ MHz and ~ 1 mA
2b	NbTi in CuNi	PTFE	CuNi braid	4K to MC; coarse signals with $\ll 10$ MHz and ~ 1 mA
3a	copper	PTFE & graphite	CuNi braid	RT to 1K; SQUID signals with $\ll 10$ MHz and ~ 1 mA
3b	NbTi in CuNi	PTFE & graphite	CuNi braid	1K to MC; SQUID signals with $\ll 10$ MHz and ~ 1 mA
4a	Ag plated CuNi	PTFE	CuNi	RT to 4K; RF signals, 0 – 10 GHz
4b	NbTi	PTFE	NbTi	4K to MC; RF signals, 0 – 10 GHz
5a	Cu	-	-	RT to 50K; very high currents, max 100 A
5b	High Tc	-	-	50K to 4K; very high currents, max 100 A
5c	NbTi in CuNi	-	-	4K to 1K; very high currents, max 100 A

THE WIRING summarized in the table above suits the current purposes of the multi-user cryostat very well. The wires 1 – 3 are used in 24-wire assemblies with multipin connectors on each end. To sum up, we used 6×12 plus 4×1 twisted pairs of type 1, 5×12 twisted pairs of type 2, three 8-wire cables with types 1 and 3 for SQUID-control, 4 semirigids of type 4, and one set of type 5, which leads to a total amount of about 300 shielded conductors going from room temperature (RT) to the mixing chamber (MC).³⁹

AT LOW TEMPERATURES we use a custom made 3×12 pins female connector. Inside the connector each stroke of 3 pins are separately shielded, and one of the three pins is connected to the shielding. This way, the connector itself is a small break-out box to which various cables can be plugged in, see Fig. 6.11.

6.7 From cryostat to electronics

IN A MULTI-USER ENVIRONMENT, colleagues will connect electronics that possibly interferes with another experiments. To minimize this interference while keeping all flexibility we developed break-out boxes with thorough interference protection, see Fig. 6.12. Starting from the cryostat we used a shielded cable with 12 shielded twisted pairs to connect the cabling from the cryostat to the break-out box that is mounted next to the the measurement electronics inside a 19" inch rack. The bundle of twisted pairs inside the cable ends

³⁹ The mixing chamber can reach a temperature below 10 mK.

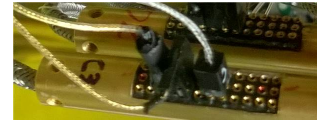


Figure 6.11: 3×12 pins connector for use at low temperatures. The left column of pins is connected to the connector housing to provide a connection for the shielding of the plugged-in cables.



Figure 6.12: Breakout box as manufactured by LSI B.V. a) front panel with 6×4 -pins LEMO connectors. b) Inside of the breakout box. The cabling inside the RF-shielded box have yet to be connected to the EMI feedthrough filters. This box has a frontpanel with 5×4 - and 2×2 -pins LEMO connectors. The single BNC connector, which is connected to the inside shielding of the black cable, can be used to measure noisy voltages between cryostat and 19" rack.

inside an RF-closed box. The wires only come out through pi-sections; a coaxial array of pi-filters⁴⁰ that filter from ~ 5 MHz and have a > 45 dB reduction from 100 MHz to at least 10 GHz. We have noticed that SQUIDs inside the cryostat regularly unlock upon some event outside the cryostat when cables of other nonSQUID equipment were connected to the cryostat *without* this breakout box, while this problem was solved *with* this breakout box. Note that this was the case even though the SQUID cabling was not connected to the breakout box.

Also, connecting commercial scientific instruments to wires that are inductively or even only capacitively coupled to the SQUID created large problems before, while this is now reduced to low frequency interferences only.⁴¹

6.8 Electronic infrastructure

BUT THERE IS MORE that can be done to prevent unnecessary excess noise and interferences. The basic paradigm is: remove all potential noise sources and provide a preferred path for the remaining inevitable noise currents. How this can be done is schematically shown in Fig. 6.13.

⁴⁰EMI Feedthrough Filters
1500pF from Tusonix

⁴¹Such as 50 Hz plus multiples, and switch-mode frequencies that some instruments like to broadcast.

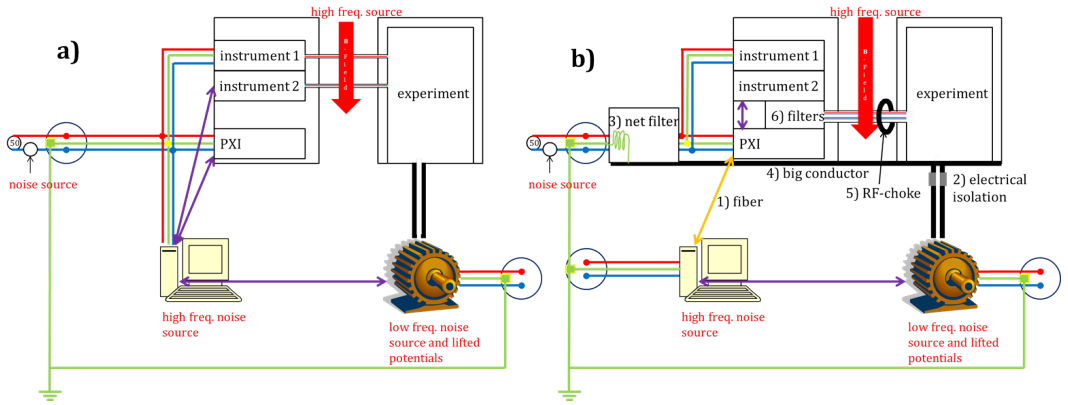


Figure 6.13: Simplified schematic of our set-up a) without and b) with action taken to prevent unnecessary noise. Precaution 1 – 3 decouples the most obvious noise sources while 4,5 makes the remaining noise currents harmless. The break-out box (6) guards the input of the experiment in the cryostat and is discussed in the previous section.

Note that the clean part (the experiment and scientific instruments) is referenced to a potential at a single point. It is highly recommended to use the standard safety earth potential for safety reasons. Note that the precise potential does not matter for noise prevention as long as the frequencies of the reference potential, with respect to the surrounding potentials, are low enough, i.e. the wavelength should be much larger than the system size to avoid resonances due to its self-capacitance or capacitance to surroundings. To avoid such frequencies we placed a lossy coil between the reference point and the system (inside the net filter), thereby compromising $< 10 \mu\text{s}$ peak voltage protection. It is not likely that these short peaks will cause injuries, however, see note 43.

Nowadays even scientific electronics uses digital processors and switch mode power supplies leading to signals at 50 Hz and (mainly odd) multiples, switch-mode signals in the 10 kHz - 5 MHz regime, and digital noise in the very and ultra high frequency regime (30 – 3000 MHz). Of course, for many applications we only need specific frequency bands, so everything else can be filtered. In our case, this is automatically done for all signals passing through the break-out box. Filtering also other parts of the remaining frequency regime⁴² can prevent amplifiers from going into saturation. Moreover,

⁴²Such as AC-coupling that many instruments provide.

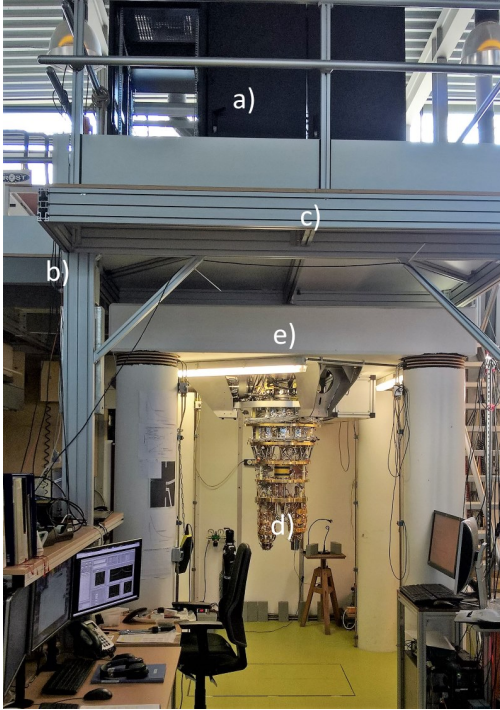


Figure 6.14: Cryostat setup. a) Three 19" instrument racks are connected with glassfibers (b) to the operator's computers. c) The platform is covered with metal plates on top that are welded to each other. The cryostat and 19" racks are connected to this big conductor with thick copper leads and metal supports. d) The experiment(s) hanging below the (open) cryostat. e) A heavy concrete 'temple' on which the cryostat is hanging. The temple stands on a different foundation than the building to avoid acoustic interference.

as a rule of thumb, it is usually best to pre-amplify signals going into or attenuate signals coming out of commercial scientific instruments such that they can make optimal use of their dynamical range at their input *and* output.

To MAKE SURE that every user adapts to this way of working, we needed to construct it in such a way that it takes effort to *not* work this way.⁴³ Therefore we lifted all 19" racks that contain measurement instruments to a higher floor, see Fig. 6.14.

⁴³ Little did we know that scientists can be so desperate that they put effort in directly connecting the experiment to their computers, instead of using optical decoupling, and thereby possibly grilling their USB-controllers.



7 *Fast and reliable pre-approach for scanning probe microscopes based on tip-sample capacitance*

Within the last three decades Scanning Probe Microscopy has been developed to a powerful tool for measuring surfaces and their properties on an atomic scale such that users can be found nowadays not only in academia but also in industry. This development is still pushed further by researchers, who continuously exploit new possibilities of this technique, as well as companies that focus mainly on the usability. However, although imaging has become significantly easier, the time required for a safe approach (without unwanted tip-sample contact) can be very time consuming, especially if the microscope is not equipped or suited for the observation of the tip-sample distance with an additional optical microscope. Here we show that the measurement of the absolute tip-sample capacitance provides an ideal solution for a fast and reliable pre-approach. The absolute tip-sample capacitance shows a generic behavior as a function of the distance, even though we measured it on several completely different setups. Insight into this behavior is gained via an analytical and computational analysis, from which two additional advantages arise: the capacitance measurement can be applied for observing, analyzing, and fine-tuning of the approach motor, as well as for the determination of the (effective) tip radius. The latter provides important information about the sharpness of the measured tip and can be used not only to characterize new (freshly etched) tips but also for the determination of the degradation after a tip-sample contact/crash.

This work is published as: de Voogd *et al.* Fast and reliable pre-approach for scanning probe microscopes based on tip-sample capacitance. *Ultramicroscopy*, Volume 181, October 2017, Pages 61-69, ISSN 0304-3991; doi: 10.1016/j.ultramic.2017.05.009 (2017).

7.1 Introduction

ALTHOUGH Scanning Probe Microscopes (SPMs) have clearly demonstrated their power and are used in many different fields,^{1,2,3,4} their usability is still an issue. For example, when comparing to an electron beam technique that can quickly deliver an image of the surface, the user of an SPM has to bring the tip into close vicinity to the sample (pre-approach), thereby avoiding a resolution destroying tip-sample contact (*tip crash*). This requires a careful approach system, which can last even up to ~ 100 minutes depending on the microscope, especially if the microscope does not provide optical access.

Ideally, one would like to have a fast, robust, and general solution for the approach metrology that can be used in any type of SPM, independently of the design. In this paper we demonstrate a straightforward solution for all SPMs that work with a (semi)conductive tip and sample: the tip-sample distance can accurately be measured via the tip-sample capacitance and this can be used for a quick and robust pre-approach. We also demonstrate that this technique can be applied in tuning-fork based Atomic Force Microscopes (AFMs). Please note that a special class of SPM, the Scanning Capacitance Microscope (SCM), uses the capacitance variation even for imaging and/or spectroscopy.^{5,6,7,8}

For Scanning Tunneling Microscopes (STMs) *with* optical access, the total approach duration is often decreased to acceptable times by using the distance between the tip and its reflection in the sample during a manual pre-approach. In this way the tip-sample distance can be safely decreased to $60 \mu\text{m}$, before the user switches to any type of automatic approach.⁹

However, a fast and reliable manual pre-approach is not always possible, as design aspects of particular SPMs prevent the implementation of optical access (and even cameras). Typical examples are low-temperature STMs, where a closed cryo-

¹ Eigler and Schweizer 1990

² IBM Corp. 2013

³ Vettiger et al. 2000

⁴ Herbschleb et al. 2014

⁵ Kleinknecht et al. 1988

⁶ Lányi and Hruškovíc 2004

⁷ Lee et al. 2006

⁸ Fumagalli et al. 2007

⁹ Usually people work with two different automatic approach routines:

(1) with a fully retracted tip, the tip-sample distance is reduced by one (or several) steps of the coarse approach motor, before a feedback checks whether the tip-sample distance is within tunneling range; if this is not the case, the routine will be repeated,

(2) with a fully working feedback, the tip-sample distance is reduced continuously, until a tunneling current is detected.

Please note that the second method is significantly faster, but often leads to a (not recognized) tip-sample contact when using analog feedback controllers. The reason for this is the integrator in the feedback. This integrator, usually realized as a capacitor, is fully charged to the power supply voltage (here assumed to be positive) during this process. As it integrates the error signal, a reduction of this charge requires a negative voltage of the error signal, which is delivered only if the tip is *closer* to the sample than the *requested* tunneling current set point. This means that, although the tip is already in tunneling conditions, the capacitor is still between zero and full positive voltage, leading to a further approach. Often this electronic circuit is not fast enough to prevent a tip-sample contact.

stat, or at least heat shields, are required.^{10,11,12} A solution for these microscopes is the implementation of absolute position readouts, which is often realized by measuring the capacitance between two cylinders that move with respect to each other. However, the position of the tip with respect to the sample remains still unknown, especially after a sample or tip exchange. As a result the (first) approach with a new tip and/or sample usually takes a long time, as one uses the automatic approach right from the beginning to surely prevent a tip-sample contact.

Finally, there are microscopes which can neither implement an optical access nor a capacitive (or any other) readout system.⁴ For such systems, a pre-approach based on the tip-sample capacitance, as described in this paper, clearly decreases the total approach time with about a factor of ten.

Faced with the problem that the exact surface position is unknown up to mm after a cleaving process of the sample in a cryogenic dipstick setup, Schlegel *et al.*¹³ found an elegant solution for their pre-approach by measuring the second derivative of the tip-sample capacitance during their approach. Their solution circumvents the determination of the absolute capacitance, which is far from trivial, due to its extremely small value.

IN THIS PAPER we set the next step and demonstrate that the tip-sample distance can accurately be measured by determining the *absolute* tip-sample capacitance. This enables not only the application of a quick and robust pre-approach, but delivers in addition a tool for an in situ tip-shape and sharpness characterization as well as for measuring and fine-tuning the performance of the coarse-approach motor. Finally, we also demonstrate that this technique can be applied in tuning-fork based Atomic Force Microscopes (AFMs).

We note here that our results combine partially well-established knowledge of different fields: electronics, nanoscale and tip-sample capacitance research, electronic tip-shape modeling, scanning capacitance microscopy, and scanning tunnel-

¹⁰ Song et al. 2010

¹¹ Jäck et al. 2015

¹² Donati et al. 2016

¹³ Schlegel et al. 2014

ing microscopy. To comprehensively provide the necessary background information, we review the most important aspects thereby giving credits to the different fields.

IN THE FIRST SECTION of the paper we present an overview on how to accurately measure absolute capacitances in the femtofarad (fF) and attofarad (aF) regime. We show that there is no need for special electronics. Moreover, it will become clear that, by default, all STMs are optimized for tip-sample capacitance measurements. This insight can be already deduced from Fumagalli et al. 2006¹⁴ which achieved aF resolution (although not on an absolute scale).

¹⁴ Fumagalli et al. 2006

In the second part, we describe measurements on various STMs and one AFM ranging from homebuilt to commercially available systems. To demonstrate the accuracy of this technique, we use a precise automated capacitance bridge. It is remarkable that the same bridge has been used by Kurokawa and Sakai 1998¹⁵ to study the influence of the tip shape on the tip-sample capacitance already in 1998. However, we also show that less expensive solutions work as well, depending on the specific information one would like to extract (e.g. only the utilization as a pre-approach).

¹⁵ Kurokawa and Sakai 1998

We will show that all measurements have a generic curve, if one plots the capacitance versus the tip-sample distance: it consists of a linear part for large distances and a steep increase for small distances. Similar observations have been obtained before.^{35,36,37,16,17} However, in addition, we show that the *absolute* capacitance values are in the same order of magnitude (hundreds of fF), although measured with different tips and even on completely different microscopes!

¹⁶ Gomila et al. 2008

¹⁷ Gomila et al. 2014

In the last part we elaborate on the generic aspect of the tip-sample capacitance versus distance curve to receive detailed information on the tip geometry. As the tip-sample capacitance determines the resolution in scanning capacitance microscopy, one can find experiments,^{39,37,36,18,35} analytic descriptions^{39,36,19,38,45,44,35} and finite element models^{41,20} in the literature dating back even to 1988⁴⁵. The growing com-

¹⁸ Law and Rieutord 2002

¹⁹ Hudlet et al. 1998

²⁰ Lányi and Hruškovíc 2003

plexity of the analytical description originates from the desire to explain *all* measured curves with a general equation. However, the tip geometry is not known and has to be assumed. Only Kurokawa and Sakai 1998³⁶ measured experimentally their tip shapes with electron microscopy to combine this information further with their model. Building on the earlier work we performed finite element as well as analytical calculations with the practical aim to entangle the parameters of the geometric tip shape from the measured curves. We show that it is possible to determine the tip radius and sharpness in situ in the microscope, which provides an ideal tool for the user to judge the quality of the tip e.g. after an undesired *tip-crash*. The comparison of our finite element analysis results shows good agreement with the ball model⁴⁵ and its later refinement with a dihedral approximation.⁴³ However, it also becomes clear that the most simple model, the ball model of Kleinknecht et al. 1988⁴⁵, fits the data best and is, therefore, in practice the most effective one to use.

7.2 *Subfemtofarad capacitance measurement principles*

USING the tip-sample capacitance for the pre-approach requires the capability to measure capacitances with a resolution smaller than one femtofarad. To demonstrate that the capacitance between the tip and the sample delivers an accurate, absolute measure for the tip-sample distance, we measured even with aF resolution. This has been achieved earlier by Fumagalli et al. 2006,³⁵ however, only on a relative scale. Measuring capacitances within the femtofarad range is not difficult, provided it is performed carefully. There is various commercial electronics available that is suitable for measuring in this capacitance range; usually higher-end electronics allow more accurate and absolute measurements. As most SPMs are not designed for high-frequency applications, we limit ourselves to frequencies below 10 kHz.

It is crucial that the electronic connections leading to the ca-

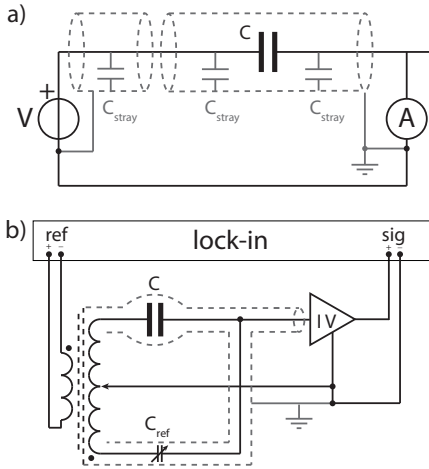


Figure 7.1: Working principles of capacitance measurements: a) Schematic of a capacitor with stray capacitances. The low impedance of the current measurement causes the stray capacitances to be negligible. Ideally, the shielding should be connected to ground at one single point in the setup, preferably shortly after the current measurement. b) The resolution and accuracy can be enhanced by using a reference capacitor and a Lock-In. Matching this reference with the unknown capacitor results in a vanishing current, which describes the principles of a capacitance bridge.

capacitor are separately shielded, as one has to prevent the measurement of so-called *stray capacitances*. For example, two conductors that *see* each other have a stray capacitance which leads to an extra capacitance added to the capacitance of interest. Note that two signal wires close to each other easily have capacitances of hundreds to thousands of femtofarads per *centimeter*.²¹

The above explains why it is usually impossible to determine the tip-sample capacitance with a hand-held multimeter: due to stray capacitances, one measures values larger than a picofarad, although one expects (and we will show) that the tip-sample capacitances are in the femtofarad regime. The additional capacitance comes from the signal that goes via the shieldings of the conductors, see Fig. 7.1a. The proper and ideal solution is to apply an alternating-current (AC) signal to one side of the capacitance, and measure the capacitive current with an amplifier that has a low input impedance on the other side of the circuit. A current-to-voltage (IV) converter is the most suited amplifier for this purpose. Please note that a dedicated IV-preamplifier (PreAmp) is inherently installed in every STM. This naturally makes an STM an ideal tool for measuring the tip-sample capacitance. The low input impedance of the PreAmp ensures that the potential difference between the input of the amplifier and the shielding is

²¹ For example: RG58 coaxial cable has 82 pF/m.

minimal such that parasitic currents are minimized. The advantage of the PreAmp has also been noticed by Fumagalli et al. 2006.³⁵

When the signal from the IV-converter is compared to the reference voltage (V_{ref}) by using quadrature measurements (Lock-In), the out-of-phase component (Y) gives a measure for the capacitance:

$$C = \frac{Y}{2\pi f G V_{ref}}. \quad (7.1)$$

Here, G is the gain of the IV-converter and f the frequency of the reference signal, assuming that the frequency, at which the capacitance measurement is performed, is well below the bandwidth of the IV-converter. This concept for measuring the tip-sample capacitance has been applied by Lee et al. 2002,²² Pingree et al. 2005,²³ and Fumagalli et al. 2006.³⁵

²² Lee et al. 2002

²³ Pingree et al. 2005

The reproducibility of the above described measurement depends on (possible) changes in the setup, like the (dis)appearance of ground loops. The application of a reference capacitor offers not only a solution for this inaccuracy, it even enables the determination of absolute capacitance measurements. The solution involves the incorporation of the reference capacitor into the electronic measurement circuit in such a way that physical replugging of the cables is not necessary, although the reference capacitor can be turned *on* and *off*. An elegant way is applying the inverted reference voltage over the reference capacitor, before it is added to the signal right in front of the PreAmp, see Fig. 7.1b. In this way, the reference capacitance is subtracted from the capacitance to be measured. If the reference capacitance exactly matches the capacitance of interest, the output is zero. Even if the capacitance does not match exactly, it is possible to determine the capacitance of interest from the measured (nonzero) signal by precise knowledge of the reference capacitor. Choosing the reference capacitor of the same order of magnitude as the capacitor of interest, makes the output signal smaller and the end result more accurate.

The previous paragraph describes the basic principles of a low-frequency capacitance bridge with high accuracy. Most of the measurements in this paper were performed with an Andeen Hagerling capacitance bridge (AH2550),²⁴ which automatically switches reference capacitances, until the reference value is close to the capacitance of interest. The calibrated reference capacitors are kept at a constant temperature inside an internal oven. This guarantees that the measured capacitance values are of high accuracy and reproducibility. Kurokawa and Sakai 1998³⁶ used a similar bridge to accurately characterize the capacitance of their tips, of which they measured the shape before with an electron microscope.

However, as dedicated capacitance bridges can be rather expensive, we will also present results measured with different instruments. The General Radio capacitance bridge²⁵ requires time consuming, manual switching of the reference capacitors. However, if one only wants to use this bridge for a pre-approach, it is not necessary to zero the signal for each step of the coarse-approach motor. Instead, the reference capacitance is set to a certain, desired threshold value. If the tip-sample capacitance value passes the reference (i.e. the Y-signal on the Lock-In passes zero or the phase rotates 180°), then one knows that the tip enters the range where the automatic approach procedure should be turned on.

Finally, it is easily possible to determine the capacitance directly with dedicated STM electronics, which should be known by researchers that use STMs in spectroscopy mode. If, e.g. the tip is connected to ground via the PreAmp, one can put an AC signal (e.g. 1 V and 10 kHz) on the sample and determine the current through the tip. After the current is converted to a voltage, a Lock-In can be used to determine the out-of-phase component of the signal, from which the capacitance can be calculated using Eq. 7.1.

However, at all tip-sample distances that are larger than the corresponding tunneling regime, the signal is dominated by the current through the capacitance. Therefore, measuring only the amplitude of the signal is enough to determine the

²⁴ AH2550 Ultra-Precision Capacitance Bridge, Andeen-Hagerling (2014)

²⁵ GenRad 1615-A, General Radio Company (~ 1970)

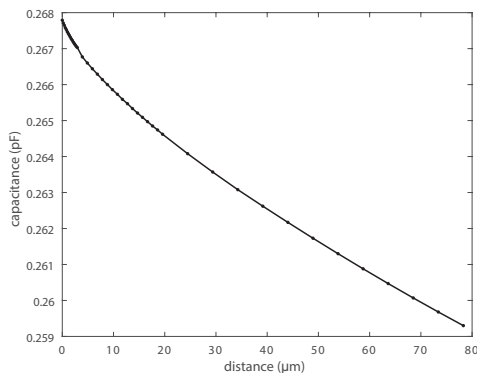


Figure 7.2: Tip-sample capacitance measured on the JPE-STM: This microscope is equipped with a homebuilt, capacitive absolute position sensor. Applying a precise capacitance bridge, an independent determination of the tip height is possible. We used a cut PtIr tip and an HOPG sample. The measurement was performed at room temperature and atmospheric pressure.

capacitance (and no quadrature measurement, like Lock-In, is needed). For example, just by applying the control electronics described by Rost et al.,^{26,27} it is possible to measure ~ 10 aF when applying an AC signal of 1 V and 10 kHz to the sample. This concept is applied by Schlegel et al. 2014,¹³ although they did not work out the absolute capacitances and focused only on the second derivative.

²⁶ Rost et al. 2009

²⁷ Rost et al. 2005

7.3 Results

TO DEMONSTRATE the generality of our approach, we investigate various SPMs. We start with an STM that is equipped with an absolute position readout such that one can directly measure the tip-sample capacitance as a function of the distance. After that, we repeat our measurements on systems without position readout and will show that the tip-sample capacitance provides, in addition, an excellent way of determining the coarse-approach motor dynamics and reliability. Furthermore, we will demonstrate the advantage of a fast and safe pre-approach on an STM with a less reliable approach motor and will show that our method works as well for a noncontact AFM²⁸ that is equipped with a tuning fork. We start with the JPE-STM: a custom Magnetic Resonance Force Microscopy system (MRFM) that consists of a commercially available stage from JPE²⁹ with a home-built absolute

²⁸ Roobol et al. 2015

²⁹ High Resonance Cryo Positioning Stage, Janssen Precision Engineering (2014)

capacitive position readout.³⁰ Applying the AH2550 capacitance bridge, it is possible to measure the absolute position with a precision below 100 nm. Figure 7.2 shows the capacitance between tip (including tip holder) and the sample as a function of the tip-sample distance. The curve in Fig. 7.2 can be used as a calibration of the tip-sample distance by using the capacitance. This calibration holds even after a sample exchange, provided that the new sample has the same geometry. After a tip change, however, the calibration is usually lost. The influence of the tip with respect to the capacitance-distance curve is explained in detail in Sec. 7.4.

AS THE LUXURY of an absolute position readout is not present on most SPMs, a calibration like the one shown in Fig. 7.2 seems to be impossible. This is not fully true, as long as one is not interested in the absolute tip-sample distance in *standard* units. To demonstrate this, we performed a similar measurement on a commercial JT-STM,³¹ of which the result is shown in Fig. 7.3. Obviously, one still recognizes a relation between capacitance and distance. However, the distance here is defined in units of coarse-approach motor steps. Please note that, although the retract curve falls exactly on the approach curve, we applied 420 retract steps, but 497 approach ones. Coarse-motor step sizes are usually not very well defined. Therefore, the step size can only be defined as a statistical average. The step size in slip-stick motors can be directionally dependent due to some constant force pushing the slider towards one or the other direction, like gravitational forces or a spring. To account for such an asymmetry, we rescaled the trace for retracting and approaching in Fig. 7.3 accordingly: it is striking that the curves fall on top of each other quite accurately. This fact together with the smoothness of the curve (and its qualitatively similar shape as in Fig. 7.2) indicates a reliable motor with linear behavior: the step size is constant over the whole range, although it is different between the approach and retract movement. We determined the step size for retracting and approaching via the calibrated piezo

³⁰ More details about this MRFM in Sec. 6.5. The stage is used for measurements in Ch. 4, but for the purpose of the current chapter it is equipped with an STM tip-holder and a Highly Ordered Pyrolytic Graphite (HOPG) sample.

³¹ Joule-Thomson Low-Temperature Scanning Probe Microscope with Tyto head, SPECS (2014)

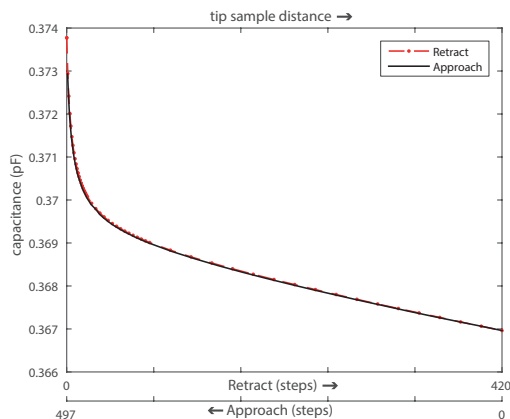


Figure 7.3: Tip-sample capacitance measured on a JT-STM: Without absolute height, the distance is measured in units of coarse approach motor steps. As the retract curve overlaps exactly with the approach curve (after rescaling), this motor runs reliably over the complete travel range, although the average step size is, due to anisotropic forces, different for both directions. We retracted 420 steps, while we needed 497 steps for the approach. Zero corresponds to a tip-sample distance of 10 nm, which we measured with the calibrated scan piezo. Using this piezo, we also calibrated the step sizes of the motor in the tunneling regime: extrapolating this, 420 retract steps correspond to approximately 10 μm . We used a commercially available PtIr tip and a 120 nm thick Au film on Si as a sample. The temperature during the experiment was 4.6 K.

tube, when the system was in tunneling regime. Assuming that these values are representative for the whole measured range, the total distance that the motor traveled was 10 μm .

UNFORTUNATELY the average step size of most coarse-approach motors is not only directionally dependent, but varies, in addition, with the precise position of the motor. This is due to imperfections of sliders and surfaces, wear, heavy use at certain positions of the travel range, and other position-dependent effects, like e.g. springs. This becomes clear from an experiment we performed on a heavily used Unisoko-STM,³² of which the results are shown in Fig. 7.4. To cancel the asymmetry caused by gravity, we applied an analogous directional rescaling as in Fig. 7.3. Here, however, the retract and approach curves do not fall on top of each other. Strikingly, two consecutive experiments (runs) do show reproducibility indicating that the step size does not change significantly in time for a position of the travel range, although there is a huge variation for different positions. As an example, two regions are clearly visible in the approach direction. Our method enables not only the possibility to tune the motor parameters until it moves with constant speed, it even demonstrates the capability to use it for studying coarse-approach motor dynamics in general.

³² USM1300S-3He, Unisoko (2011)

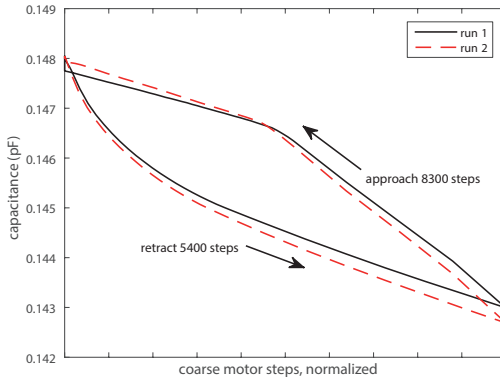


Figure 7.4: Tip-sample capacitance measured on a Unisoko-STM: In both runs, we retracted 5490 motor steps and needed 8300 steps to get back. The starting point corresponds to a tip-sample distance of about 10 nm. Note that this motor runs reliably, as both runs fit almost perfectly on top of each other. However, it is obvious that the motor runs with different speeds on different positions of its travel range. Also directional asymmetry is present. We used a commercially available P4r tip and a Cu(100) sample. These measurements demonstrate that our method can be applied to study the motor performance and dynamics in general. The temperature during the experiment was 1.5 K.

THE MOST REWARDING APPLICATION of the tip-sample capacitance measurement is probably the implementation of it for a fast, safe and reliable pre-approach without optical access. Figure 7.5 shows the results for the ReactorSTM.⁴ The rather unique coarse-approach mechanism in this STM is realized via a sliding movement of the tip (with tip holder) over two guiding rods at the inside of the scanning piezo tube. Between movements, the tip is magnetically pulled to the guiding rods. Due to this special design, this motor shows nonlinear, and sometimes unpredictable behavior, which is also reflected in the curves of Fig. 7.5. The combination of this less reliable motor and the absence of optical access, required often long pre-approach times to safely find the tunneling regime.

After a tip exchange, one first measures one (or several) retract curves, which can also be done at ambient conditions if that is more practical. From these curves one can choose a threshold capacitance that one considers to be safe and fast enough (close enough to the sample) for the quick pre-approach. In a next step, one repeatedly runs the approach motor until the threshold value is reached. This happens within a few seconds. Then one switches to the automatic safe (but slower) approach mode and counts the number of steps that are needed to reach the tunneling regime. This procedure lasts only a few tens of seconds. The crosses in Fig. 7.5 indicate the chosen threshold capacitance versus the number

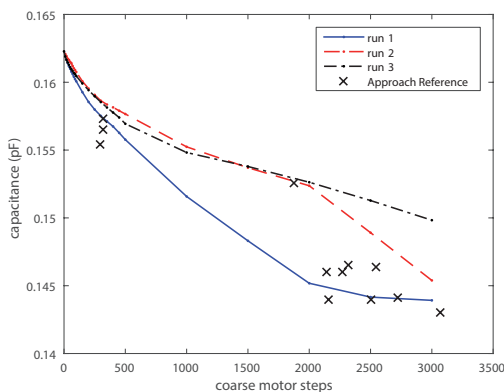


Figure 7.5: Tip-sample capacitance measured on the ReactorSTM: The particular design of the approach motor mechanism makes this motor less reliable compared to the approach motors of other STMs. The variation in the motor performance can be seen from three different retract curves. Still it is possible to significantly shorten the total approach time, as is indicated by the crosses, all of which represent an individual approach: based on earlier measured retract curves (run 1 to 3), the user chooses a *safe* threshold capacitance. The approach motor is continuously operated without extra interrupts until the chosen threshold value is reached. This procedure lasts only a few seconds, after which one switches to the automatic safe (but slower) approach mode and counts the number of steps that are needed to reach the tunneling regime. This procedure lasts only a few tens of seconds. The crosses indicate the chosen threshold capacitance versus the number of steps needed to reach the tunneling regime. To increase the accuracy/statistics, one should measure the capacitance once in a while for a complete retract curve. The data are obtained for different PtIr tips on various (metallic) samples.

of steps needed to reach the tunneling regime. Applying this way of approaching, the system could be regularly brought into tunneling regime within only 10 minutes, while it took usually 60 minutes and more before. Experience shows that this method is insensitive to sample exchange as long as the samples are of comparable geometry. We expect that a complete approach (including the pre-approach) can be realized in less than a minute, if one programs a dedicated routine for the used control electronics and provided that the motor can move fast enough.

IN THE FINAL EXAMPLE, we show that the capacitive approach is more widely applicable than to STM only. To illustrate this, we performed a similar measurement using a non-contact AFM equipped with a quartz tuning fork (QTF).³³ Using Electron Beam Induced Deposition³⁴ (EBID) a nano-sized Pt/C tip was grown on the prong of the tuning fork facing the sample. The length of the tip was $\sim 2.6 \mu\text{m}$ and its diameter was $\sim 220 \text{ nm}$. The tip was first approached to the surface by measuring the shift in resonance frequency after every coarse approach step. After the approach, the QTF was retracted in small steps and the capacitance between tip and sample was measured. The results, plotted in Fig. 7.6, show the same generic curve for the nano-sized tip as observed for the macroscopic STM tips. If one uses a non-conducting tip, one can still use the capacity between the sample and one

³³ similar to the qPlus sensor of Giessibl et al. 2004

³⁴ Nova NanoSEM 200, FEI

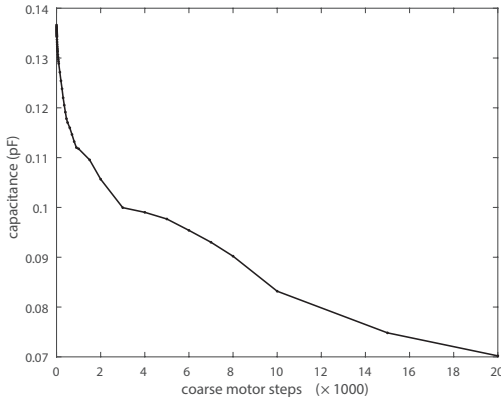


Figure 7.6: Tip-sample capacitance measured on the tuning-fork-based AFM: The tuning fork has an electron beam induced deposited tip on one side. This result shows that our quick pre-approach method, which is based on capacitive measurements, is not only applicable to standard STMs.

electrode of the QTF for the pre-approach.

IN THE ABOVE EXAMPLES we showed *how* the tip-sample capacitance provides valuable information about the tip-sample distance. Even when the capacitance cannot be related to absolute length scales, it still provides information on the motor performance. Depending on the reliability of the motor, the capacitances can be converted into distances in units of motor steps. In any case a reference capacitance can be chosen such that a fast and safe pre-approach can be realized until this value is reached. This method significantly saves time and minimizes the number of tip crash events. In addition, detailed motor characterization and optimization is possible in this way.

7.4 Finite element analysis

THE ABOVE presented tip-sample capacitance measurements all show a rather similar curve with a linear behavior for large distances and a steep rise for decreasingly shorter distances. Similar curves have been obtained before.^{35,36,37,38,39} Moreover, the absolute scale of the values is approximately the same, with the capacitance changing by 5 – 15 fF in the last few tens of micrometers. The AFM is an exception to this because the EBID grown tip is very short and the prong of

³⁵ Fumagalli et al. 2006

³⁶ Kurokawa and Sakai 1998

³⁷ Fumagalli et al. 2007

³⁸ Gomila et al. 2008

³⁹ Gomila et al. 2014

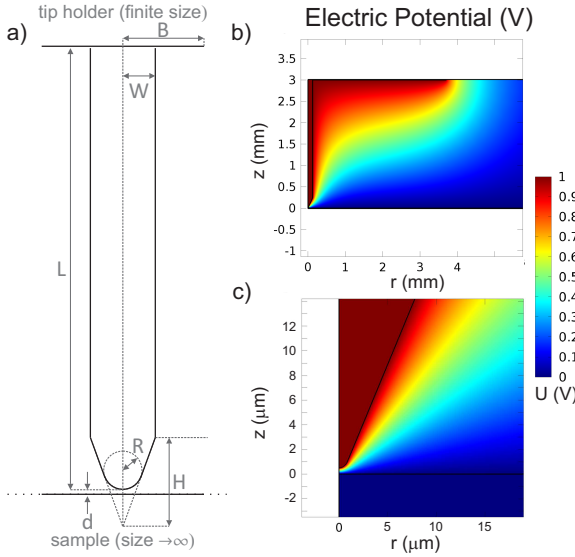


Figure 7.7: Simple tip-model: a) Schematic of the model (drawn not to scale) of a tip with radius W and length L , connected to a base plate with radius B . The end of the tip is conical with height H and truncated with a ball with radius R . The smallest distance between the tip (the apex) and the relatively large sample is noted d . In our finite element simulations the diameter of the tip wire ($2W$) is fixed to 0.25 mm. To calculate the capacitance in the simulation, we did set the tip to a potential of 1 V and the sample to 0 V. Panels b) and c) show the equipotential lines of the simulation for the particular tip geometry at one distance for the JPE-STM: r denotes the radial direction of the geometry and z is the vertical direction. The simulation was performed with COMSOL.⁴⁰

the quartz tuning fork forms a parallel-plate capacitor with the sample surface. Still, the shape of the curve looks similar and suggests a generic behavior which raises the question: can we also *understand* the tip-sample capacitance curve as function of tip-sample distance?

In order to address this question, we performed a Finite Element Analysis (FEA)⁴⁰ calculation and created a simple tip-sample model taking into account cylindrical symmetry, see Fig. 7.7a. Note that other FEA models have been discussed before,^{41,42} however, none of them included the tip holder. By simulating the electrical field, shown in Figs. 7.7b and c, we can determine the capacitance. Finally, by using a parametric sweep for the distance d , which means successive recalculation of the model, we generate a capacitance-distance curve. Furthermore, it is possible to determine the contributions of the tip holder (B), tip length (L), tip sharpness (H), tip wire radius (W), and radius of the apex at the end of the tip (R), as we will describe later in more detail.

To get an estimate for reasonable values of these parameters we can include a lower boundary, which is simply given by a

⁴⁰ COMSOL Multiphysics®v. 5.2. COMSOL AB, Stockholm, Sweden (2015)

⁴¹ Lee et al. 2006

⁴² Lányi and Hruškovíc 2003

parallel-plate capacitor:

$$C_{par} = \frac{\epsilon_0 A_{par}}{L_{par} + d} \quad (7.2)$$

C_{par} causes the linear behavior for large tip-sample distances of the total capacitance, see Fig. 7.8. This additional capacitance comes from the tip holder that forms, in good approximation, with the combination of the sample and sample holder a parallel-plate capacitor. Its capacitance can be easily determined from the data far away from the sample: $A_{par}^{-1} = \epsilon_0 \left. \frac{\partial}{\partial d} C^{-1} \right|_{d_{max}}$ and thus $L_{par} = \epsilon_0 A_{par} / C_{par} - d_{max}$, where d_{max} is the maximum tip-sample distance available in the data. C_{par} is drawn in blue in the graphs of Fig. 7.8 and the corresponding parameters are provided in Tab. 7.1. The remaining deviation for small distances comes from the tip itself and can be described with C_{tip} . Note that L is the real tip length and that L_{par} is the tip length if one assumes the whole capacitance curve could be explained by just one parallel plate at distance $L_{par} + d$. In the following we discuss *how* L as well as the other parameters W, R, H, B influence the capacitance-distance curve. We will show that it is possible to determine all these parameters such that we finally receive fits that closely resemble the measured data, see Fig. 7.8.

SURPRISINGLY, two branches of analytic descriptions for tip-sample capacitances can be found in literature: the first and older ones^{45,36} describe C_{tip} with a sphere, whereas the newer ones consider a cone with a sphere at the end.^{43,44,38} In honor of the first description by Kleinknecht et al. 1988,⁴⁵ we follow

⁴³ Hudlet et al. 1998

⁴⁴ Law and Rieutord 2002

⁴⁵ Kleinknecht et al. 1988

	JPE-stage	JT-Specs STM
W	0.126 mm	0.126 mm
L	3.00 mm	3.00 mm
R	1.0 μm	10 μm
H	0.24 mm	0.30 mm
B	3.7 mm	4.7 mm
πB^2	43 mm ²	69 mm ²
A_{par}	98 mm ²	72 mm ²
L_{par}	3.3 mm	1.8 mm

Table 7.1: This table shows the geometric values that are found by matching the data from Figs. 7.2 and 7.3 to the simple model as illustrated in Fig. 7.7.

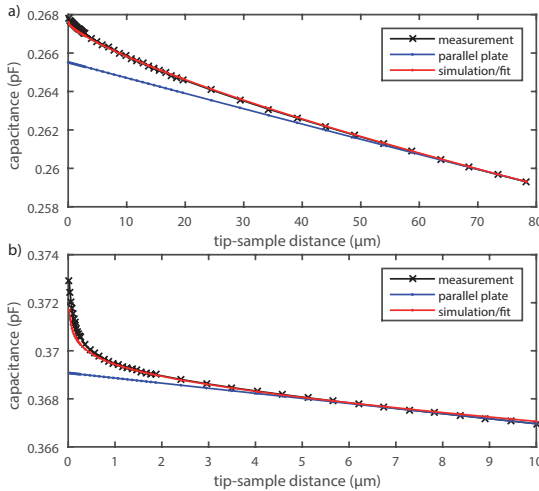


Figure 7.8: Comparison between measured, simulated, and analytically calculated data of the tip-sample capacitance: The measurements are shown in black: (a) for the JPE-STM and (b) for the JT-STM. Our simulations (red) closely fit the experimental values. The curve in blue represents an analytical lower boundary approximation based on a parallel-plate approximation.

this most simplified model to fit and analyze our data. This is fully justified, as we will show in a comparison in Sec. 7.5 that the other, more complicated models, do not deliver better fits or insight.

Describing the very end of the tip with a half sphere, the radius of this sphere, R , determines the distance-capacitance curve for small distances ($d < R$). In turn it is possible to derive the radius of the apex from the measured capacitance-distance curves by using:^{45,36}

$$R_{eff} = \frac{-1}{2\pi\epsilon_0} \frac{dC}{d\ln(d)}, \quad (7.3)$$

For real small distances ($d \ll R$) R_{eff} converges to the real tip radius R , which we can compare with the R in our simulation that fits the measured data. At larger distances C_{par} contributes significantly to the slope of the capacitance-distance curve and therefore R_{eff} is greater than R . This can be seen in Fig. 7.9, in which we applied Eq. 7.3 to capacitance-distance FEA data that we calculated for different tip radii R . One sees that when $d \ll R$, R_{eff} indeed converges to the set value R . For completeness, we also plotted the measured data of the JPE-stage (Fig. 7.2) and the JT-STM (Fig. 7.3) in Fig. 7.9. Although clearly different, both data sets fit the theory. The reason for the difference between these two data sets could

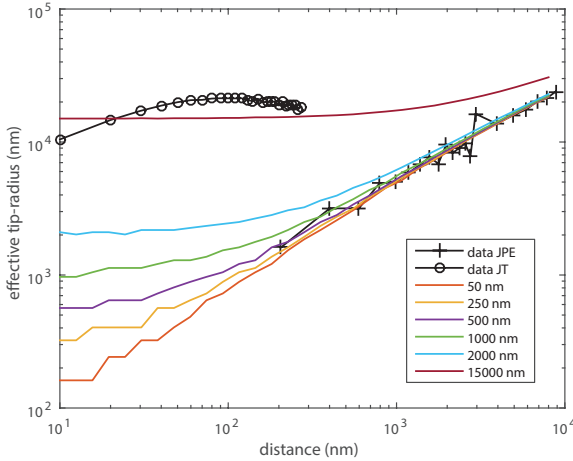


Figure 7.9: Effective tip radius, R_{eff} , versus tip-sample distance. Using our simulations, we varied the tip radius R , see Fig. 7.7, which determines the radius of the apex at the end of the tip. For small tip-sample distances R_{eff} converges to a constant value, which represents the “real” tip radius. This method provides the possibility to determine the end-of-tip radius (e.g. after a tip crash) *in situ*, in the microscope. For comparison we also plotted the JPE-STM as well as the JT-STM data. Note that the tip in the JT-STM had been crashed before, whereas no tip crash happened in the JPE-STM. This can also be seen from the data of the effective tip radii of the two different microscopes.

be tip crashes as well as the different tip fabrication methods (see above).

It becomes clear from this comparison that it is easily possible to determine the apex radius inside the setup, which provides a powerful tool to judge, e.g., if one needs to replace the tip after a tip crash. If one wants to model a measured tip, one should use the lowest measured value for R_{eff} .

Note that it is possible to determine the tip radius (and its sharpness) without the knowledge of the cone height! This finding stands in contrast to previous conclusions.⁴⁶

Taking into account the above insight, we fitted the remaining geometric parameters of the tips of the JPE- and the JT-measurements. Table 7.1 shows the results. From these fits we learned about their dependencies:

In the 1 to 100 micron tip-sample distance regime, L and B contribute in the same manner: they act mainly as an offset to the capacitance curve. As the total tip length can be rather accurately determined and is usually even similar for different microscopes, the main difference often comes from C_{par} , which is due to the specific tip-holder design (described by B). For the fit in Fig. 7.8 we did set L to a fixed, realistic value of 3 mm and varied B as a fitting parameter. The second fitting parameter is given by the cone height H that describes the macroscopic sharpness at the tip end. In the

⁴⁶ Lányi 2005

large-distance regime (1 to 100 micron), this sharpness determines mainly the general slope of the curve, such that this parameter can be determined independently. The last missing parameter is W , which is set by the used tip wire; 126 μm in our case. In conclusion, to receive the fits presented in Fig. 7.8, we determined first the real tip radius R (see Fig. 7.9) and further needed only an optimization of the geometric parameters B and H that determine the offset and slope, respectively, for the large distance range.

As a remark, please note that the values in Tab. 7.1 are not exactly representative for the geometry of the real tips and tip-holders, especially as the geometry of real tip holders can be complicated. However, it is striking that this simple model generates two different curves that follow the capacitance-distance curves of two completely different measured systems remarkably well, see Fig. 7.9.

Despite this fact, a careful comparison between the simulated curve (red) and the measured data (black) in Fig. 7.8 reveals too low capacitances of the fit for small distances. Speculating on the reason, we suspect that the extra capacitance in the experimental data stems from the roughness (imperfections) of the surface of the sphere, like protrusions, that are not included in the model. The additional charge buildup by these protrusions is expected to be commonly found for cut PtIr tips due to the tendency of this material to form micro-tips under cutting. How the capacitance is influenced by the surface roughness can be calculated.^{47,48,49} However, the reverse, how to calculate the roughness of the STM tip based on the additional capacitances in the capacitance-distance curve, remains an interesting open question that is beyond the scope of this paper.

⁴⁷ Boyer et al. 1994

⁴⁸ Bruce et al. 1999

⁴⁹ Bruce et al. 2000

7.5 Analytical models

FOR THE PURPOSE of scanning capacitance microscopy, various analytical formulas have been developed that describe

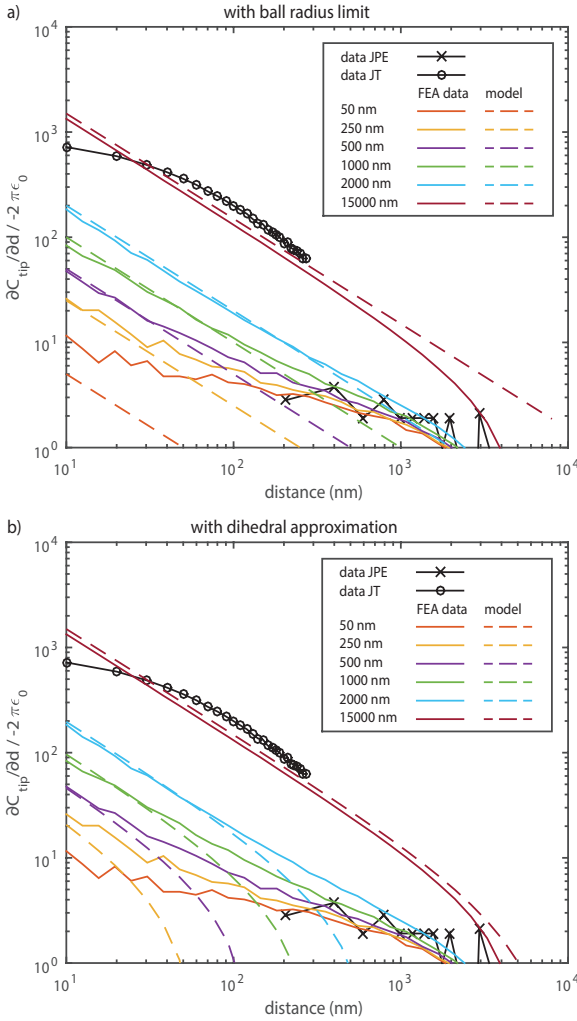


Figure 7.10: Comparison of two analytical models: (a) the ball model described by Eq. 7.4, and (b) the dihedral model described by Eq. 7.5. The dashed lines represent the models, whereas the solid lines show the FEA results. Everything is calculated for different tip radii that are represented by different colors. For completeness we also added the JPE and JT data in black.

the (slope of the) capacitance as a function of tip-sample distance.^{39,36,43,38,45,44,35} One of the earliest contributions^{45,36} state that the variation of the capacitance, $\partial C / \partial d$, comes mainly from the ball-shaped apex (with radius R) in the regime where $d \ll R$. For a ball approaching an infinite plane, this variation is given by:⁴⁵

$$\frac{\partial C_{tip}}{\partial d} \approx -2\pi\epsilon_0 \frac{R}{d} \quad (7.4)$$

Realizing that a real tip does consist of a combination of a ball with a cone, a refined formula was derived a decade later by

using a dihedral approximation.⁴³ The result,

$$\frac{\partial C_{tip}}{\partial d} \approx -2\pi\epsilon_0 \left[\frac{R}{d} \frac{1}{1 + \frac{d}{R(1-\sin\theta)}} + \frac{1}{\ln^2 \tan(\theta/2)} \times \right. \quad (7.5)$$

$$\left. \left(\ln \frac{d + R(1 - \sin\theta)}{H + R(1 - \cot\theta)} - 1 + \frac{1 + \frac{1}{\sin\theta}}{1 + \frac{d}{R(1-\sin\theta)}} \right) \right],$$

is less straightforward since it also involves the cone of the tip that is described by its angle θ , i.e. $\tan\theta = W/H$, see Fig. 7.7. Please note that only the first term in the square brackets comes from the ball-shaped end of the tip. Moreover, following the derivation in Ref. 43 one realizes that Eq. 7.4 was used as a boundary condition for deriving the first term in Eq. 7.5. Since this term dominates at small distances, it is not at all surprising that Eq. 7.5 breaks down to Eq. 7.4 in this regime ($d \ll R$). Noticing that the tip radius influences the total capacitance only for small distances, at which the radius can be determined experimentally, the added value of Eq. 7.5 should be the description of the total capacitance for rather large distances ($d \geq R$). Equipped with the complete FEA tip model, in which we easily can change the tip radii, we tested both analytical descriptions against the FEA model.

Figure 7.10 shows the result, in which the solid colored lines are for different radii obtained from the FEA calculations. Our results nicely match those published by Lányi 2005⁴⁶, who calculated the variation of the tip-sample capacitance for a tip with $R=100$ nm. To evaluate the analytic theories, we fitted (dashed lines) our results with the ball model (Eq. 7.4) in Fig. 7.10a, and with the dihedral approximation model (Eq. 7.5) in Fig. 7.10b. Comparing the fits one realizes three important points: (1) As expected, there is little difference for small distances (compare offset values at the y-axis); (2) The ball model describes straight lines, whereas the dihedral-approximation model curves “down” to lower values at a distance $d \sim \frac{1}{10}R$. (3) In contradiction, the FEA results curve “up” for large distances.

FROM THIS we can conclude that the dihedral-approximation model is not suited to describe the large-distance behavior.⁵⁰ The reason for this is that the cone ends at a certain height (see Fig. 7.7a) and that the tip should be described from this point on with a straight wire that ends in a plate of a capacitor (shield).

This means that fitting the cone angle directly from Eq. 7.5 is unreliable. As the ball radius is equally well derived from Eq. 7.4, there is no advantage to continue using Eq. 7.5. Therefore we used Eq. 7.4 to determine the radius of the ball-shaped apex, see Sec. 7.4. Currently, if one needs to determine the cone angle, one should still create a realistic FEA model.

⁵⁰ It was found by experiments Law and Rieutord 2002 that sometimes the model would better be replaced by a hyperboloid model. However, in our FEA simulations we fixed the geometry to be ball-shaped+cone and not hyperboloid.

7.6 Conclusion

WE SHOWED that it is possible to determine the absolute distance between a tip and a sample via the capacitance between them. Although the capacitances are in the order of tenths to hundreds of femtofarads, the tip-sample separations can be measured reliably for both large scale as well as nanometer distances. Measuring such low capacitances with high accuracy seems to be a difficult task. However, we showed that the application of a low input impedance current-to-voltage converter in combination with proper grounding and shielding makes this task rather easy, as stray capacitances are eliminated in this way. Moreover, by applying an STM control electronics it is possible to measure ~ 10 aF (and even below). We measured the tip-sample capacitance versus distance on several different setups with different tips and samples and found a generic curve with even similar absolute values. Our analysis provides deeper insight and delivers additional benefit for the user, as it is possible to extract the tip shape and radius from these curves. We find, in contrast to earlier conclusions, that it is possible to determine the tip radius without the knowledge of the height of the conical part of the

tip. This is a powerful tool to determine the actual quality of a tip, whether it is freshly etched or has experienced a tip crash. We compared our FEA results with analytic theories and found that the most simple model, the ball model approximation,⁴⁵ delivers the best fit and should, therefore, be used in most cases. Probably the most important impact, however, is the implementation of a fast and reliable pre-approach for any type of SPM and especially for those that do not provide optical access, thereby significantly reducing the total approach time before imaging. Furthermore, it is possible to use the tip-sample capacitance as a characterization tool of the motor performance of the SPM: motor fine tuning, deterioration, and problem analysis can be performed in this way. Finally, the determination of the absolute tip-sample capacitance (including the tip holder) is crucial for a proper system characterization when working in the GHz regime.⁵¹ The capacitance determines, in addition, the energy broadening of an STM when reaching the quantum limit at ultra-low temperatures.⁵²

⁵¹ Jäck et al. 2015

⁵² Ast et al. 2016

Bibliography

- A. Abragam and L. C. Hebel. The Principles of Nuclear Magnetism. *American Journal of Physics*, 29, 860–861, December 1961.
- B. Anderson and J. Payne. *The Spectroscope and Gemmology*. GemStone Press, Woodstock, Vt., 2 edition edition, October 2006.
- M. Aspelmeyer, T. J. Kippenberg, and F. Marquardt. Cavity optomechanics. *Reviews of Modern Physics*, 86, 1391–1452, December 2014.
- C. R. Ast, B. Jäck, J. Senkpiel, M. Eltschka, M. Etzkorn, J. Ankerhold, and K. Kern. Sensing the quantum limit in scanning tunnelling spectroscopy. *Nature Communications*, 7, 13009, October 2016.
- H. Atmanspacher. Quantum Approaches to Consciousness. In E. N. Zalta, editor, *The Stanford Encyclopedia of Philosophy*. Metaphysics Research Lab, Stanford University, summer 2015 edition, 2015.
- N. Bar-Gill, L. M. Pham, A. Jarmola, D. Budker, and R. L. Walsworth. Solid-state electronic spin coherence time approaching one second. *Nature Communications*, 4, 1743, April 2013.
- A. Bassi, K. Lochan, S. Satin, T. P. Singh, and H. Ulbricht. Models of wave-function collapse, underlying theories, and experimental tests. *Reviews of Modern Physics*, 85, 471–527, April 2013.
- G. P. Berman, F. Borgonovi, V. N. Gorshkov, and V. I. Tsifrinovich. *Magnetic Resonance Force Microscopy and a Single-Spin Measurement*. WORLD SCIENTIFIC, September 2006.
- F. Bloch. Nuclear Induction. *Physical Review*, 70, 460–474, October 1946.
- N. Bloembergen, E. M. Purcell, and R. V. Pound. Relaxation Effects in Nuclear Magnetic Resonance Absorption. *Physical Review*, 73, 679–712, April 1948.

- L. Boyer, F. Houze, A. Tonck, J.-L. Loubet, and J.-M. Georges. The influence of surface roughness on the capacitance between a sphere and a plane. *Journal of Physics D: Applied Physics*, 27, 1504, July 1994.
- D. Braak. Integrability of the Rabi Model. *Physical Review Letters*, 107, 100401, August 2011.
- V. B. Braginsky, F. Y. Khalili, and K. S. Thorne. *Quantum Measurement*. Cambridge University Press, Cambridge, 1 edition edition, May 1995.
- P. R. Briddon and R. Jones. Theory of impurities in diamond. *Physica B: Condensed Matter*, 185, 179–189, April 1993.
- N. C. Bruce, A. García-Valenzuela, and D. Kouznetsov. Rough-surface capacitor: approximations of the capacitance with elementary functions. *Journal of Physics D: Applied Physics*, 32, 2692, 1999.
- N. C. Bruce, A. García-Valenzuela, and D. Kouznetsov. The lateral resolution limit for imaging periodic conducting surfaces in capacitive microscopy. *Journal of Physics D: Applied Physics*, 33, 2890, 2000.
- A. Bruno, G. de Lange, S. Asaad, K. L. van der Enden, N. K. Langford, and L. Di-Carlo. Reducing intrinsic loss in superconducting resonators by surface treatment and deep etching of silicon substrates. *Applied Physics Letters*, 106, 182601, May 2015.
- R. Budakian, H. J. Mamin, and D. Rugar. Suppression of spin diffusion near a micron-size ferromagnet. *Phys. Rev. Lett.*, 92, 037205, Jan 2004.
- A. O. Caldeira and A. J. Leggett. Influence of Dissipation on Quantum Tunneling in Macroscopic Systems. *Physical Review Letters*, 46, 211–214, January 1981.
- A. O. Caldeira and A. J. Leggett. Quantum tunnelling in a dissipative system. *Annals of Physics*, 149, 374–456, September 1983.
- J. Cardellino, N. Scozzaro, M. Herman, A. J. Berger, C. Zhang, K. C. Fong, C. Jayaprakash, D. V. Pelekhov, and P. C. Hammel. The effect of spin transport on spin lifetime in nanoscale systems. *Nature Nanotechnology*, 9, 343–347, May 2014.
- S. Carroll. *Spacetime and Geometry: An Introduction to General Relativity*. Pearson, San Francisco, September 2003.
- L. Chen, J. G. Longenecker, E. W. Moore, and J. A. Marohn. Long-lived frequency shifts observed in a magnetic resonance force microscope experiment following microwave irradiation of a nitroxide spin probe. *Appl. Phys. Lett.*, 102, 132404, 2013.

- B. W. Chui, Y. Hishinuma, R. Budakian, H. J. Mamin, T. W. Kenny, and D. Rugar. Mass-loaded cantilevers with suppressed higher-order modes for magnetic resonance force microscopy. *2*, 1120–1123, June 2003.
- P. K. Day, H. G. LeDuc, B. A. Mazin, A. Vayonakis, and J. Zmuidzinas. A broadband superconducting detector suitable for use in large arrays. *Nature*, 425, 817–821, October 2003.
- C. L. Degen, M. Poggio, H. J. Mamin, C. T. Rettner, and D. Rugar. Nanoscale magnetic resonance imaging. *Proc. Natl. Acad. Sci. U. S. A.*, 106, 1313–7, 2009a.
- C. L. Degen, M. Poggio, H. J. Mamin, C. T. Rettner, and D. Rugar. Nanoscale magnetic resonance imaging, appendix b. *Proceedings of the National Academy of Sciences*, 106, 1313–1317, February 2009b.
- L. Diósi. Models for universal reduction of macroscopic quantum fluctuations. *Physical Review A*, 40, 1165–1174, August 1989.
- L. Diósi. Gravity-related spontaneous wave function collapse in bulk matter. *New Journal of Physics*, 16, 105006, 2014.
- L. Diósi. Testing Spontaneous Wave-Function Collapse Models on Classical Mechanical Oscillators. *Physical Review Letters*, 114, 050403, February 2015.
- M. W. Doherty, N. B. Manson, P. Delaney, F. Jelezko, J. Wrachtrup, and L. C. L. Hollenberg. The nitrogen-vacancy colour centre in diamond. *Physics Reports*, 528, 1–45, July 2013.
- F. Donati, S. Rusponi, S. Stepanow, C. Wäckerlin, A. Singha, L. Persichetti, R. Baltic, K. Diller, F. Patthey, E. Fernandes, J. Dreiser, Ž. Šljivančanin, K. Kummer, C. Nistor, P. Gambardella, and H. Brune. Magnetic remanence in single atoms. *Science*, 352, 318–321, April 2016.
- D. M. Eigler and E. K. Schweizer. Positioning single atoms with a scanning tunnelling microscope. *Nature*, 344, 524–526, April 1990.
- A. Einstein. Die Feldgleichungen der Gravitation. *Sitzungsberichte der Königlich Preussischen Akademie der Wissenschaften (Berlin)*, Seite 844-847., 1915.
- Element Six Technologies. *The Element Six CVD Diamond Handbook*. The De Beers Group of Companies, 2015.
- A. Endo, C. Šfiligoj, S. J. C. Yates, J. J. A. Baselmans, D. J. Thoen, S. M. H. Javadzadeh, P. P. van der Werf, A. M. Baryshev, and T. M. Klapwijk. On-chip filter bank spectroscopy at 600-700 GHz using NbTiN superconducting resonators. *Applied Physics Letters*, 103, 032601, July 2013.

- K. M. C. Fu, C. Santori, P. E. Barclay, I. Aharonovich, S. Praver, N. Meyer, A. M. Holm, and R. G. Beausoleil. Coupling of nitrogen-vacancy centers in diamond to a GaP waveguide. *Applied Physics Letters*, 93, 234107, December 2008.
- L. Fumagalli, G. Ferrari, M. Sampietro, I. Casuso, E. Martínez, J. Samitier, and G. Gomila. Nanoscale capacitance imaging with attofarad resolution using ac current sensing atomic force microscopy. *Nanotechnology*, 17, 4581–4587, September 2006.
- L. Fumagalli, G. Ferrari, M. Sampietro, and G. Gomila. Dielectric-constant measurement of thin insulating films at low frequency by nanoscale capacitance microscopy. *Applied Physics Letters*, 91, 243110, December 2007.
- C. Gardiner and P. Zoller. *Quantum Noise: A Handbook of Markovian and Non-Markovian Quantum Stochastic Methods with Applications to Quantum Optics*. Springer, Berlin ; New York, 3rd ed. 2004 edition edition, October 2004.
- S. R. Garner, S. Kuehn, J. M. Dawlaty, N. E. Jenkins, and J. A. Marohn. Force-gradient detected nuclear magnetic resonance. *Applied Physics Letters*, 84, 5091–5093, June 2004.
- F. J. Giessibl, S. Hembacher, M. Herz, C. Schiller, and J. Mannhart. Stability considerations and implementation of cantilevers allowing dynamic force microscopy with optimal resolution: the qplus sensor. *Nanotechnology*, 15, S79, 2004.
- G. Gomila, J. Toset, and L. Fumagalli. Nanoscale capacitance microscopy of thin dielectric films. *Journal of Applied Physics*, 104, 024315, July 2008.
- G. Gomila, G. Gramse, and L. Fumagalli. Finite-size effects and analytical modeling of electrostatic force microscopy applied to dielectric films. *Nanotechnology*, 25, 255702, 2014.
- A. M. J. den Haan. *Nuclear magnetic resonance force microscopy at millikelvin temperatures*. Leiden University, March 2016.
- A. M. J. den Haan, G. H. C. J. Wijts, F. Galli, O. Usenko, G. J. C. van Baarle, D. J. van der Zalm, and T. H. Oosterkamp. Atomic resolution scanning tunneling microscopy in a cryogen free dilution refrigerator at 15 mK. *Rev. Sci. Instrum.*, 85, 035112, 2014.
- A. M. J. den Haan, J. J. T. Wagenaar, J. M. de Voogd, G. Koning, and T. H. Oosterkamp. Spin-mediated dissipation and frequency shifts of a cantilever at millikelvin temperatures. *Physical Review B*, 92, 235441, December 2015.

- P. J. Hajduk, D. A. Horita, and L. E. Lerner. Theoretical Analysis of Relaxation During Shaped Pulses. I. The Effects of Short T_1 and T_2 . *Journal of Magnetic Resonance, Series A*, 103, 40–52, June 1993.
- D. Haneman. Electron paramagnetic resonance from clean single-crystal cleavage surfaces of silicon. *Phys. Rev.*, 170, 705–718, 1968.
- J. G. E. Harris, R. Knobel, K. D. Maranowski, A. C. Gossard, N. Samarth, and D. D. Awschalom. Damping of micromechanical structures by paramagnetic relaxation. *Appl. Phys. Lett.*, 82, 3532–3534, 2003.
- E. C. Heeres, A. J. Katan, M. H. van Es, A. F. Beker, M. Hesselberth, D. J. van der Zalm, and T. H. Oosterkamp. A compact multipurpose nanomanipulator for use inside a scanning electron microscope. *Rev. Sci. Instrum.*, 81, 023704, 2010.
- C. T. Herbschleb, P. C. van der Tuijn, S. B. Roobol, V. Navarro, J. W. Bakker, Q. Liu, D. Stoltz, M. E. Cañas Ventura, G. Verdoes, M. A. van Spronsen, M. Bergman, L. Crama, I. Taminiau, A. Ofitserov, G. J. C. van Baarle, and J. W. M. Frenken. The ReactorSTM: Atomically resolved scanning tunneling microscopy under high-pressure, high-temperature catalytic reaction conditions. *Review of Scientific Instruments*, 85, 083703, August 2014.
- S. Hudlet, M. Saint Jean, C. Guthmann, and J. Berger. Evaluation of the capacitive force between an atomic force microscopy tip and a metallic surface. *The European Physical Journal B - Condensed Matter and Complex Systems*, 2, 5–10, March 1998.
- IBM Corp. A boy and his atom: The world's smallest movie, May 2013. URL <http://ibm.co/ZyRmCT>.
- M. Imboden and P. Mohanty. Evidence of universality in the dynamical response of micromechanical diamond resonators at millikelvin temperatures. *Physical Review B*, 79, 125424, March 2009.
- C. J. Isham. *Canonical Quantum Gravity and the Problem of Time*. NATO ASI Series. Springer, Dordrecht, 1993.
- B. Jäck, M. Eltschka, M. Assig, A. Hardock, M. Etzkorn, C. R. Ast, and K. Kern. A nanoscale gigahertz source realized with Josephson scanning tunneling microscopy. *Applied Physics Letters*, 106, 013109, January 2015.
- JPE Precision Point. Precision Point - Fit a plane through data points, 2013. URL <http://www.janssenprecisionengineering.com/page/fit-a-plane-through-data-points/>.

- G. Jug, S. Bonfanti, and W. Kob. Realistic tunnelling states for the magnetic effects in non-metallic real glasses. *Philosophical Magazine*, 96, 648–703, March 2016.
- V. Kaajakari, T. Mattila, A. Oja, and H. Seppa. Nonlinear limits for single-crystal silicon microresonators. *Journal of Microelectromechanical Systems*, 13, 715–724, October 2004.
- H. P. Kleinknecht, J. R. Sandercock, and H. Meier. An experimental scanning capacitance microscope. *Scanning Microscopy*, 2, 1839–1844, 1988.
- S. Kolkowitz, A. C. Bleszynski Jayich, Q. P. Unterreithmeier, S. D. Bennett, P. Rabl, J. G. E. Harris, and M. D. Lukin. Coherent Sensing of a Mechanical Resonator with a Single-Spin Qubit. *Science*, 335, 1603–1606, March 2012.
- H. Kovacs, D. Moskau, and M. Spraul. Cryogenically cooled probes - a leap in NMR technology. *Progress in Nuclear Magnetic Resonance Spectroscopy*, 46, 131–155, May 2005.
- S. Kuehn, R. F. Loring, and J. A. Marohn. Dielectric fluctuations and the origins of noncontact friction. *Phys. Rev. Lett.*, 96, 156103, 2006.
- S. Kuehn, S. A. Hickman, and J. A. Marohn. Advances in mechanical detection of magnetic resonance. *The Journal of chemical physics*, 128, 052208, February 2008.
- S. Kurokawa and A. Sakai. Gap dependence of the tip-sample capacitance. *Journal of Applied Physics*, 83, 7416–7423, 1998.
- Š. Lányi. Effect of tip shape on capacitance determination accuracy in scanning capacitance microscopy. *Ultramicroscopy*, 103, 221 - 228, 2005.
- Š. Lányi and M. Hruškovic. Analysis of lateral resolution and contrast of scanning capacitance microscopes. *Surface Science*, 566-568, Part 2, 880 - 884, 2004. Proceedings of the 22nd European Conference on Surface Science.
- S. Lányi and M. Hruškovic. The resolution limit of scanning capacitance microscopes. *Journal of Physics D: Applied Physics*, 36, 598, 2003.
- A. Laraoui, J. S. Hodges, and C. A. Meriles. Nitrogen-Vacancy-Assisted Magnetometry of Paramagnetic Centers in an Individual Diamond Nanocrystal. *Nano Letters*, 12, 3477–3482, July 2012.
- B. M. Law and F. Rieutord. Electrostatic forces in atomic force microscopy. *Physical Review B*, 66, 035402, June 2002.

- D. Lee, K. W. Lee, J. V. Cady, P. Ovarthaiyapong, and A. C. Bleszynski Jayich. Topical review: spins and mechanics in diamond. *Journal of Optics*, 19, 033001, 2017.
- D. T. Lee, J. P. Pelz, and B. Bhushan. Instrumentation for direct, low frequency scanning capacitance microscopy, and analysis of position dependent stray capacitance. *Review of Scientific Instruments*, 73, 3525–3533, September 2002.
- D. T. Lee, J. P. Pelz, and B. Bhushan. Scanning capacitance microscopy for thin film measurements. *Nanotechnology*, 17, 1484, 2006.
- S. Lee, E. W. Moore, and J. A. Marohn. Unified picture of cantilever frequency shift measurements of magnetic resonance. *Physical Review B*, 85, 165447, April 2012.
- B. P. Lemke and D. Haneman. Low-temperature epr measurements on *in situ* vacuum-cleaved silicon. *Phys. Rev. Lett.*, 35, 1379–1382, Nov 1975.
- J. H. N. Loubser and J. A. van Wyk. Electron spin resonance in the study of diamond. *Reports on Progress in Physics*, 41, 1201, 1978.
- H. J. Mamin, R. Budakian, B. W. Chui, and D. Rugar. Detection and manipulation of statistical polarization in small spin ensembles. *Phys. Rev. Lett.*, 91, 207604, 2003.
- N. B. Manson and J. P. Harrison. Photo-ionization of the nitrogen-vacancy center in diamond. *Diamond and Related Materials*, 14, 1705–1710, October 2005.
- F. Marquardt, J. P. Chen, A. A. Clerk, and S. M. Girvin. Quantum Theory of Cavity-Assisted Sideband Cooling of Mechanical Motion. *Physical Review Letters*, 99, 093902, August 2007.
- W. Marshall, C. Simon, R. Penrose, and D. Bouwmeester. Towards Quantum Superpositions of a Mirror. *Physical Review Letters*, 91, 130401, September 2003.
- P. Mohanty, D. A. Harrington, K. L. Ekinci, Y. T. Yang, M. J. Murphy, and M. L. Roukes. Intrinsic dissipation in high-frequency micromechanical resonators. *Physical Review B*, 66, 085416, August 2002.
- B. A. Myers, A. Das, M. C. Dartailh, K. Ohno, D. D. Awschalom, and A. C. Bleszynski Jayich. Probing Surface Noise with Depth-Calibrated Spins in Diamond. *Physical Review Letters*, 113, 027602, July 2014.
- Y. V. Nazarov and Y. M. Blanter. *Quantum Transport: Introduction to Nanoscience*. Cambridge University Press, Cambridge, 2009.

- J. M. Nichol, E. R. Hemesath, L. J. Lauhon, and R. Budakian. Nanomechanical detection of nuclear magnetic resonance using a silicon nanowire oscillator. *Physical Review B*, 85, 054414, February 2012.
- D. G. Norris, H. Lüdemann, and D. Leibfritz. An analysis of the effects of short T_2 values on the hyperbolic-secant pulse. *Journal of Magnetic Resonance (1969)*, 92, 94–101, March 1991.
- Y. Okazaki, I. Mahboob, K. Onomitsu, S. Sasaki, and H. Yamaguchi. Quantum point contact displacement transducer for a mechanical resonator at sub-Kelvin temperatures. *Applied Physics Letters*, 103, 192105, November 2013.
- T. H. Oosterkamp and J. Zaanen. A clock containing a massive object in a superposition of states; what makes Penrosian wavefunction collapse tick? *arXiv:1401.0176 [quant-ph]*, December 2013. arXiv: 1401.0176.
- D. P. Pappas, M. R. Vissers, D. S. Wisbey, J. S. Kline, and J. Gao. Two Level System Loss in Superconducting Microwave Resonators. *IEEE Transactions on Applied Superconductivity*, 21, 871–874, June 2011.
- R. N. Patel, T. Schröder, N. Wan, L. Li, S. L. Mouradian, E. H. Chen, and D. R. Englund. Efficient photon coupling from a diamond nitrogen vacancy center by integration with silica fiber. *Light: Science & Applications*, 5, e16032, February 2016.
- P. K. Peddibhotla. *Magnetic resonance force microscopy : harnessing nuclear spin fluctuations*. University of Basel, 2013.
- R. Penrose. On Gravity's role in Quantum State Reduction. *General Relativity and Gravitation*, 28, 581–600, May 1996.
- R. Penrose. On the Gravitization of Quantum Mechanics 1: Quantum State Reduction. *Foundations of Physics*, 44, 557–575, May 2014.
- W. A. Phillips. Tunneling states in amorphous solids. *Journal of Low Temperature Physics*, 7, 351–360, 1972.
- L. S. C. Pingree, E. F. Martin, K. R. Shull, and M. C. Hersam. Nanoscale impedance microscopy—a characterization tool for nanoelectronic devices and circuits. *IEEE Transactions on Nanotechnology*, 4, 255–259, March 2005.
- M. Poggio and C. L. Degen. Force-detected nuclear magnetic resonance: recent advances and future challenges. *Nanotechnology*, 21, 342001, 2010.
- D. M. Pozar. *Microwave Engineering, 4th Edition*. Wiley, November 2011.

- N. V. Prokof'ev and P. C. E. Stamp. Theory of the spin bath. *Reports on Progress in Physics*, 63, 669, 2000.
- Quantum Design. Coupling Magnetic Signals to a SQUID Amplifier, December 2001. URL <http://www.qdusa.com/techsupport/index.html>.
- I. I. Rabi. *Science: the Center of Culture*. World Publishing Company, first edition. edition edition, January 1970.
- L. Rademaker, T. van der Reep, N. van den Broeck, B. van Waarde, J. M. de Voogd, and T. H. Oosterkamp. The Instability of a Quantum Superposition of Time Dilations. *arXiv:1410.2303 [quant-ph]*, October 2014. arXiv: 1410.2303.
- L. Robledo, H. Bernien, I. van Weperen, and R. Hanson. Control and Coherence of the Optical Transition of Single Nitrogen Vacancy Centers in Diamond. *Physical Review Letters*, 105, 177403, October 2010.
- S. B. Roobol, M. E. Cañas-Ventura, M. Bergman, M. A. van Spronsen, W. G. Onderwaater, P. C. van der Tuijn, R. Koehler, A. Ofitserov, G. J. C. van Baarle, and J. W. M. Frenken. The ReactorAFM: Non-contact atomic force microscope operating under high-pressure and high-temperature catalytic conditions. *Review of Scientific Instruments*, 86, 033706, March 2015.
- T. Roskopf, A. Dussaux, K. Ohashi, M. Loretz, R. Schirhagl, H. Watanabe, S. Shikata, K. M. Itoh, and C. L. Degen. Investigation of surface magnetic noise by shallow spins in diamond. *Phys. Rev. Lett.*, 112, 147602, 2014.
- M. J. Rost, L. Crama, P. Schakel, E. van Tol, G. B. E. M. van Velzen-Williams, C. F. Overgaw, H. ter Horst, H. Dekker, B. Okhuijsen, M. Seynen, A. Vijftigschild, P. Han, A. J. Katan, K. Schoots, R. Schumm, W. van Loo, T. H. Oosterkamp, and J. W. M. Frenken. Scanning probe microscopes go video rate and beyond. *Review of Scientific Instruments*, 76, 053710, May 2005.
- M. J. Rost, G. J. C. van Baarle, A. J. Katan, W. M. van Spengen, P. Schakel, W. A. van Loo, T. H. Oosterkamp, and J. W. M. Frenken. Video-rate scanning probe control challenges: setting the stage for a microscopy revolution. *Asian Journal of Control*, 11, 110–129, March 2009.
- D. Rugar, H. J. Mamin, P. Guethner, S. E. Lambert, J. E. Stern, I. McFadyen, and T. Yogi. Magnetic force microscopy: General principles and application to longitudinal recording media. *Journal of Applied Physics*, 68, 1169–1183, August 1990.
- D. Rugar, C. S. Yannoni, and J. A. Sidles. Mechanical detection of magnetic resonance. *Nature*, 360, 563–566, December 1992.

- D. Rugar, R. Budakian, H. J. Mamin, and B. W. Chui. Single spin detection by magnetic resonance force microscopy. *Nature*, 430, 329–332, 2004.
- R. Schlegel, T. Hänke, D. Baumann, M. Kaiser, P. K. Nag, R. Voigtländer, D. Lindackers, B. Büchner, and C. Hess. Design and properties of a cryogenic dip-stick scanning tunneling microscope with capacitive coarse approach control. *Review of Scientific Instruments*, 85, 013706, January 2014.
- M. Schlosshauer, A. P. Hines, and G. J. Milburn. Decoherence and dissipation of a quantum harmonic oscillator coupled to two-level systems. *Physical Review A*, 77, 022111, February 2008.
- T. Sleator, E. L. Hahn, C. Hilbert, and J. Clarke. Nuclear-spin noise and spontaneous emission. *Physical Review B*, 36, 1969–1980, August 1987.
- C. P. Slichter. *Principles of Magnetic Resonance*, volume 1 of *Springer Series in Solid-State Sciences*. Springer Berlin Heidelberg, Berlin, Heidelberg, 1990.
- W. V. Smith, P. P. Sorokin, I. L. Gelles, and G. J. Lasher. Electron spin resonance of nitrogen donors in diamond. *Phys. Rev.*, 115, 1546–1552, Sep 1959.
- Y. J. Song, A. F. Otte, V. Shvarts, Z. Zhao, Y. Kuk, S. R. Blankenship, A. Band, F. M. Hess, and J. A. Stroscio. Invited Review Article: A 10 mK scanning probe microscopy facility. *Review of Scientific Instruments*, 81, 121101, December 2010.
- B. C. Stipe, H. J. Mamin, T. D. Stowe, T. W. Kenny, and D. Rugar. Magnetic dissipation and fluctuations in individual nanomagnets measured by ultrasensitive cantilever magnetometry. *Phys. Rev. Lett.*, 86, 2874–2877, 2001a.
- B. C. Stipe, H. J. Mamin, C. S. Yannoni, T. D. Stowe, T. W. Kenny, and D. Rugar. Electron spin relaxation near a micron-size ferromagnet. *Phys. Rev. Lett.*, 87, 277602, 2001b.
- P. Strehlow, M. Wohlfahrt, A. G. M. Jansen, R. Hau Eisen, G. Weiss, C. Enss, and S. Hunklinger. Magnetic Field Dependent Tunneling in Glasses. *Physical Review Letters*, 84, 1938–1941, February 2000.
- S. Takahashi, R. Hanson, J. van Tol, M. S. Sherwin, and D. D. Awschalom. Quenching spin decoherence in diamond through spin bath polarization. *Phys. Rev. Lett.*, 101, 047601, Jul 2008.
- Y. Tao, J. M. Boss, B. A. Moores, and C. L. Degen. Single-crystal diamond nanomechanical resonators with quality factors exceeding one million. *Nat. Commun.*, 5, 3638, 2014.

- A. Tayebi and V. Zelevinsky. The Holstein polaron problem revisited. *Journal of Physics A: Mathematical and Theoretical*, 49, 255004, 2016.
- R. P. Taylor, G. F. Nellis, S. A. Klein, D. W. Hoch, J. Fellers, P. Roach, J. M. Park, and Y. Gianchandani. Measurements of the material properties of a laminated piezoelectric stack at cryogenic temperatures. In *Advances in Cryogenic Engineering*, volume 824, pages 200–207. AIP Publishing, 2006.
- C. J. Terblanche and E. C. Reynhardt. Room-temperature field dependence of the electron spin-lattice relaxation times of paramagnetic P1 and P2 centers in diamond. *Chemical Physics Letters*, 322, 273–279, May 2000.
- O. Usenko. *Development and testing of the gravitational wave antenna MiniGRAIL in its full-featured configuration*. Leiden University, May 2012.
- O. Usenko, A. Vinante, G. Wijts, and T. H. Oosterkamp. A superconducting quantum interference device based read-out of a subattonewton force sensor operating at millikelvin temperatures. *Applied Physics Letters*, 98(13):133105, 2011.
- A. Venkatesan, K. J. Lulla, M. J. Patton, A. D. Armour, C. J. Mellor, and J. R. Owers-Bradley. Dissipation due to tunneling two-level systems in gold nanomechanical resonators. *Physical Review B*, 81, 073410, February 2010.
- P. Vettiger, M. Despont, U. Drechsler, U. Durig, W. Haberle, M. I. Lutwyche, H. E. Rothuizen, R. Stutz, R. Widmer, and G. K. Binnig. The "Millipede";- More than thousand tips for future AFM storage. *IBM Journal of Research and Development*, 44, 323–340, May 2000.
- A. Vinante, G. Wijts, O. Usenko, L. Schinkelshoek, and T. H. Oosterkamp. Magnetic resonance force microscopy of paramagnetic electron spins at millikelvin temperatures. *Nature Communications*, 2, 572, December 2011a.
- A. Vinante, G. Wijts, O. Usenko, L. Schinkelshoek, and T. H. Oosterkamp. Magnetic Resonance Force Microscopy of paramagnetic electron spins at millikelvin temperatures. *ArXiv.org*, December 2011b. arXiv: 1105.3395v2.
- A. Vinante, A. Kirste, A. M. J. den Haan, O. Usenko, G. Wijts, E. Jeffrey, P. Sonin, D. Bouwmeester, and T. H. Oosterkamp. High sensitivity SQUID-detection and feedback-cooling of an ultrasoft microcantilever. *Applied Physics Letters*, 101, 123101, September 2012.
- A. Vinante, M. Bahrami, A. Bassi, O. Usenko, G. Wijts, and T. H. Oosterkamp. Upper Bounds on Spontaneous Wave-Function Collapse Models Using Millikelvin-Cooled Nanocantilevers. *Physical Review Letters*, 116, 090402, March 2016.

- J. M. de Voogd, M. A. van Spronsen, F. E. Kalff, B. Bryant, O. Ostojić, A. M. J. den Haan, I. M. N. Groot, T. H. Oosterkamp, A. F. Otte, and M. J. Rost. Fast and reliable pre-approach for scanning probe microscopes based on tip-sample capacitance. *Ultramicroscopy*, 181, 61–69, October 2017a.
- J. M. de Voogd, J. J. T. Wagenaar, and T. H. Oosterkamp. Dissipation and resonance frequency shift of a resonator magnetically coupled to a semiclassical spin. *Scientific Reports*, 7, 42239, February 2017b.
- B. E. Vugmeister. Spin diffusion and spin-lattice relaxation in paramagnetic crystals. *physica status solidi (b)*, 90, 711–718, December 1978.
- B. van Waarde. *The lead zeppelin : a force sensor without a handle*. Leiden University, November 2016.
- J. J. T. Wagenaar. *Magnetic resonance force microscopy for condensed matter*. Leiden University, July 2017.
- J. J. T. Wagenaar, A. M. J. den Haan, J. M. de Voogd, L. Bossoni, T. A. de Jong, M. de Wit, K. M. Bastiaans, D. J. Thoen, A. Endo, T. M. Klapwijk, J. Zaanen, and T. H. Oosterkamp. Probing the Nuclear Spin-Lattice Relaxation Time at the Nanoscale. *Physical Review Applied*, 6, 014007, July 2016.
- J. van Wezel and T. H. Oosterkamp. A nanoscale experiment measuring gravity's role in breaking the unitarity of quantum dynamics. *Proc. R. Soc. A*, 468, 35–56, January 2012.
- G. Wijts. *Magnetic resonance force microscopy at milliKelvin temperatures*. Leiden University, September 2013.
- J. A. van Wyk. Carbon-12 hyperfine interaction of the unique carbon of the P₂ (ESR) or N₃ (optical) centre in diamond. *Journal of Physics C: Solid State Physics*, 15, L981, 1982.
- J. A. van Wyk, E. C. Reynhardt, G. L. High, and I. Kiflawi. The dependences of ESR line widths and spin - spin relaxation times of single nitrogen defects on the concentration of nitrogen defects in diamond. *Journal of Physics D: Applied Physics*, 30, 1790, 1997.
- J. Q. You and F. Nori. Superconducting circuits and quantum information. *Physics Today*, 58, 42–47, November 2005.

List of publications

J. M. de Voogd, G. Welker, M. de Wit, and T. H. Oosterkamp. [Section 4.3](#)
Change in linear response of ultra sensitive magnetic probe reveals spin density of diamond bulk and surface spins. *In preparation*, 2017.

J. M. de Voogd, M. A. van Spronsen, F. E. Kalff, B. Bryant, O. Ostojić, A. M. J. den Haan, I. M. N. Groot, T. H. Oosterkamp, A. F. Otte, and M. J. Rost. [Chapter 7](#)
Fast and reliable preapproach for scanning probe microscopes based on tip-sample capacitance. *Ultramicroscopy*, 181, 61-69, October 2017.

J. M. de Voogd, J. J. T. Wagenaar, and T. H. Oosterkamp. [Chapter 2](#)
Dissipation and resonance frequency shift of a resonator magnetically coupled to a semiclassical spin. *Scientific Reports*, 7, 42239, February 2017.

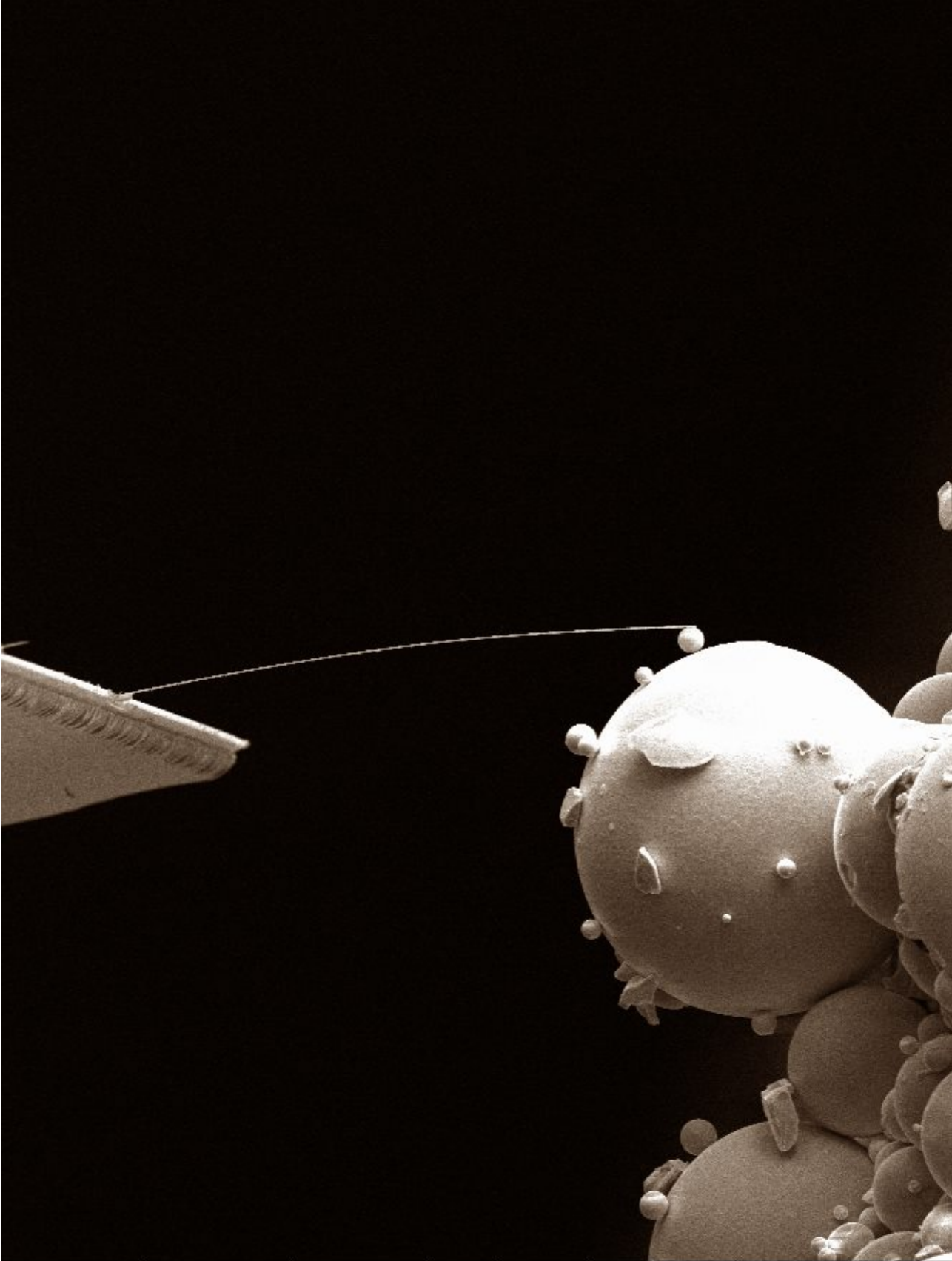
J. J. T. Wagenaar, A. M. J. den Haan, J. M. de Voogd, L. Bossoni, T. A. de Jong, M. de Wit, K. M. Bastiaans, D. J. Thoen, A. Endo, T. M. Klapwijk, J. Zaanen, and T. H. Oosterkamp. Probing the Nuclear Spin-Lattice Relaxation Time at the Nanoscale. *Physical Review Applied*, 6, 014007, July 2016.

A. M. J. den Haan, J. J. T. Wagenaar, J. M. de Voogd, G. Koning, and T. H. Oosterkamp. Spin-mediated dissipation and frequency shifts of a cantilever at milliKelvin temperatures. *Physical Review B*, 92, 235441, December 2015.

Chapter 3

L. Rademaker, T. van der Reep, N. van den Broeck, B. van Waarde, J. M. de Voogd, and T. H. Oosterkamp. The Instability of a Quantum Superposition of Time Dilations. *arXiv:1410.2303 [quant-ph]*, October 2014.

Section 5.2



WD	HV	mag	tilt	spot	curr	
5.6 mm	15.0 kV	1 000 x	0 °	3.5	0.18 nA	←

Samenvatting

De samenvatting is toegankelijk gemaakt voor een breed publiek. Hierom zijn sommige zaken vereenvoudigd en zijn er geen bronvermeldingen opgenomen. De wetenschappelijk geïnteresseerde lezer wordt verwezen naar de Engelstalige introductie in hoofdstuk 1.

BEGIN TWINTIGSTE EEUW werden er twee vernieuwende natuurkundige theorieën ontwikkeld die het wereldbeeld van de natuurkundige wetenschapper voorgoed veranderden. De ene theorie is Einsteins geometrische beschrijving van de zwaartekracht die de bewegingen van grote objecten nauwkeurig beschrijft. De andere theorie, de kwantummechanica, beschrijft de natuur op heel kleine schaal. Al een eeuw lang wordt geprobeerd deze twee theorieën te verenigen in één natuurkundig model. Dit wordt voornamelijk geprobeerd door de kwantummechanica uit te breiden en Einsteins theorie daar dan weer uit voort te laten komen. Dit is tot op heden niet gelukt.

VOLGENS DE KWANTUMMECHANICA kan een deeltje of object op meerdere plekken tegelijk zijn. Als we de positie van datgene meten, krijgen we echter maar één uitkomst. De kwantummechanica beschrijft wel heel nauwkeurig de kans op die uitkomst, maar niet precies welke uitkomst je daadwerkelijk gaat meten. Het moet worden benadrukt dat voor de meting het object écht op meerdere plekken tegelijk is. Echter, door een meting te doen begint het object na die meting weer

vanaf een enkele positie. De meting, hoe voorzichtig ook gedaan, beïnvloedt fundamenteel het te bestuderen object. Maar waarom beïnvloedt het observeren van een object de toestand van het object? Dit is het zogeheten meetprobleem.

Er zijn veel verschillende verklaringen bedacht, maar geen van alle is bewezen. Sommige interpretaties kunnen waarschijnlijk niet bewezen worden. Welke van deze interpretaties de juiste is, kan grote gevolgen hebben voor de wetenschap, omdat het onderwerp onder meer direct gelinkt is aan primordiale vraagstukken zoals: Wat betekent kans wanneer je maar over één uniek evenement spreekt?, Is energie misschien toch geen behouden grootte?, Zijn er andere parallele werelden?, en Bestaat er eigenlijk wel zoiets als vrije wil?

DE WETENSCHAPPERS Diósi en Penrose lieten met relatief eenvoudige redeneringen zien waar de kwantummechanica botst met Einsteins theorie en gebruikten deze conclusies in het onderbouwen van een nieuwe interpretatie van de kwantummechanica. Dus door het combineren van twee problemen konden Diósi en Penrose aangeven onder welke omstandigheden één of beide natuurkundige modellen niet meer kloppen. Hét grote verschil met andere interpretaties is dat we deze beweringen kunnen testen.

De afgelopen eeuw is er een wildgroei aan oplossingen ontstaan voor één of beide problemen, maar geen van alle is eenvoudig en kloppend genoeg. Wat we nodig hebben, is een test waarvan de uitkomst vele mogelijkheden uitsluit en, als het even kan, aanwijzingen geeft die leiden naar de juiste oplossing. Een dergelijk experiment is wat wij, en vele onderzoeksgroepen met ons, proberen te verwezenlijken.

Experiment

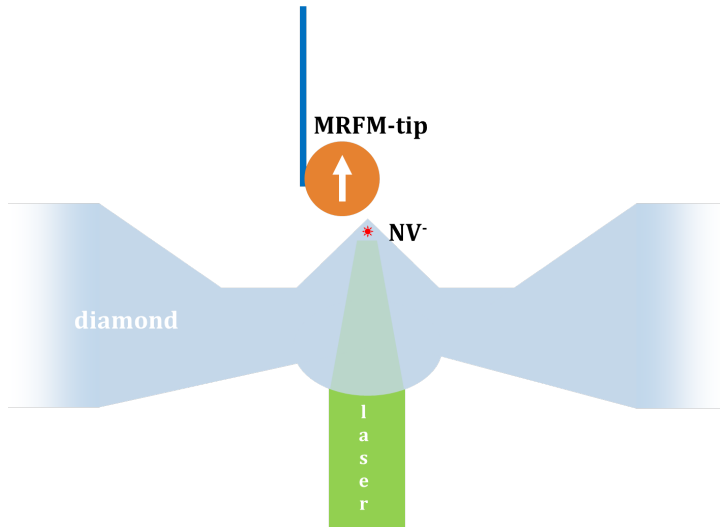
HET PRINCIPE van het experiment is heel eenvoudig: probeer een zo zwaar mogelijk object zo lang mogelijk op meerdere plekken tegelijk te laten zijn. Wij hebben

gekozen om een bestaande techniek te gebruiken en te verbeteren. Deze is de Magnetic Resonance Force Microscope (MRFM). Deze bestaat uit een klein magnetisch balletje dat aan een heel gevoelig veertje (in de vorm van een duikplankje) hangt. De elektronenmicroscopie-foto aan het begin van dit hoofdstuk is gemaakt net nadat wij het balletje van 0.003 mm doorsnede aan het 0.15 mm lange duikplankje hebben geplakt. De MRFM is door dit balletje zeer gevoelig voor magnetische velden, en dat kunnen we goed gebruiken.

Het balletje wordt vervolgens in de buurt van het te bestuderen object geïmponeerd. Sommige atomen zijn kleine magneetjes. Deze atoom-magneetjes, ook wel spins genoemd, kunnen we laten draaien. De MRFM-tip kan vervolgens voelen hoeveel en welke spins er draaien. Uit de trilling van de MRFM-tip kan dan weer het object gereconstrueerd worden. De methode om de hoeveelheid spins op een plek te meten door ze te laten draaien is vergelijkbaar met die van een MRI-scanner zoals die wordt gebruikt in het ziekenhuis.

De MRFM kan worden gebruikt voor zowel materiaalkundig onderzoek als biologisch onderzoek. Het is een unieke techniek omdat het, zonder het te bestuderen object kapot te maken, driedimensionale plaatjes kan maken van zowel eiwitten (waarvan de werking voornamelijk bepaald wordt door de driedimensionale structuur) als nieuwe soorten materialen die hun vele technologische toepassingen nog moeten vinden. De techniek staat echter nog in de kinderschoenen en er is nog veel onderzoek nodig om de MRFM commercieel inzetbaar te krijgen. Door voor het experiment - om een zwaar object op meerdere plekken te krijgen - te kiezen voor het MRFM-tipje, creëren we een win-winsituatie: wij kunnen gebruik maken van de al bestaande technieken en met ons onderzoek dragen wij weer bij aan de verdere ontwikkeling van de MRFM.

Het plan, zoals uitgelegd in hoofdstuk 5, is als volgt: We brengen de MRFM-tip naar een diamantje, dichtbij een plek waar we een enkel zeer speciaal atoommagneetje hebben ingebracht. Deze spin, aangeduid met NV^- , kunnen we nauwkeurig



Schets van het bedachte toekomstige experiment. In het diamant bevindt zich het NV^- -center. De speciale pyramide of kegelvorm zou opwarming van het MRFM-tipje zoveel mogelijk voorkomen. Een uitgebreide uitleg staat in paragraaf 5.5.

manipuleren met een laser. Deze techniek wordt gebruikt in kwantummechanische netwerken en is al ver ontwikkeld. Vervolgens laten wij de spin in twee richtingen tegelijkertijd draaien. De vraag is dan hoe lang het MRFM-tipje tegelijkertijd in twee richtingen zal bewegen.

Techniek

HET EXPERIMENT is makkelijker beschreven dan gedaan, want de condities waarin dit moet gebeuren zijn gecompliceerd. Doordat de MRFM-tip in contact is met de door de temperatuur trillende atomen waaruit het experiment is opgebouwd, moet het gehele experiment worden afgekoeld naar -273.14 graden Celsius, 0.01 graad boven het absolute nulpunt. Een lagere temperatuur zou het experiment nog

minder verstoren, maar in hoofdstuk 5 laten we zien dat door gebruik te maken van het experiment we vanaf deze temperatuur alle overige trillingen actief uit de MRFM-tip kunnen 'pompen'.

Gebruikelijk wordt de beweging van een MRFM-tip uitgelezen met behulp van een laser. Dit zou in dit experiment echter teveel opwarming geven en daarom meten wij de beweging van de MRFM-tip door de stroom te meten die het bewegende magnetische balletje opwekt in een supergeleidend elektrisch circuitje. Hoofdstuk 6 beschrijft onder andere het recept dat is gebruikt om de supergeleidende baantjes van 0.0004 mm breed in dit circuit te produceren. Daarnaast worden in hoofdstuk 6 nog meer methodes en technologie beschreven die wij hebben ontwikkeld of ingezet ten behoeve van dit experiment. Met name het positioneren van de tip, en het uitlezen van de positie van de MRFM-tip in de kou, zonder licht of magneetvelden te gebruiken, is een kritiek technisch onderwerp. Het nauwkeurig uitlezen van de afstand tussen twee elektrisch geladen plaatjes blijkt niet alleen handig te zijn voor het MRFM experiment, maar ook voor andere types microscopen die werken met een tipje en die de afstand willen weten tussen het tipje en het sample, zoals gedetailleerd beschreven is in het gepubliceerde artikel van hoofdstuk 7.

Wetenschappelijke bevindingen

UIT EERDER ONDERZOEK met MRFM bleek dat de gevoeligheid van de MRFM-tip minder wordt naarmate het magneetje dichterbij het oppervlak van het sample komt. Tot nog toe was er geen beschrijving die deze extra demping van beweging kon verklaren. De grondige theoretische analyse in hoofdstuk 2 laat zien dat de spins, waarvan we sommige willen meten, alle tezamen de MRFM-tip afremmen en de trillingstijd veranderen. Deze theorie is geverifieerd door in een MRFM-experiment de tip heel voorzichtig te laten naderen boven een stukje siliciumoxide,

zoals beschreven in hoofdstuk 3. Het effect neemt toe wanneer de temperatuur van het experiment afneemt. Tegenintuïtief is echter dat onder een bepaalde temperatuur het effect weer minder wordt. De theorie beschrijft de resultaten van het experiment nauwkeurig. De artikelen van beide hoofdstukken zijn gepubliceerd. Dit effect nauwkeurig begrijpen is van groot belang voor het experiment omdat de gevoeligheid van de MRFM-tip hoog moet zijn. We begrijpen hierdoor nu onder andere beter hoe zuiver het diamant en hoe schoon het oppervlak ten minste moet zijn. Tenslotte hebben wij een diamanten sample onder de MRFM gemonteerd. Met de nu bekende theorie van hoofdstuk 2 hebben wij de zuiverheid van het diamant (ongeveer 400 op de miljard atomen hoort niet in puur diamant thuis) en de oppervlakteverontreiniging (ongeveer 60 miljard spins per vierkante millimeter) kunnen meten. Verder hebben wij de mogelijkheden verkend om MRI te doen op deze atomen, onder deze omstandigheden. Daarmee vonden wij dat het magneetje nog kleiner mag, of dat we de spins harder moeten laten draaien.

WIJ kunnen concluderen dat de eerste stappen technisch, theoretisch en experimenteel gezet zijn richting een experiment dat het natuurkundige wereldbeeld drastisch kan veranderen.

Acknowledgements

DURING MY PHD I have had the pleasure to work together with many people and I received lots of help. Although it would not be possible to express my gratitude to everyone who has supported me in so few words, I would like to acknowledge at least some of these people here.

I am very grateful to my promotor Tjerk Oosterkamp for his guidance and encouragement. Your view on science and, above that, on life has been very inspiring. Furthermore, when going for the ridiculously challenging goals you have set (which this thesis is only a beginning of), you always showed how much fun it actually is doing something while confronted with the edge of the impossible.

This brings me to Kier Heeck whom I would like to thank for his imperturbable enthusiasm to explain thoroughly how techniques, methods, and tricks in electronics and mechanics actually work and for putting them in a greater perspective. I still profit from this knowledge nearly every day.

I have had the luck of working together with Martin de Wit who helped me a lot. We complemented each other in many things. I would like to thank Jelmer Wagenaar for fruitful discussions and styling the figures in this thesis. I would also like to thank the other members from the Oosterkamp group: Arthur, Bob, Gesa, Lucia, Tom, Geert, Olaf, Louk, and all MSc and BSc students who joined the group during my time there. Beside work we had lots of fun together.

The people from the fine mechanics department: Gert, Dian, Fred, and Merlijn, the people from the electronics department: Ko, Bert, Peter, and Raymond, and Wim

Bosch, Ireyana Usenko, and LSI BV played a crucial role in the design and construction of the setup and experiment.

I am indebted to Pavel Antonov for my training in the Kavli Nanolab clean room, and to David Thoen for his help on the fabrication of my samples. Also, I would like to thank the people from the group of Dirk Bouwmeester, and all others in the measurement hall, and the people from the Kavli Nanolab, Hanson Lab, Steele Lab, and Yaroslav Blanter for fruitful discussions on the construction of the experiments on diamond, both technically and theoretically.

For the experiments and simulations on the capacitive pre-approach (Ch. 7) I am grateful to Marcel Rost and all co-authors.

I thank Ellie van Rijsewijk for taking care of all the bureaucracy and the never-ending supply of coffee.

During my PhD I was a member of the very last central works council (COR) of FOM and I would like to thank all other representatives for the intensive and great years we had together.

Finally, I am grateful to my family. Ine, thank you for all the time and energy that I could devote to this work. I am truly indebted to you and our children for this. Nevertheless, I hope and know that you will support me also in the next adventure. Thank you.

Curriculum Vitae

JACOBUS MARINUS DE VOOGD (Marc) was born on January 29th 1989 in Vlissingen and grew up in Grijskerke, The Netherlands. After he graduated from VWO at Calvin College Goes in 2007, he went to Leiden to study physics. He obtained his BSc degree after research on the change of the transfer function of MRI receiver coils due to the different salinities of human heads. The research was conducted at the 7T MRI scanner at the Gorter Center for High Field MRI at the LUMC under supervision of Prof. dr. A. G. Webb and Prof. dr. ir. T. H. Oosterkamp.

Following this, he studied theoretical physics and did his MSc research under supervision of Prof. dr. K. E. Schalm and Dr. D. Garlaschelli. The subject of his MSc thesis was the configuration relaxation of space, which consisted of two parts: resonant tunneling in scalar field theory, and the freezing of bubbly space. In 2012 he obtained his MSc in Physics cum laude.

He went on to pursue a PhD under supervision of Prof. dr. ir. T. H. Oosterkamp in which he did technical, experimental, and theoretical work on Magnetic Resonance Force Microscopy (MRFM). With his work he tried to pave the way for experiments that eventually might be able to detect gravitational induced decoherence. Also, he explained the change of the transfer function when the MRFM tip approaches the sample and interacts with the spin bath. This work is described in this thesis.

During the last two years of his PhD, he was vice secretary of the (last) Central Works Council (COR) at FOM, the Dutch Foundation for Fundamental Research on Matter during a fusion and reorganization with the parent organization NWO, the

Netherlands Organisation for Scientific Research.

As of May 2017, Marc is working part-time at LPM BV, a company that creates custom scientific setups in the field of scanning probe microscopy and research catalysis reactors. Besides this, he started a company De Voogd Scientific that consults on scientific setups in the field of scanning probe microscopy and quantum computing. In the future he plans to sell modular scientific electronics under the name Godfather Instrumentation.

ISBN 978-90-8593-333-5
Casimir PhD series 2018-01